# BASIC TESTING AND STRENGTH DESIGN OF CORRUGATED BOARD AND CONTAINERS

TOMAS NORDSTRAND

Structural
Mechanics

Doctoral Thesis

BASIC TESTING AND STRENGTH DESIGN OF CORRUGATED BOARD AND CONTAINERS

Doctoral Thesis by

TOMAS NORDSTRAND

ABSTRACT

Packaging serves a lot of purposes, and would be hard to do without. Packaging protects the goods during transport, saves costs, informs about the product, and extends its durability. A transport package is required to be strong and lightweight in order to be cost effective. Furthermore, it should be recycled because of environmental and economical concerns. Corrugated board has all of these features.

This thesis is compiled of seven papers that theoretically and experimentally treat the structural properties and behaviour of corrugated board and containers during buckling and collapse. The aim was to create a practical tool for strength analysis of boxes that can be used by corrugated board box designers. This tool is based on finite element analysis.

The first studies concerned testing and analysis of corrugated board in three-point-bending and evaluation of the bending stiffness and the transverse shear stiffness. The transverse shear stiffness was also measured using a block shear test. It was shown that evaluated bending stiffness agrees with theoretically predicted values. However, evaluation of transverse shear stiffness showed significantly lower values than the predicted values. The predicted values were based on material testing of constituent liners and fluting prior to corrugation. Earlier studies have shown that the fluting sustains considerable damage at its troughs and crests in the corrugation process and this is probably a major contributing factor to the discrepancy. Furthermore, the block shear method seems to constrain the deformation of the board and consistently produces higher values of the transverse shear stiffness than the three-point-bending test. It is recommended to use the latter method.

Further experimental studies involved the construction of rigs for testing corrugated board panels under compression and cylinders under combined stresses. The panel test rig, furnishing simply supported boundary conditions on all edges, was used to study the buckling behaviour of corrugated board. Post-buckling analysis of an orthotropic plate with initial imperfection predicted failure loads that exceed the experimental values by only 6-7 % using the Tsai-Wu failure criterion. It was confirmed, by testing the cylinders that failure of biaxially loaded corrugated board is not significantly affected by local buckling and that the Tsai-Wu failure criterion is appropriate to use.

A method for prediction of the top-to-bottom compression strength of corrugated board containers using finite element analysis was developed and verified by a large number of box compression tests. Up to triple-wall corrugated board is accommodated in the finite element model. The described FE-method for predicting the top-to-bottom compressive strength of corrugated containers has been used as the basic component in the subsequent development of a user-friendly computer-based tool for strength design of containers.

Keywords: analysis, bending, box, buckling, collapse, compression, corrugation, corrugated board, crease, design, experiment, failure criterion, fluting, finite element method, liner, local buckling, packaging, panel, paper, stiffness, strength, test method, transverse shear

CONTENTS   PAGE

 PART II: APPENDED PAPERS

Part I

Introduction and Summary

INTRODUCTION AND SUMMARY

General remarks

In 2001 the European transport packaging market had an estimated value of approximately $20 billion. Corrugated board represented 62 per cent of this market value [1]. A transport package is required to be strong and lightweight in order to be cost effective. Furthermore, it should be recycled because of environmental and economical concerns. Corrugated board has all of these features. In its most common form, viz. single-wall board, two face sheets, called liners, are bonded to a wave shaped web called fluting or medium, see Figure 1. The resulting pipes make the board extremely stiff in bending and stable against buckling in relation to its weight [1]. Consequently, the strength of the wood fibres in the board is also utilised in an efficient way. The fluting pipes are oriented in the cross-direction (y, CD) of board production, see Figure 1. The orientation of the board in-line with production is called machine-direction (x, MD). Orientation through the thickness of the board is denoted Z-direction (z, ZD). This definition of principal directions is also used for the constituent paper sheets.

Figure 1. Single-wall corrugated board.

In area, about 80 per cent of corrugated board production is single-wall board. The rest is produced for more demanding packaging solutions that require double or triple-wall board, illustrated in Figure 2.

Figure 2. Double and triple-wall corrugated board.

The profile of a corrugated web in Figure 3 is characterised by a letter, A, B, C, E or F, specified in Table 1 [1]. Also listed in Table 1 are the take-up factors which quantify the length of the fluting per unit length of the board. For example, one metre of corrugated board with B-flute requires a 1.32 m long piece of paper prior to corrugation.
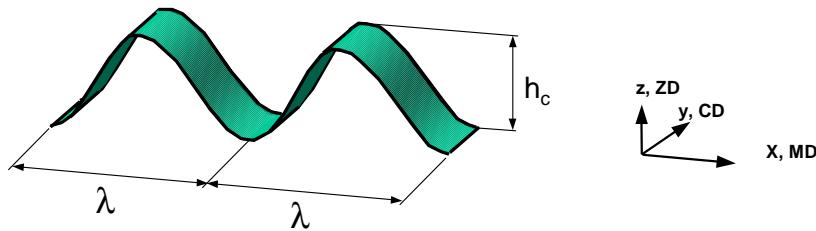
Figure 3. The geometry of a corrugated web.

As seen in Table 1 the tallest core profile is A-flute, which is used in board for heavy duty boxes. B and C-flute are used for the most common board grades. The E and F-flutes are small and consequently used in board for smaller boxes, e.g. perfume packages, where appearance and printability are important [1].

Table 1. Flute profiles.

Profile	A	B	C	E	F
Wavelength, λ (mm)	8.3-10	6.1-6.9	7.1-8.3	3.2-3.6	2.3-2.5
Flute height, h_c (mm)	4.67	2.46	3.61	1.15	0.76
Take-up factor, α	1.54	1.32	1.43	1.27	1.25

A corrugator is a set of machines in line, designed to bring together liner and medium to form single, double or triple-wall board. This operation is achieved in a continuous process, see Figure 4.

The reels of liner and medium are fed into the corrugator. The medium is conditioned with heat and steam and fed between large corrugating rolls forming fluting. In the Single Facer, starch adhesive is applied to the tips of the flutes on one side and the inner liner is glued to the fluting. The fluting with one liner attached to it is called single-face web and travels along the machine towards the Double Backer where the single-face web is bonded to the outer liner and forms corrugated board. The corrugated board is then cut and stacked.
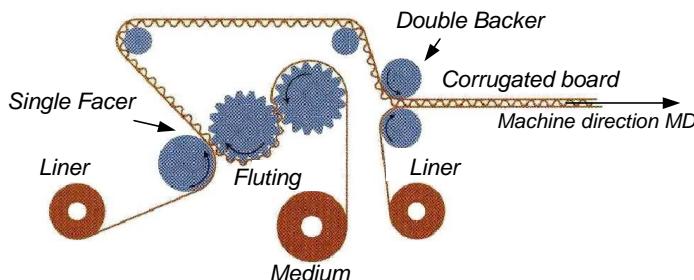
Figure 4. Manufacture of corrugated board.

The first corrugators were built in the US at the start of the last century. However, up until 1920, the majority of products shipped via railroads, for example, were packed in wooden crates. The corrugated box was relatively new and few had any experience in transporting them. In order to avoid liability for damage while shipping items in corrugated boxes, railroads in the US established a standard known as Rule 41. Rule 41 was an important step in opening up the market for corrugated board packaging. Later on, during World War II, corrugated board packaging was called upon to deliver rations and other war material to all corners of the earth. This contributed to the establishment of corrugated board globally. After the war the market grew rapidly, and the range of sizes and capabilities of corrugated boxes grew to fit the myriad of new products developed. Recently, the combination of a plastic bag inside a corrugated board box (bag-in-box) has resulted in many new opportunities, including the latest trend packaging of wine.

Corrugated board is permeable to moisture and absorbs water. This will reduce its strength and stiffness. However, it can be made both water and grease proof.

Many package styles and design options are possible, but often an international standard of box styles [2], the FEFCO-code, is used in specifying a design. One of the most common box styles is the regular slotted container (RSC) denoted FEFCO 0201, see Figure 5. The box size is specified by L×W×H, i.e. length of the longest side panel, width of the shortest side and height. The flap size is half of the width. In the logistics chain in Sweden a transport package is usually adjusted to the EUR-pallet. Thus the length and width of an RSC are usually uniform divisions of the pallet size (1200x800 mm), e.g. 300x200 mm or 600x400 mm.
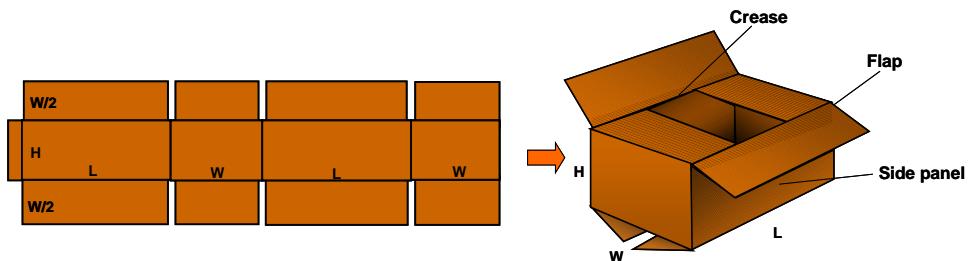
Figure 5. A regular slotted container, code FEFCO 0201.

RSC:s are produced with an in-line Slotter-Folder-Gluer, which in one operation creases, cuts, folds and glues the blank into its final shape. The RSC is then palletised and ready to be shipped flat to the customer.

Background and earlier work

Several experimental studies have been conducted on the compression strength of corrugated board containers [3,4]. The most common failure mode for a corrugated box loaded in top-to-bottom compression is post-buckling deflection of its side panels,

followed by biaxial compressive failure of the board in the highly stressed corner regions of the box. Local instabilities of the liners and fluting may also interact with the failure progression [5-8]. A detailed finite element analysis of a corrugated board panel has shown that local buckling of one of the liners may occur before actual material failure [9]. This can also be observed visually just prior to compression failure of panels and boxes [10]. However, for shallow boxes and boxes with high board bending stiffness in comparison to the box perimeter, failure is often caused by crushing of the creased board at the loaded edges instead of collapse during buckling [11].

When considering the compression of panels in a box it is recognised that the flaps, attached to the panels through the creases at top and bottom edges, introduce an eccentricity in the loading [12, 13]. Furthermore, the top and bottom edges normally have a much lower stiffness than the interior of the panel due to the creases. It has been concluded that the low stiffness prevents a redistribution of the stresses to the corners of the box and consequently reduces the box compression strength.

Several previous investigations have involved finite element analysis of corrugated board. Peterson [14] developed a finite element model to study the stress fields developed in a corrugated board beam under three point loading. Pommier and Poustius studied bending stiffnesses of corrugated board using a linear elastic finite element code [15]. Pommier and Poustius also developed a linear elastic finite element model for prediction of compression strength of boxes [16]. Likewise a linear elastic finite element model of a corrugated board panel for prediction of compression strength was developed by Rahman [17].

Patel developed a linear elastic finite element model in a study of biaxial failure of corrugated board [18]. The model was used to predict buckling patterns of a circular tube subjected to different loading conditions. In an investigation by Nyman, local buckling of corrugated board facings was studied numerically through finite element calculations [19].

Little published work is available on the use of non-linear constitutive models for prediction of strength of corrugated board structures. However, a non-linear model of corrugated board was developed by Gilchrist, Suhling and Urbanik [20]. In their model, both material and geometrical non-linearities were included, in-plane and transverse loadings of corrugated board were examined. Bronkhorst and Riedemann [21] and Nordstrand and Hagglund [22] have developed non-linear finite element models for corrugated board configurations. These investigations generated predictions for compressive creep of a box and time-dependent sagging of a corrugated board tray.

Aim of present work

This project was initiated with the objective of developing a design method based on fundamental engineering mechanics to predict the strength of corrugated containers in top-to–bottom compression.

General assumptions and limitations in present work

The major assumptions and limitations adopted in this work are as follows:

- Paper is regarded as a homogenous continuum with liner elastic orthotropic properties.
- Influence of load duration, e.g. creep, moisture and inertia forces are not analysed.
- Deterministic characterisation of material properties, geometry and loading.
- Box strength analysed only for loading in top-to-bottom compression.

Summary of contents and major conclusions

In Paper 1, expressions for the transverse shear stiffnesses of corrugated board are derived by considering a shear loaded element of the corrugated board and using the theory of curved beams. It is shown how the transverse shear stiffness in the machine direction is significantly changed by the transition from one core shape to another. An experimental study of the transverse shear stiffness is given in Paper 2, where the transverse shear stiffness is measured both by a block shear test and evaluated from a three-point flexure test. The three-point flexure test is also simulated using finite element analysis. Values of transverse shear stiffnesses obtained from the block shear test are much larger than values evaluated from the three-point flexure test. The difference is attributed to the highly constrained deformation of the facings in the block shear test. It is also shown that experimental values are significantly lower than calculated values obtained in Paper 1 and obtained from the finite element analysis. This is probably caused by delamination damage to the corrugated medium inflicted during the corrugation process.

In Paper 3, an expression is derived for the buckling load of a simply supported orthotropic plate including first order transverse shear deformation. The influence of the transverse shear on critical buckling is studied and compared with ordinary sandwich theory. Its primary use, however, is to verify the buckling load obtained in a finite element analysis of a simply supported single-wall corrugated board panel in Paper 4. The influence on the panel strength of different parameters such as asymmetry, slenderness of the corrugated board and eccentric loading is studied in Paper 4. It was concluded that panel strength is very sensitive to boundary conditions and change in core thickness of the board, i.e. the change in bending stiffness of the board.

In Paper 5, a panel compression test rig, furnishing simply supported boundary conditions on all edges, was designed and used to study the buckling behaviour of corrugated board panels. An analysis of an orthotropic plate with initial imperfection is presented in Paper 5 to predict the collapse load using the Tsai-Wu failure criterion. A significant difference was observed between analytically predicted and experimentally measured displacements at large out-of-plane deformation. This is probably caused by non-linear material behaviour of paper and local buckling of the panel facings, i.e. the

liners. However, the analytically predicted failure load exceeds experimental values by only 6-7 %. This suggests that collapse of the corrugated board panel is triggered by material failure of the inner facing. It is also concluded in Paper 6, where an experimental study of biaxially loaded corrugated board is presented, that failure is not significantly affected by local buckling of the corrugated board and that the Tsai-Wu criterion is appropriate to use.

Finally, in Paper 7, a finite element method developed for stress and strength analysis of corrugated containers using the failure criterion above is presented. The corrugated board is represented by multi-ply eight node isoparametric shell elements, and the soft creases at the loaded top and bottom edges are accommodated in the finite element model by spring elements. Effective material properties of the homogenised corrugated cores have been used, and each layer of the corrugated board is assumed to be orthotropic linear elastic. It is shown that convergence is obtained with relatively few elements, e.g. 144 elements are quite sufficient for a regular size box, i.e. 300x300x300 mm. Sensitivity of the collapse load to the imposed compliance at the loaded boundaries is also studied. Different buckling modes of a box are simulated giving an in-depth understanding of the relation between the strength of a box and constraints imposed on the panels by the corners of the box. Extensive testing of boxes made from B- and C-board shows that predicted failure loads using the proposed finite element model have an average error margin of 5% compared to measured box strengths.

Concluding remarks and future research

Box performance requirements range from its appearance, to its mechanical strength and ability to protect its contents. Mechanical properties can be divided into two categories, those that pertain to rough handling and stacking. Both of these types are difficult to duplicate accurately in the laboratory. As a consequence, the box compression test or BCT of an empty container has been widely used as a means of evaluating container performance. However, in order to distinguish between factors that govern box performance it is necessary to test the quality of the corrugated board and its components, maintain good control of conversion operations and environmental influences such as humidity and load duration. In addition to standard testing methods, a future challenge for research is to develop more sophisticated testing methods that are based on finite element models. Once the roles of liner and medium behaviour in box performance are properly understood, material properties can be evaluated by mill and plant personnel so that attention is given to the properties that govern end-use performance. For example, corrugated containers that are stacked on top of each other will slowly deform with time until one of the boxes collapses or the stack falls over. Consequently, the relevance of studying creep behaviour of paper and board is that it can reduce stacking factors in design of corrugated board packages. This is a future goal in the development of a user-friendly computer-based tool for strength design of containers. Finally, this work shows how far it is possible to predict box performance using an orthotropic linear elastic material model, multi-ply eight node iso-parametric finite element and the Tsai-Wu failure criterion.

Presented papers

Paper 1: T. Nordstrand, H. G. Allen and L. A. Carlsson, "Transverse Shear Stiffness of Structural Core Sandwich", Composite Structures, No. 27, pp. 317-329, 1994.

Paper 2: T. Nordstrand and L. A. Carlsson, "Evaluation of Transverse Shear Stiffness of Structural Core Sandwich Plates", Composite Structures, Vol. 37, pp. 145-153, 1997.

Paper 3: T. Nordstrand, "On Buckling Loads for Edge-Loaded Orthotropic Plates including Transverse Shear". To be submitted to Composite Structures.

Paper 4: T. Nordstrand, "Parametrical Study of the Post-buckling Strength of Structural Core Sandwich Panels", Composite Structures, Vol. 30, pp. 441-451, 1995.

Paper 5: T. Nordstrand, "Analysis and Testing of Corrugated Board Panels into the Post-buckling Regime". To be submitted to Composite Structures.

Paper 6: P. Patel, T. Nordstrand and L. A. Carlsson, "Local buckling and collapse of corrugated board under biaxial stress", Composite Structures, Vol. 39, No. 1-2, pp. 93-110, 1997.

Paper 7: T. Nordstrand, M. Blackenfeldt and M. Renman, "A Strength Prediction Method for Corrugated Board Containers", Report TVSM-3065, Div. of Structural Mechanics, Lund University, Sweden, 2003.

Acknowledgements

References

1. R. Steadman, "Corrugated Board", Ch. 11, in Handbook of Physical Testing of Paper, (R.E. Mark et al. eds.), pp. 563-660, Marcel Dekker, New York, 2002.

2. FEFCO, Avenue Louise 250, B – 1050 Brussels, Belgium, www.fefco.org.

3. R. C. McKee and J. W. Gander, "Top-Load Compression", TAPPI, Vol. 40, No. 1, pp. 57-64, 1957.

4. R. C. McKee, J. W. Cander, and J. R. Wachuta, "Compression Strength Formula for Corrugated Boxes", Paperboard Packaging, 48, pp. 149-159, 1963.

5. M. W. Johnson and T. J. Urbanik, "Analysis of the Localized Buckling in Composite Plate Structures with Application to Determining the Strength of Corrugated Fiberboard", J. Comp. Tech. & Res., 11 (4), pp.121-127, 1989.

6. B. S. Westerlind and L. A. Carlsson, "Compressive Response of Corrugated Board", TAPPI, 75 (7), pp.145-154, 1992.

7. P. Patel, T. Nordstrand and L.A. Carlsson, "Instability and Failure of Corrugated Core Sandwich Cylinders Under Combined Stresses", in Multiaxial Fatigue and Deformation Testing Techniques, ASTM STP 1280(S. Kalluri and P.J. Bonacuse, Eds.), pp. 264-289, 1997.

8. P. Patel, T. Nordstrand and L. A. Carlsson, "A Study on the Influence of Local Buckling on the Strength of Structural Core Sandwich Structures", Proceedings of EUROMECH 360, Ecole des Mines de Saint-Etienne, 1997.

9. A. Allansson and B. Svärd, "Stability and Collapse of Corrugated Board", Master thesis, Report TVSM-5102, Division of Structural Mechanics, Lund University, Sweden, 2001.

10. E. K. Hahn, A.de Ruvo and L. A. Carlsson, " Compressive Strength of Edge-loaded Corrugated Panels", Exper. Mech., Vol. 32, pp. 252-258, 1992.

11. W. Vollmer, "Components of Compression Testing on Corrugated Board Packaging ", FEFCO. XIIIth Congress, 1974.

12. J. S. Buchanan, "The Effect of Crease Form on the Compressive Strength of Corrugated Cases", Packaging, pp. 37-43, March, 1963.

13. M. Renman, "A mechanical characterization of creased zones of corrugated board", Licentiate thesis, Report 94:05, Division of Engineering Logistics, Lund University, Sweden, 1994.

14. W. S. Peterson, "Unified Container Performance and Failure Theory I : Theoretical Development of Mathematical Model", TAPPI, Vol. 63(10), pp. 75-79, 1980.

15. J. C. Pommier and J. Poustis, "Bending Stiffness of Corrugated Board Prediction Using the Finite Element Method, Mechanics of Wood and Paper Materials", ASME AMD-Vol. 112, Edited by R.W. Perkins, pp. 67-70, 1990.

16. J. C. Pommier, J. Poustis,Bending, J. Fourcade and P. Morlier, "Determination of the critical load of a Corrugated Box Subjected to Vertical Compression by Finite Element Method", Proceedings of the 1991 International Paper Physics Conference, pp. 437-447, Kona, HI, 1991.

17. A. Rahman, "Finite element buckling analysis of corrugated fiberboard panels", Proceedings of the 1997 joint ASME/ASCE/SES summer meeting entitled mechanics of cellulosic materials, pp. 87-92; June 29-July 02, 1997.

18. P. Patel , "Biaxial Failure of Corrugated Board", Licentiate thesis, Division of Eng. Logistics, Lund University, Sweden 1996.

19. U. Nyman, P.J. Gustafsson, "Material and Structural Failure Criterion of Corrugated Board Facings", Accepted for publication in Composite Structures.

20. A. C. Gilchrist, J. C. Suhling and T. J. Urbanik., "Nonlinear finite element modeling of corrugated board", Mechanics of Cellulose Materials- ASME AMD-Vol 231/MD-Vol 85, pp. 101-106, 1999.

21. C. A. Bronkhorst and J. R. Riedemann, "The Creep Deformation Behaviour of Corrugated Containers in a Cyclic Moisture Environment", Proceedings of the Symposium on Moisture Induced Creep Behaviour of Paper and Board, pp. 249-273, Stockholm , Sweden, December 5-7, 1994.

22. T. Nordstrand and R. Hagglund, "Predicting Sagging of Corrugated Board Tray Bottom Using Isochrones", Proceedings of the 3rd International Symposium on Moisture and Creep Effects on Paper, Board and Containers, pp. 215-220, Rotorua, New Zeeland, February 20-21, 1997.

Part II

Appended Papers

Paper 1

———

Transverse Shear Stiffness of Structural Core Sandwich

by

T. Nordstrand, Carlsson, L.A. and Allen, H.G.

Transverse shear stiffness of structural core sandwich

Tomas Nordstrand

SCA Research AB, Box 3054, 850 03 Sundsvall, Sweden

Leif A. Carlsson

Department of Mechanical Engineering, Florida Atlantic University, Boca Raton, Florida 33431, USA

&

Howard G. Allen

Department of Civil Engineering, Southampton University, Southampton SO9 5NH, UK

Transverse shearing deformations in corrugated core sandwich plates cannot always be disregarded in the calculation of their strength and stability. This makes it necessary to accurately characterize the corresponding shear stiffnesses. In an effort towards this goal a theoretical study on how various core shapes influence the effective transverse shear moduli is presented. An upper limit of the transverse shear modulus across the corrugations is calculated assuming rigid facings. The reduction of the effective shear modulus across the corrugation due to deformations of the facings is quantified and the results are compared with classical theory and finite elements.

INTRODUCTION

Corrugated core sandwich plates possess high strength and stiffness per unit weight. A common application of this material is in corrugated board boxes for shipment of goods. These boxes are often stacked on top of each other during transportation and in storage. Thus, an important design parameter for a box is the top-to-bottom compression strength.[1] Before collapse, the vertical sides undergo large out-of-plane deformations with loads often exceeding the critical buckling load.[2-4] The processes of load redistribution and final collapse are governed by the boundary conditions, the transverse shear rigidities and the flexural rigidities of the panel.[5,6] The transverse shear stiffness of a sandwich is always less than that of a homogeneous member of the same flexural stiffness, because of the use of a light-weight and flexible core. Consequently, transverse shearing deformations in the sandwich cannot always be disregarded in the calculation of the strength and stability.[7] For structural cores, such as the corrugated one, it is convenient to define effective elastic constants for an equivalent homogeneous core material. This is adequate when the sandwich plate width is many times greater than the corrugation pitch.[8] Since the corrugated core is orthotropic, two effective transverse shear moduli, G_{xz} and G_{yz}, corresponding to shear stresses τ_{xz} and τ_{yz} have to be determined, see Fig. 1.

Elastic stiffnesses for corrugated cores composed of straight members were derived by Libove and Hubka.[9] Ko[10] modified Libove and Hubka's results to account for nonuniform corrugation legs and compared the effective transverse shear modulus G_{xz} for the corrugated core type above with a honeycomb core of the same effective density.

This paper presents an analysis of G_{xz} based on curved beam theory[11] which is subsequently applied to various geometrical shapes of the core in order to illustrate how sensitive G_{xz} is to the curvature of the corrugation. Only sandwiches with identical facings will be considered and the corrugation pitch is assumed to be symmetrical. An approximate expression for G_{yz} is also provided. Results are compared with G_{xz} obtained from design curves given by Libove and Hubka[9] and G_{xz} computed using the ANSYS finite element computer code.[12]

317

ANALYSIS

In the first part of this section an expression for the upper limit of the transverse shear modulus G_{xz} is derived based on rigid facings. The second part deals with the reduction of G_{xz} due to elastic facings. The third part gives an expression for calculating G_{yz} approximately.

Upper bound on the effective transverse shear modulus G_{xz}

Consider a strip of the corrugated layer of thickness t_c and width b from a trough to a crest represented by its centre line and clamped at point A, see Fig. 2. The corrugation pitch is p and the core height is h_c. The centre line is described by a function

$$\zeta = f(\xi) \tag{1}$$
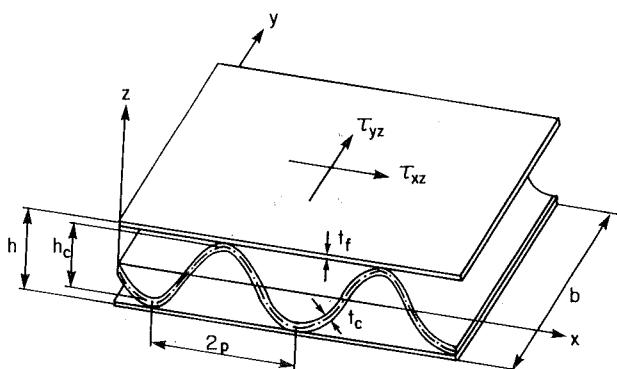
Fig. 1. A sandwich plate with unidirectionally corrugated core of total thickness h. The thickness of the facings and the corrugated sheet are t_f and t_c, respectively. The wavelength of the corrugation pitch is $2p$ and the width is b.

where the horizontal ξ-axis lies in the middle plane of the sandwich and is orthogonal to the corrugations and the vertical ζ-axis is normal to the middle plane.

Figure 3 shows an element CD of the corrugated layer before (dotted) and after (solid) deformation due to applied forces and moments at point D. If forces H_D, V_D and moment M_D are applied at point D in Fig. 3 the reaction forces and moment at a cross-section C^1 will be N, T and M. In order to keep the corrugation element C–D in equilibrium the following equations must be fulfilled.

$$N = H_D \cos \phi + V_D \sin \phi \tag{2}$$

$$T = -H_D \sin \phi + V_D \cos \phi \tag{3}$$

$$M = H_D \left(\frac{h_c}{2} - \zeta \right) - V_D(p - \xi) + M_D \tag{4}$$

where ϕ is the slope at C

$$\phi = \frac{d\zeta}{d\xi} \tag{5}$$

The deformation of the corrugation element considered as a curved beam is considered next. It is assumed that the shear stresses are negligible and that the deformation is due primarily to the normal stresses. These stresses can be partitioned into two parts, σ_s due to the longitudinal force N and σ_b due to the bending moment M, see Fig. 4. The total stress is

$$\sigma = \sigma_s + \sigma_b \tag{6}$$

where

$$\sigma_s = \frac{N}{A_c} \tag{7}$$

Fig. 2. The centre line of a corrugation leg between a crest and a trough.
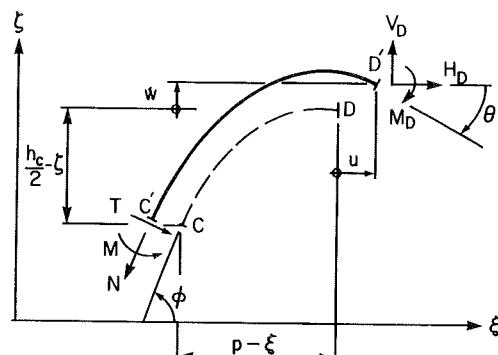
Fig. 3. A corrugation element CD before (dotted) and after C′D′ deformation (solid) due to applied forces and moments at D.
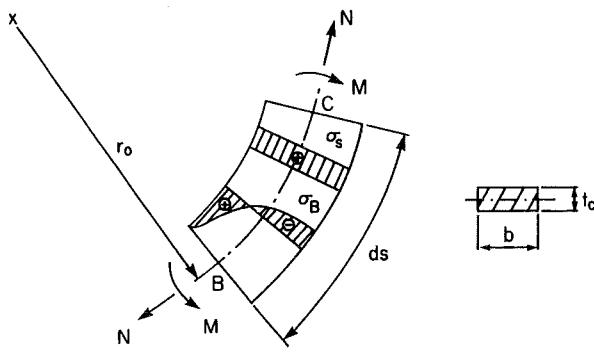
Fig. 4. Normal stresses σ_s and σ_b in a small element due to the longitudinal force N and bending moment M produce small changes in the radius of curvature r.

in which A_c is the cross-sectional area of the strip, $A_c = bt_c$.

The bending stress, σ_b, obtained from curved beam theory,[11] is

$$\sigma_b = -\frac{M}{A_c r_o} \qquad (8)$$

where r_o is the local radius of curvature. Hence the strain ε_s in a fibre along the centre line will depend not only on the force N but also on the bending moment M

$$\varepsilon_s = \frac{1}{E_c}\left(\frac{N}{A_c} - \frac{M}{A_c r_o}\right) \qquad (9)$$

where E_c is Young's modulus along the centre line of the strip.

The rotation of the cross-section at point C in Fig. 3, $d\phi$, due to the deformation of the element B–C in Fig. 4 is considered next. The length of the infinitesimal element B–C is denoted ds and the arc length of the centre line from A to D is denoted S, see Fig. 2. From curved beam theory[11] the rotation of cross-section C relative to cross-section B, Fig. 4, is

$$\frac{d\phi}{ds} = \frac{1}{r} - \frac{1}{r_o} + \frac{\varepsilon_s}{r_o} \qquad (10)$$

where the change in curvature upon moment application is

$$\frac{1}{r} - \frac{1}{r_o} = -\frac{M}{E_c J} \qquad (11)$$

J is the second moment of area of the cross-section $(I = bt_c^3/12)$ times a correction factor κ.[11]

κ is given as an infinite series in Ref. 11 and is reproduced herein as a truncated two term approximation

$$\kappa \approx 1 + \frac{3}{20}\left(\frac{t_c}{r_o}\right)^2 + \frac{3}{112}\left(\frac{t_c}{r_o}\right)^4 \qquad (12)$$

Substitution of (9) and (11) into (10) gives

$$\frac{d\phi}{ds} = -\left(\frac{1}{E_c J} + \frac{1}{E_c A_c r_o^2}\right) M + \frac{N}{E_c A_c r_o} \qquad (13)$$

The rotation $d\phi$ and elongation $\varepsilon_s\, ds$ at point C, Fig. 4, produce axial and vertical displacements du and dw and rotation $d\theta$ of point D in Fig. 3, due to rigid body motion of the section C–D. If the deformations and rotations along the centre line are small the displacements du and dw at D can be approximated as

$$du = \left[-\frac{d\phi}{ds}\left(\frac{h_c}{2} - \zeta\right) + \varepsilon_s \cos\phi\right]ds \qquad (14)$$

$$dw = \left[\frac{d\phi}{ds}(p - \xi) + \varepsilon_s \sin\phi\right]ds \qquad (15)$$

The rotation at D is

$$d\theta = \left[-\frac{d\phi}{ds}\right]ds \qquad (16)$$

Integration of eqns (14–16) over the arc length S, i.e. the distance between A and D along the centre line, gives the total displacements u, w and rotation θ

$$u = \int_S\left[-\frac{d\phi}{ds}\left(\frac{h_c}{2} - \zeta\right) + \varepsilon_s \cos\phi\right]ds \qquad (17)$$

$$w = \int_S\left[\frac{d\phi}{ds}(p - \xi) + \varepsilon_s \sin\phi\right]ds \qquad (18)$$

$$\theta = \int_S\left[-\frac{d\phi}{ds}\right]ds \qquad (19)$$

These three compatibility equations together with the constitutive relationships (9) and (13) and the equilibrium conditions (2) and (4) form a system of equations which connects the applied loads and moment at point D with the total displacements u, w and rotation θ.

$$\begin{bmatrix} u \\ w \\ \theta \end{bmatrix} = \frac{1}{E_c A_c} \begin{bmatrix} C_{11} & C_{12} & C_{13} \\ & C_{22} & C_{23} \\ \text{sym.} & & C_{33} \end{bmatrix} \begin{bmatrix} H_D \\ V_D \\ M_D \end{bmatrix} \qquad (20)$$

The coefficients C_{ij} in the compliance matrix are given in the Appendix.

If the facings are assumed rigid $(\theta = 0)$ and there is no thickness reduction of the core $(w = 0)$ this system of equations provides an upper bound on the transverse shear stiffness of the sandwich. These conditions in (20) gives

$$\begin{bmatrix} u \\ 0 \\ 0 \end{bmatrix} = \frac{1}{E_c A_c} [C] \begin{bmatrix} H_D \\ V_D \\ M_D \end{bmatrix} \qquad (21)$$

where $[C]$ denotes the compliance matrix. Elimination of V_D and M_D in the top row of (21) gives the relation between the shear force H_D and the horizontal displacement u as follows

$$\frac{H_D}{u} = E_c A_c \frac{\det[C_{sub}]}{\det[C]} \qquad (22)$$

where

$$[C_{sub}] = \begin{bmatrix} C_{22} & C_{23} \\ C_{23} & C_{33} \end{bmatrix} \qquad (23)$$

and $\det[\ ]$ denotes the determinant of the matrix. The effective transverse shear modulus G_{xz} is here defined as

$$G_{xz} = \frac{\tau_{xz}}{\gamma_{xz}} \qquad (24)$$

where

$$\tau_{xz} = \frac{H_D}{pb} \qquad (25)$$

and

$$\gamma_{xz} = \frac{u}{h} + \frac{w}{p} \qquad (26)$$

in which h is the distance between the facing midplanes, Fig. 1,

$$h = h_c + t_c + t_f \qquad (27)$$

Because the vertical displacement w is assumed zero it follows that

$$G_{xz} = \frac{h}{pb} \frac{H_D}{u} \qquad (28)$$

Substitution of H_D/u by (22) in (28) gives an expression connecting the transverse shear modulus G_{xz} with the Young's modulus of the corrugated layer

$$G_{xz} = \Gamma E_c \qquad (29)$$

where Γ is a dimensionless factor

$$\Gamma = \frac{h t_c}{p} \frac{\det[C_{sub}]}{\det[C]} \qquad (30)$$

For plates, replace E_c with $E_c/(1 - \nu_c^2)$, where ν_c is Poisson's ratio.[13]

Deformable facings

A shear loaded corrugated core sandwich with deformable facings will typically deform as indicated in Fig. 5. Points A and C, located on the planes of symmetry perpendicular to the x-axis, are fixed relative to the origin of the global coordinate system $x - z$, see Fig. 5. Five degrees of freedom u, w, θ_A, θ_B and θ_C may be identified. For a symmetric sandwich, however, the rotations at points A, B and C must be equal, thus reducing the number of degrees of freedom to three u, w and $\theta = \theta_A = \theta_B = \theta_C$.

To enable use of the previously derived eqn (20), the element shown in Fig. 5 is separated into two free body diagrams, see Fig. 6. Local coordinate systems (ξ_1, ζ_1) and (ξ_2, ζ_2) fixed in rotation relative to points A and C are introduced at the midplane of the sandwich. The local displacement components of point B in the local coordinate system are u_1, w_1, θ_1, and u_2, w_2, θ_2, see Fig. 6. For small rotations, $\theta \ll 1$, it is possible to
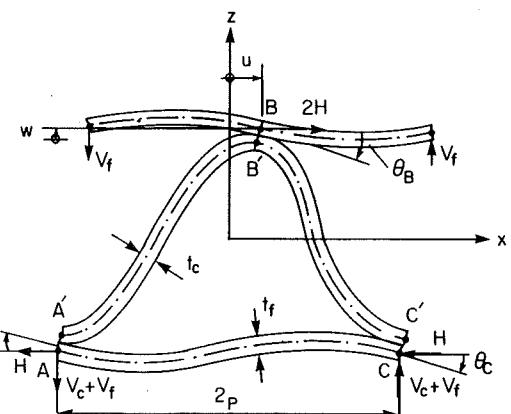

Fig. 5.   Deformation of shear loaded corrugated core sandwich.
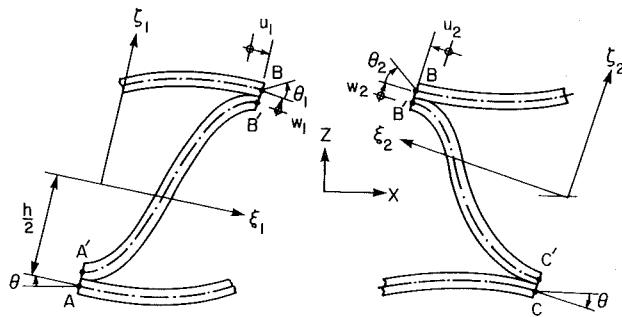
Fig. 6. Local coordinate systems $\xi_1 - \zeta_1$ and $\xi_2 - \zeta_2$ rotated an angle θ around points A and C. Local displacements and rotation are u_i and w_i and θ_i with $i = 1, 2$.

relate local and global displacements according to

$$u_1 = u - w\theta - h\theta \tag{31a}$$

$$w_1 = u\theta + w + p\theta \tag{31b}$$

$$\theta_1 = 0 \tag{31c}$$

$$u_2 = -u + w\theta + h\theta \tag{32a}$$

$$w_2 = u\theta + w - p\theta \tag{32b}$$

$$\theta_2 = 0 \tag{32c}$$

θ_1 and θ_2 must be zero because the cross-section at B does not rotate relative to the cross-sections at A and C as stated earlier.

Figure 7 shows the horizontal and vertical shear forces H, V_c and V_f in the global system acting on the structure and the resultant forces and moments acting on the top and bottom facings and the core in the form of a free-body diagram. The internal moments are found through equilibrium for the facing

$$M - p V_f = 0 \tag{33}$$

The moment equilibrium of the core (with $M = p V_f$) yields

$$\frac{h}{p} H - V_c - 2 V_f = 0 \tag{34}$$

The rotation θ at points A, B and C in Fig. 7 is determined by ordinary beam theory as

$$\theta = \frac{p^2 V_f}{3 E_f I_f} \tag{35}$$

where E_f is Young's modulus and I_f is the second moment of area of each facing

$$I_f = \frac{b t_f^3}{12} \tag{36}$$

The free-body diagrams shown in Fig. 6 and detailed in Fig. 8, give the connection between the global and local forces and moments. In the free-body diagram for the left region in Fig. 8, the forces and moment in the local coordinate system (ξ_1, ζ_1) are denoted by H_1, V_1 and M_1. H_2, V_2 and M_2 similarly denote local forces and moment in the (ξ_2, ζ_2)-system.

For small rotations, i.e. $\theta \ll 1$, $\sin \theta$ can be approximated by θ and $\cos \theta$ by 1; equilibrium of the element BB' demands

$$H_1 = H - V_c \theta \tag{37a}$$

$$V_1 = H\theta + V_c \tag{37b}$$

$$M_1 = -M - V_c \frac{t_f + t_c}{2} \theta + H \frac{t_f + t_c}{2} \tag{37c}$$

$$H_2 = -H - V_c \theta \tag{38a}$$

$$V_2 = H\theta - V_c \tag{38b}$$
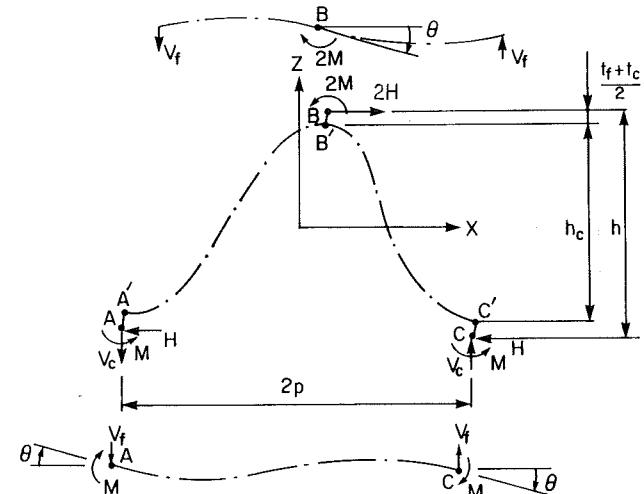
Fig. 7. Free-body diagram illustrating forces and moments acting on the facings and core of a shear loaded corrugated core sandwich.
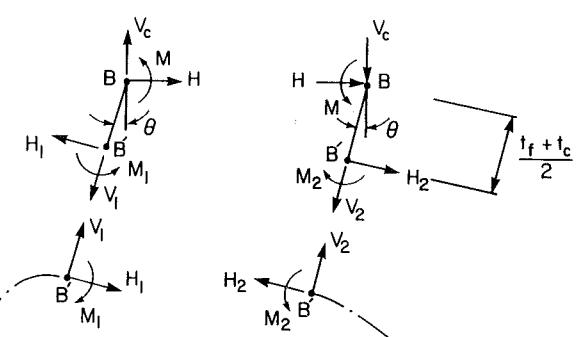
Fig. 8. Free-body diagram connecting local and global forces and moments.

$$M_2 = M - V_c \frac{t_f + t_c}{2} \theta - H \frac{t_f + t_c}{2} \qquad (38c)$$

$$\begin{bmatrix} u_i \\ w_i \\ \theta_i \end{bmatrix} = \frac{1}{E_c A_c} [C] \begin{bmatrix} H_i \\ V_i \\ M_i \end{bmatrix}, \quad i = 1, 2 \qquad (39)$$

At this state, eqn (21) can be applied to connect the local displacements and rotations with the local forces and moments.

The two local systems are assembled to a global system by subtracting (or equivalently adding) local displacements and forces for the two systems given by eqn (39),

$$\begin{bmatrix} u_1 - u_2 \\ w_1 - w_2 \\ \theta_1 - \theta_2 \end{bmatrix} = \frac{1}{E_c A_c} [C] \begin{bmatrix} H_1 - H_2 \\ V_1 - V_2 \\ M_1 - M_2 \end{bmatrix} \qquad (40)$$

Substitution of the local entities given by eqns (1, 2, 7, 8) into (41) yields the connection between global displacements and forces

$$u - w\theta - h\theta = \frac{1}{E_c A_c} \left[\left(C_{11} + \frac{t_f + t_c}{2} C_{13} \right) H + C_{12} V_c - pC_{13} V_f \right] \qquad (41a)$$

$$p\theta = \frac{1}{E_c A_c} \left[\left(C_{12} + \frac{t_f + t_c}{2} C_{23} \right) H + C_{22} V_c - pC_{23} V_f \right] \qquad (41b)$$

$$0 = \frac{1}{E_c A_c} \left[\left(C_{13} + \frac{t_f + t_c}{2} C_{33} \right) H + C_{23} V_c - pC_{33} V_f \right] \qquad (41c)$$

A relationship between the forces H, V_c and V_f may be obtained if eqns (34), (35), (41b) and (41c) are assembled into the following system of equations

$$\begin{bmatrix} \dfrac{h}{p} & -1 & -2 \\[2ex] C_{12} + \dfrac{t_f + t_c}{2} C_{23} & C_{22} & -\left(\dfrac{p^3 E_c A_c}{3 E_f I_f} + pC_{23} \right) \\[2ex] C_{13} + \dfrac{t_f + t_c}{2} C_{33} & C_{23} & -pC_{33} \end{bmatrix} \begin{bmatrix} H \\[2ex] V_c \\[2ex] V_f \end{bmatrix} = \begin{bmatrix} 0 \\[2ex] 0 \\[2ex] 0 \end{bmatrix} \qquad (42)$$

Multiplying the top row of the matrix above by C_{23} and adding it to the bottom row we obtain

$$\begin{bmatrix} \dfrac{h}{p} & -1 & -2 \\[2ex] C_{12} + \dfrac{t_f + t_c}{2} C_{23} & C_{22} & -\left(\dfrac{p^3 E_c A_c}{3 E_f I_f} + pC_{23} \right) \\[2ex] C_{13} + \dfrac{t_f + t_c}{2} C_{33} + \dfrac{h}{p} C_{23} & 0 & -(2C_{23} + pC_{33}) \end{bmatrix} \begin{bmatrix} H \\[2ex] V_c \\[2ex] V_f \end{bmatrix} = \begin{bmatrix} 0 \\[2ex] 0 \\[2ex] 0 \end{bmatrix} \qquad (43)$$

In the same manner we can eliminate C_{22} in the middle row of the matrix giving

$$\begin{bmatrix} \dfrac{h}{p} & -1 & -2 \\[3ex] C_{12}+\dfrac{t_f+t_c}{2}C_{23}+\dfrac{h}{p}C_{22} & 0 & -\left(\dfrac{p^2E_cA_c}{3E_fI_f}+pC_{23}+2C_{22}\right) \\[3ex] C_{13}+\dfrac{t_f+t_c}{2}C_{33}+\dfrac{h}{p}C_{23} & 0 & -(2C_{23}+pC_{33}) \end{bmatrix}\begin{bmatrix} H \\[3ex] V_c \\[3ex] V_f \end{bmatrix}=\begin{bmatrix} 0 \\[3ex] 0 \\[3ex] 0 \end{bmatrix} \qquad (44)$$

By symmetry arguments it may be shown that a non-trivial solution to (44) is given by

$$C_{13}+\frac{t_f+t_c}{2}C_{33}+\frac{h}{p}C_{23}=0 \qquad (45a)$$

and

$$2C_{23}+pC_{33}=0 \qquad (45b)$$

Thus the system (44) reduces to two equations

$$\frac{h}{p}H-V_c-2V_f=0 \qquad (46a)$$

$$\left(C_{12}+\frac{t_f+t_c}{2}C_{23}+\frac{h}{p}C_{22}\right)H-\left(\frac{p^3E_cA_c}{3E_fI_f}+2C_{22}\right)V_f=0 \qquad (46b)$$

From these equations we can express the vertical shear forces V_c and V_f in the horizontal shear force H

$$V_c=D_1H \qquad (47a)$$

$$V_f=D_2H \qquad (47b)$$

$$D_1=\frac{h}{p}-2D_2 \qquad (47c)$$

where

$$D_2=\frac{C_{12}+\dfrac{t_f+t_f}{2}C_{23}+\dfrac{h}{p}C_{22}}{\dfrac{p^2E_cA_c}{3E_fI_f}+pC_{23}+2C_{22}} \qquad (47d)$$

Substitution of (47) and θ given by (35) into (41a) and neglecting the second order term $w\theta$ we obtain

$$u=\frac{D_3}{E_cA_c}H \qquad (48)$$

where

$$D_3=C_{11}+\frac{t_f+t_c}{2}C_{13}+C_{12}D_1+\left(\frac{p^2hE_cA_c}{3E_fI_f}-pC_{13}\right)D_2 \qquad (49)$$

From (31) and (32) we obtain

$$w_1 + w_2 = 2u\theta + 2w = \frac{2\theta}{E_c A_c} \left[C_{22}H - \left(C_{12} + \frac{t_f + t_c}{2} C_{23} \right) V_c \right] \tag{50}$$

Rearranging the equation above and substituting u and V_c of (47a) and (48) give

$$w = \frac{\theta}{E_c A_c} \left[C_{22} - \left(C_{12} + \frac{t_f + t_c}{2} C_{23} \right) D_1 - D_3 \right] H \tag{51}$$

The rotation θ can be found from (35) after substitution of V_f of (47b) as

$$\theta = \frac{p^2 D_2}{3 E_f I_f} H \tag{52}$$

Now all the global displacements and rotations u, w and θ are expressed as functions of the horizontal shear force H.

As illustrated in Fig. 5, only the horizontal displacement contributes to the shear deformation. Thus the effective transverse shear modulus G_{xz} can be expressed as

$$G_{xz} = \frac{\tau_{xz}}{\gamma_{xz}} = \frac{H/bp}{u/h} \tag{53}$$

A non-dimensional shear modulus factor, Γ^*, may be defined as

$$\Gamma^* = G_{xz}/E_c \tag{54}$$

From eqns (48) and (53), Γ^* is obtained as

$$\Gamma^* = \frac{h t_c}{p D_3} \tag{55}$$

Thus, Γ^* depends on the geometry and dimensions of the constituents and the ratio between the Young's moduli of the facings and the corrugated layer. For plates, replace E_c and E_f with $E_c/(1 - \nu_c^2)$ and $E_f/(1 - \nu_f^2)$. It may be verfieid that $\Gamma^* \to \Gamma$ with increased facing stiffness (Γ is defined in eqn (29)).

An approximate expression for the transverse shear modulus G_{yz}

If it is assumed that the entire bending moment is carried by the facings and the shear force by the core when the corrugated board is subjected to bending, the transverse shear deformation δ_{yz} can be modelled as shown in Fig. 9.[9] The transverse shear force T_{yz} which is transmitted through the core will be

$$T_{yz} = pb\tau_{yz} \tag{56}$$

If G_{12} is the inplane shear modulus of the corrugated layer, the transverse shear deformation δ_{yz} will be

$$\delta_{yz} = \frac{S T_{yz}}{b t_c G_{12}} \tag{57}$$

where S is the arc length between a crest and a trough.

The transverse shear modulus G_{yz} is defined as

$$G_{yz} = \frac{h T_{yz}}{\delta_{yz} p b} \tag{58}$$

Substituting (56) and (57) into (58), G_{yz} is obtained as

$$G_{yz} = \frac{ht_c}{pS} G_{12}$$ (59)

COMPARISON WITH OTHER METHODS AND NUMERICAL EXAMPLES

To examine the validity of the approach described, the effective transverse shear modulus, G_{xz}, was calculated numerically for circular and triangular cores using the ANSYS finite element code.[12] Two-noded elastic beam elements (STIF 3) were used to model 1 wavelength of the sandwich. Twenty elements were used to model the core and ten for the each of the facings. The core and the facings were rigidly connected to represent an ideal bond. Loads and boundary conditions were applied as shown in Fig. 5. The effective shear modulus for a circular-straight core sandwich, Fig. 10, was extracted from the design curves of Libove and Hubka,[9] and compared ith the present analysis.

The effective transverse shear modulus, G_{xz}, is best quantified by the non-dimensional factor Γ^* defined in eqn (54). Γ^* was calculated using the following dimensional parameters: $p = h_c$, $t_c = t_f = p/20$, $R = p/2$ for the circular core, while $R = 0.18\ p$ and $\theta = 60°$ was used for the circular-straight core. Furthermore, the elastic moduli for the core material and the facings were set equal, $E_c = E_f$.

Table 1 summarizes the results from the Γ^* calculations based on the present analysis, finite elements and Libove and Hubka.[9] Very close agreement is observed between the various analysis methods which supports the validity of the present analysis. The small difference (2%) between the Libove and Hubka's[9] results based on straight beam segments and the present results, based on curved beam theory, is evidently due to the straight core geometry considered, Fig. 10(b), and the slender core members. Larger differences are expected for more curved and less slender core members.

To illustrate the influence of core geometry and deformable facing, the shear modulus coefficients Γ^* and Γ were calculated for the core shapes shown in Fig. 10. As discussed earlier in this paper, Γ^* contains contributions from deformations of both facings and core while Γ represents the upper bound on G_{xz} assuming rigid facings. Γ and Γ^* were calculated using the same dimen-
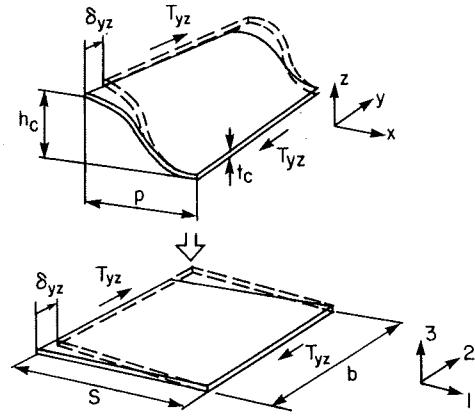

Fig. 9. Transverse shear loading of the corrugated core.
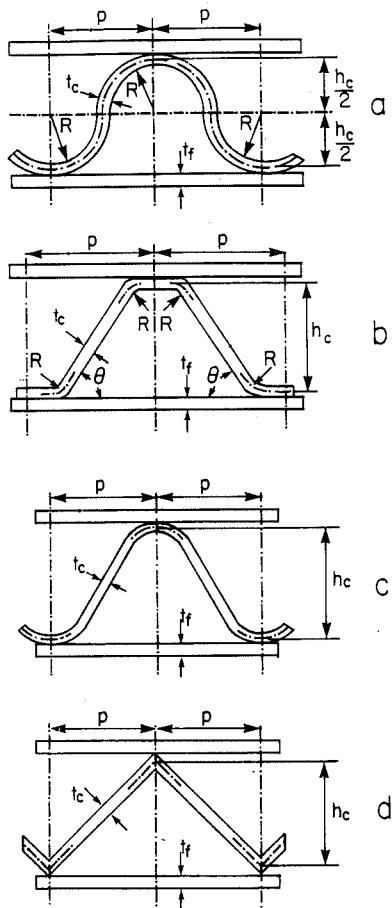
**Fig. 10.** Various core shapes: (a) circular; (b) circular-straight; (c) sinusoidal; (d) triangular.

Table 1. Shear modulus coefficient Γ^* for various core shapes obtained by the present analysis, finite elements and Libove and Hubka[9]

	Circular	Circular–straight	Triangular
Present analysis	$0{\cdot}430 \times 10^{-3}$	$0{\cdot}961 \times 10^{-3}$	$8{\cdot}72 \times 10^{-3}$
Finite elements	$0{\cdot}433 \times 10^{-3}$		$8{\cdot}53 \times 10^{-3}$
Libove and Hubka		$0{\cdot}982 \times 10^{-3}$	
Difference (%)	$0{\cdot}65$	$2{\cdot}00$	$-2{\cdot}20$

Table 2. Shear modulus coefficients Γ and Γ^* for various core shapes and reduction in transverse shear modulus G_{xz} due to deformable facings

	Circular	Circular–straight	Sinusoidal	Triangular
$\Gamma \times 10^3$	0·531	1·52	3·77	19·5
$\Gamma^* \times 10^3$	0·430	0·961	2·75	8·72
Reduction in G_{xz} (%)	19·4	37·1	27·1	55·2

Table 3. G_{yz}/E_c and G_{yz}/G_{xz} for various core shapes

	Circular	Circular–straight	Sinusoidal	Triangular
$G_{yz}/E_c \times 10^3$	12·3	12·5	13·2	14·0
G_{yz}/G_{xz}	28·5	13·0	4·8	1·6

sional parameters as for Table 1. Table 2 summarizes Γ and Γ^* for the various core geometries shown in Fig. 10, and the reduction in G_{xz} due to deformable facings. The results show that the effective transverse shear modulus, G_{xz}, is a small fraction of the core elastic modulus. G_{xz} is highly sensitive to the shape of the corrugations. It is observed that the stiffest core shape (triangular) is an order of magnitude stiffer than the most flexible shape (circular). Furthermore, G_{xz} is very sensitive to deformations of the facings, especially for the triangular core where facing flexibility reduces G_{13} by more than a factor of two.

The shear modulus along the corrugations, G_{yz}, was considered next. G_{yz} was calculated from eqn (56) for the core shapes shown in Fig. 10 using the same dimensional parameters as for Tables 1 and 2. For simplicity, the core and facing were assumed isotropic ($\nu = 0{\cdot}3$). Table 3 shows G_{yz} normalized with $E_c (= E_f)$ and G_{xz}. The results show that G_{yz} is also a small fraction of the elastic modulus of the corrugated layer, and in contrast to G_{xz} not highly sensitive to the core shape. Inspection of the ratio G_{yx}/G_{xz} shows that G_{yz} exceeds G_{xz} and that the transverse shear modulus of corrugated core sandwich plates may be highly anisotropic. For orthotropic core materials like paper, where the stiffer direction is along the

x-axis, less anisotropy than shown in Table 3 is expected.

CONCLUSIONS

An analysis of the transverse shear modulus G_{xz} for various corrugated core structures has been derived using curved beam theory. An approximate formula for the transverse shear modulus G_{yz} was derived based on deformation of the core only. The analysis is in good agreement with finite elements and previous analysis. An upper limit of the transverse shear modulus G_{xz} was found by assuming rigid facings. The reduction of the transverse shear modulus G_{xz} due to elastic facing was quantified. For the core and facing materials and geometries investigated the reduction of G_{xz} was between 20 and 50%. If the bonds between the facings and the core are flexible there will be additional losses. The transverse shear modulus G_{xz} was found to be very sensitive to the corrugation shape and the stiffest core had an effective transverse shear modulus which was 20 times larger than that of the most flexible core. The transverse shear modulus G_{yz} was found to be larger than G_{xz} and less sensitive to the corrugation shape.

REFERENCES

1. Godshall, W. D., Corrugated fiberboard standardization issues. *ASTM Standardization News* (November 1989) 26-9.
2. McKee, R. C., Gander, J. W. & Wachuta, J. R., Compression strength formula for corrugated boxes. *Paperboard Packaging,* **48** (1963) 149-59.
3. Hahn, E. K., Carlsson, L. A. & Westerlind, B. S., Edge compression test fixture for buckling studies of corrugated board panels. *Experimental Mechanics* (in press).
4. Hahn, E. K., Ruvo, A. de, Westerlind, B. S. & Carlsson, L. A., Compressive strength of edge loaded corrugated board panels. *Experimental Mechanics* (in press).
5. Bert, C. W. & Chang, S., Shear-flexible orthotropic plates loaded in plane. *Journal of the Engineering Mechanics Division, Proceedings of the American Society of Civil Engineers,* **98** (EM6) (December 1972) 1499-509.
6. Allen, H. G., *Analysis and Design of Structural Sandwich Panels.* Pergamon Press, Oxford, 1969.
7. Folie, G. M., The behaviour and analysis of orthotropic sandwich plates. *Building Science,* **6** (1971) 57-67.
8. Plantema, F. J., *Sandwich Construction.* John Wiely, New York, 1966.
9. Libove, C. & Hubka, R. E., *Elastic Constants for Corrugated Core Sandwich Plates.* NACA TN 2289, 1951.
10. Ko, W. L., Elastic constants for superplastically formed/diffusion-bonded sandwich structures. *AIAA Journal,* **18** (1980) 986-7.
11. Timoshenko, S., *Strength of Materials, Vol. 1.* Krieger, Malabar, 1976, pp. 362-9.
12. *ANSYS User's Manual, DN-R144.* Swanson Analysis Systems Inc., Houston, PA, 1989.
13. Timoshenko, S. & Woinowky-Krieger, S., *Theory of Plates and Shells,* 2nd edn. McGraw-Hill, New York, 1987.

APPENDIX

Substitution of N and M in eqn (9) by the expressions given in eqns (2) and (4) gives

$$\varepsilon_s = \frac{1}{E_c A_c} \left\{ \left[-\frac{1}{r_o}\left(\frac{h_c}{2}-\zeta\right) + \cos\phi \right] H_D + \left[\frac{1}{r_o}(p-\xi) + \sin\phi \right] V_D - \frac{M_D}{r_o} \right\} \tag{A1}$$

Substitution of bt_c with A_c in eqn (12) gives

$$J = \frac{\kappa t_c^2}{12} A_c \tag{A2}$$

Making the same substitution as in (A1) for (13) and using the expression given in (A2) we obtain

$$\frac{d\phi}{ds} = \frac{1}{E_c A_c} \left\{ \left[-\left(\frac{12}{\kappa t_c^2}+\frac{1}{r_o^2}\right)\left(\frac{h_c}{2}-\zeta\right) + \frac{\cos\phi}{r_o} \right] H_D + \left[\left(\frac{12}{\kappa t_c^2}+\frac{1}{r_o^2}\right)(p-\zeta) + \frac{\sin\phi}{r_o} \right] V_D - \left(\frac{12}{\kappa t_c^2}+\frac{1}{r_o^2}\right) M_D \right\} \tag{A3}$$

Inserting the expressions (A1) and (A2) for ε_s and $d\phi/ds$ in (14)-(16) gives

$$du = \frac{ds}{E_c A_c} \left\{ \left[\left(\frac{12}{\kappa t_c^2}+\frac{1}{r_o^2}\right)\left(\frac{h_c}{2}-\zeta\right)^2 - 2\frac{\cos\phi}{r_o}\left(\frac{h_c}{2}-\zeta\right) + \cos^2\phi \right] H_D \right.$$

$$+ \left[-\left(\frac{12}{\kappa t_c^2}+\frac{1}{r_o^2}\right)(p-\xi)\left(\frac{h_c}{2}-\zeta\right) + \frac{\cos\phi}{r_o}(p-\xi)\frac{\sin\phi}{r_o}\left(\frac{h_c}{2}-\zeta\right) + \cos\phi\sin\phi \right] V_D$$

$$\left. + \left[\left(\frac{12}{\kappa t_c^2}+\frac{1}{r_o^2}\right)\left(\frac{h_c}{2}-\zeta\right) - \frac{\cos\phi}{r_o} \right] M_D \right\} \tag{A4}$$

$$dw = \frac{ds}{E_c A_c} \left\{ \left[-\left(\frac{12}{\kappa t_c^2} + \frac{1}{r_o^2} \right)(p - \xi)\left(\frac{h_c}{2} - \zeta \right) + \frac{\cos \phi}{r_o}(p - \xi) - \frac{\sin \phi}{r_o}\left(\frac{h_c}{2} - \zeta \right) + \cos \phi \sin \phi \right] H_D \right.$$

$$+ \left[\left(\frac{12}{\kappa t_c^2} + \frac{1}{r_o^r} \right)(p - \xi)^2 + 2\frac{\sin \phi}{r_o}(p - \xi) + \sin^2 \phi \right] V_D + \left[-\left(\frac{12}{\kappa t_c^2} + \frac{1}{r_o^2} \right)(p - \xi) - \frac{\sin \phi}{r_o} \right] M_D \right\} \qquad (A5)$$

$$d\theta = \frac{ds}{E_c A_c} \left\{ \left[\left(\frac{12}{\kappa t_c^2} + \frac{1}{r_o^2} \right)\left(\frac{h_c}{2} - \zeta \right) - \frac{\cos \phi}{r_o} \right] H_D + \left[-\left(\frac{12}{\kappa t_c^2} + \frac{1}{r_o^2} \right)(p - \xi) - \frac{\sin \phi}{r_o} \right] V_D + \left[\frac{12}{\kappa t_c^2} + \frac{1}{r_o^2} \right] M_D \right\} \quad (A6)$$

Integration of all the individual terms in (A4)–(A6) over the arc length S gives the total displacements and rotation at point B in Fig. 3 as follows

$$u = \frac{1}{E_c A_c} \{ [k_5 - 2k_9 + k_{13}] H_D + [-k_6 + k_8 - k_{12} + k_{15}] V_D + [k_3 - k_7] M_D \} \qquad (A7)$$

$$w = \frac{1}{E_c A_c} \{ [-k_6 + k_8 - k_{12} + k_{15}] H_D + [k_4 + 2k_{11} + k_{14}] V_D + [-k_2 - k_{10}] M_D \} \qquad (A8)$$

$$\theta = \frac{1}{E_c A_c} \{ [k_3 - k_7] H_D + [-k_2 - k_{10}] V_D + k_1 M_D \} \qquad (A9)$$

where

$$k_1 = \int_s \left(\frac{12}{\kappa t_c^2} + \frac{1}{r_o^2} \right) ds, \qquad\qquad k_2 = \int_s \left(\frac{12}{\kappa t_c^2} + \frac{1}{r_o^2} \right)(p - \xi)\, ds,$$

$$k_3 = \int_s \left(\frac{12}{\kappa t_c^2} + \frac{1}{r_o^2} \right)\left(\frac{h_c}{2} - \zeta \right) ds, \qquad\qquad k_4 = \int_s \left(\frac{12}{\kappa t_c^2} + \frac{1}{r_o^2} \right)(p - \xi)^2\, ds,$$

$$k_5 = \int_s \left(\frac{12}{\kappa t_c^2} + \frac{1}{r_o^2} \right)\left(\frac{h_c}{2} - \zeta \right)^2 ds, \qquad\qquad k_6 = \int_s \left(\frac{12}{\kappa t_c^2} + \frac{1}{r_o^2} \right)(p - \xi)\left(\frac{h_c}{2} - \zeta \right) ds,$$

$$k_7 = \int_s \frac{\cos \phi}{r_o}\, ds, \qquad\qquad k_8 = \int_s \frac{\cos \phi}{r_o}(p - \xi)\, ds,$$

$$k_9 = \int_s \frac{\cos \phi}{r_o}\left(\frac{h_c}{2} - \zeta \right) ds, \qquad\qquad k_{10} = \int_s \frac{\sin \phi}{r_o}\, ds,$$

$$k_{11} = \int_s \frac{\sin \phi}{r_o}(p - \xi)\, ds, \qquad\qquad k_{12} = \int_s \frac{\sin \phi}{r_o}\left(\frac{h_c}{2} - \zeta \right) ds,$$

$$k_{13} = \int_s \cos^2 \phi\, ds, \qquad\qquad k_{14} = \int_s \sin^2 \phi\, ds,$$

$$k_{15} = \int_s \cos \phi \sin \phi\, ds$$

Writing (A6)–(A8) in matrix form yields eqn (21) as

$$\begin{bmatrix} u \\ w \\ \theta \end{bmatrix} = \frac{1}{E_c A_c} \begin{bmatrix} C_{11} & C_{12} & C_{13} \\ & C_{22} & C_{23} \\ \text{sym.} & & C_{33} \end{bmatrix} \begin{bmatrix} H_D \\ V_D \\ M_D \end{bmatrix}$$

were

$$C_{11} = k_5 - 2k_9 + k_{13}$$
$$C_{12} = k_6 + k_8 - k_{12} + k_{15}$$
$$C_{13} = k_3 - k_7$$
$$C_{22} = k_4 + 2k_{11} + k_{14}$$
$$C_{23} = -k_2 - k_{10}$$
$$C_{33} = k_1$$

Paper 2

———

Evaluation of Transverse Shear Stiffness of Structural Core Sandwich Plates

by

T. Nordstrand and Carlsson, L.A.

Composite Structures, Vol. 37, pp. 145-153, 1997.

Evaluation of transverse shear stiffness of structural core sandwich plates

T. M. Nordstrand[a] & L. A. Carlsson[b]

[a]*Paper Physics and Fibre Technology, SCA Research, Sundsvall, Sweden*
[b]*Department of Mechanical Engineering, Florida Atlantic University, Boca Raton, Florida, USA*

Effective transverse shear moduli in the principal material directions of corrugated board were examined experimentally for five corrugated board types using the ASTM block shear test and the three-point bend test. It was found that shear moduli determined by the three-point bend test are significantly lower than those obtained from the block shear test. The difference is probably caused by local indentation of the board at the supports and contribution from bending deformation of the facings in the three-point bend test. Experimental results were compared to shear moduli obtained by finite-element analysis (FEA) and analytical predictions. Shear modulus along the corrugations, determined with the three-point bend test, was about half of the predicted value using FEA, while the shear modulus transverse to the corrugations was substantially below that prediction from FEA, apparently due to delamination damage of the core material inflicted during the corrugation process. © 1997 Elsevier Science Ltd.

INTRODUCTION

Corrugated board (Fig. 1) is an efficient low-cost structural material that is widely used for transporting, storing and distributing goods. As shown in Fig. 1, the corrugations are directed along the cross-direction (CD) of each of the constituents. The bending stiffness of the board is generally much larger transverse to the corrugations, i.e. in the machine-direction (MD), than in the CD[1], while the reverse is true for the out-of-plane shear stiffnesses [2,3]. This means that the direction of large bending stiffness (MD) coincides with the direction of low

Fig. 1. Corrugated core sandwich. MD and CD denote machine- and cross-directions, respectively.

transverse shear stiffness, which may lead to substantial shear deformation of transversely loaded sandwich panels. For a corrugated core plate this means that the overall structural stiffness and stability may suffer due to low MD shear rigidity. In addition to the inherent low transverse shear rigidity in the MD, the corrugating process is known to cause delamination damage to the core material (fluting) resulting in further structural performance losses [4].

In a previous study [2] analytical models based on mechanics of materials principles were presented for calculation of the transverse shear moduli of corrugated board. The analysis is based on the geometry of the core, thickness and material properties of the constituents, measured prior to the corrugation process. The corrugation process, however, is known to substantially damage the core due to the severe mechanical deformations encountered as shown by Whitsitt & Sprague [4]. In particular the integrity of the material at the crest and trough of the core may suffer due to delamination damage [4], which is also likely to degrade the

transverse shear moduli of the board. It is therefore of importance for designers of corrugated packages to know how the performance of the corrugated board is influenced by the degradation of the core.

In this study, transverse shear stiffnesses of five commercial corrugated board types are examined experimentally using two test methods for determining shear moduli, i.e. the ASTM C273-61 block shear test and the three-point bend (TPB) test, ASTM C393-62. Test results will be compared to predicted shear moduli using a previously derived methodology [2] and FEA [5].

EVALUATION OF BENDING AND SHEAR RIGIDITIES

Two test methods were utilized to measure transverse shear stiffness in the principal directions of the board (MD and CD), viz. the block shear test ASTM C273-61 (Fig. 2) and the three-point bend test (Fig. 3) described in ASTM standard C393-62.

Transverse shear deformation of a sandwich panel is illustrated in Fig. 4. Shear stress, τ_{iz}, with $i = x$, y, is acting on the facings that are assumed to be rigid in shear. The shear displacement, u_i, is then given by

$$u_i = c\gamma_{c,i} = H\gamma_{a,i}, \quad i = x, y \tag{1}$$

with x and y denoting MD and CD, respectively. Constants c and H are the core and total sandwich thickness, respectively, and $\gamma_{c,i}$ and $\gamma_{a,i}$ are
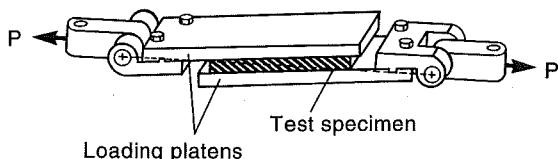
Fig. 2. Block shear test principle.
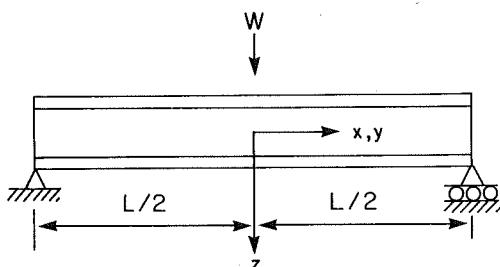
Fig. 3. Principle of the three-point bend test.
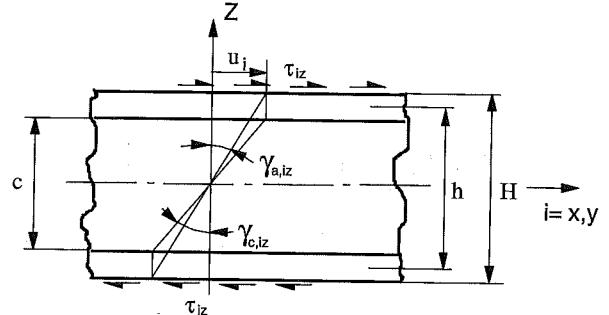
Fig. 4. Illustration of transverse shear deformation in a sandwich panel.

the core and average shear strains, respectively (Fig. 4). The corresponding effective shear moduli in MD and CD are defined by

$$G_{c,iz} = \frac{\tau_{iz}}{\gamma_{c,iz}} = \frac{c}{H}\frac{\tau_{iz}}{\gamma_{a,iz}} = \frac{c}{H}G_{a,iz}, \quad i = x, y \tag{2}$$

The effective shear moduli for a corrugated core, $G_{c,iz}$, defined in this manner represent those for an equivalent homogeneous core material, see Nordstrand et al. [2]. The average transverse shear moduli, $G_{a,iz}$, will be slightly higher. The block shear test (Fig. 2) is specifically designed to measure the shear properties of sandwich panels and core materials, and has been standardized by the ASTM [6]. The line of load application is slightly tilted with respect to the specimen midplane so that the line of load action is in the sandwich diagonal plane. By this design the applied load causes an opening moment that counteracts the closing moment which tends to reduce the thickness of the specimen. It is recognized that a state of pure shear is not achieved by this design. However, by suitable design it is possible to minimize the influence of secondary stresses and end effects.

The three-point bend (TPB) test geometry (Fig. 3) provides a combination of bending and shear deformation. The sandwich beam is subjected to bending by the lateral force W and the shear force of magnitude $W/2$ will cause transverse shear deformation that contributes to the overall beam deflection. In thin facing sandwich beam theory [7], the shear force is assumed to be entirely carried by the core and the bending stiffnesses of the facings are assumed to be negligible. For this situation, the vertical deflection, Δ, under the central load, W, becomes [8]

$$\Delta = \frac{WL^3}{48bD_i} + \frac{WL}{4AG_{c,iz}} \tag{3}$$

where L is the beam span length, D_i, is the flexural rigidity per unit width of the beam and $AG_{c,iz}$ is the shear stiffness of the sandwich. The effective shear area of the beam cross-section is $A = bh^2/c$, where b is the beam width and h the distance between the centre lines of the facings. Equation (3) provides a basis for experimental determination of bending and shear rigidities from two plots of the beam compliance [7], see Fig. 5. Figure 5(a) shows Δ/WL plotted vs L^2. The slope of the line provides a good estimate of the value $1/48bD_i$, while the extrapolated intercept on the abscissa approximately yields $1/4AG_{c,iz}$. Figure 5(b) shows Δ/WL^3 plotted vs $1/L^2$. The slope of the line provides a good estimate of $1/4AGC_{c,iz}$, while the intercept is an approximate value of $1/48bD_i$ [7]. The evaluation of bending and shear rigidities according to the above procedure requires that the faces count as 'thin' which implies that the local flexural rigidity of the facings is negligible compared to the total bending stiffness, D_i. Moreover, local deformations, 'denting', at the load introduction and support regions may add to the apparent beam compliance (Δ/W) [9]

Fig. 6. Unit cell of corrugated board modelled by key-points and area elements.

which is not accounted for in the data reduction procedure above (eqn (3)).

FINITE-ELEMENT ANALYSIS

Finite-element analysis was performed on the three-point bend test to validate test results. A finite-element model of an 'unit cell' of the board was first constructed, see Fig. 6. The 'unit cell' consists of two outer facings of thickness t_f, separated by a corrugated core of thickness C. The corrugated medium has a thickness of t_c and the corrugations are assumed sinusoidal in shape with a wavelength of $2p$. Thus, the length of the unit cell is $4p$ and the width was set to $2p$.

The finite element used is based on the standard eight-node isoparametric shell formulation given by Ahmad *et al.* [10], see Fig. 7. In the ANSYS code [5] the element is denoted STIF93. The quadratic shape functions, which describe both shape and displacements of the element, allow modelling of curved structures such as the corrugated core. The element formulation includes orthotropic linear elastic material behaviour, with the principal axis of elastic symmetry aligned with the curvilinear element coordinate system $x_e-y_e-z_e$, shown in Fig. 1.

Fig. 5. Plots for evaluation of bending and shear stiffness from three-point bend specimen compliance.
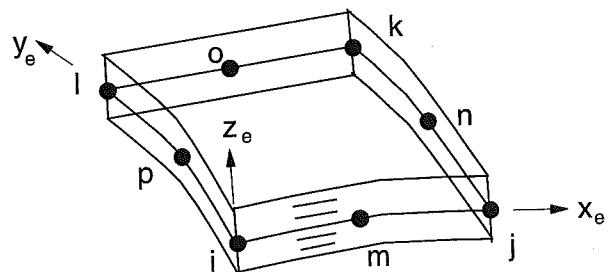
**Fig. 7.** Eight-node isoparametric shell element, STIF93.
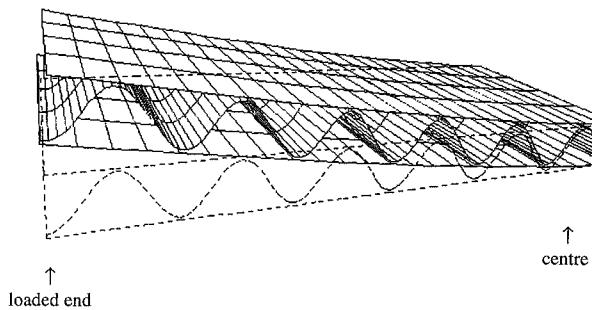
Fig. 8. Deformation of the finite-element model in three-
point bending.

The finite-element model of the corrugated
board (Fig. 8) was generated by an assembly of
'unit cells'. The areas generated were meshed
with STIF93 elements using divisions of 2 along
the width of the unit cell, 8 along the length of
the facings and 40 along the length of the
corrugations. As the model consists of two-
dimensional elements, a distance of half the
thickness of the facing and core sheet separated
the three entities. Rigid connections between
the nodes on the tips of the corrugated core
and the facings were applied using constraint
equations between the separate degrees of free-
dom in each node pair of core and facing [5].

Finite-element models of corrugated board
specimens of various lengths were generated by
connecting several 'unit cells' in the MD and
CD. In the MD specimens 2 unit cells were
connected along the width, and 2.5, 3 and 4 unit
cells were connected along the MD. The CD
specimens employed 1.5, 2, 3, 4 and 5 unit cells
along the beam length and 2 unit cells for the
width dimension. Thus, all beam models were
$8p$ in width. In the MD the beam length varied
between $10p$ and $16p$, and in the CD between
$6p$ and $20p$.

Symmetry of the three-point bend test (Fig.
3) allowed modelling of only half of the speci-
men. Thus, the beam was 'cut' at the centre

section and the top and bottom facings were
fixed in rotation on the right-hand side in Fig. 8,
while axial displacement of the entire cross-sec-
tion of the beam was prevented. Only the
bottom facing was laterally supported allowing
thickness changes of the beam at the centre
section. Loading was accomplished by applica-
tion of a uniform lateral displacement of the
nodes of the cross-section at the beam end.

Material properties and geometry considered
in the finite-element modelling are the actual
ones listed in Tables 1 and 2. The in-plane
shear modulus of the fluting is calculated using
Baum's approximation [11] as follows

$$G_{12,\text{flute}} = 0.387\sqrt{E_{\text{MD, flute}}E_{\text{CD, flute}}} \qquad (4)$$

After applying the boundary conditions, analysis
was performed using the frontal solver in the
ANSYS program [5]. The lateral nodal loads at
the simply supported end were added and the
applied displacement was divided by twice the
total load to yield the beam compliance. The
bending and shear rigidities of the beams were
evaluated according to Fig. 5, using the beam
compliance evaluated from the finite-element
analysis and the span length of the structure in
Fig. 3. Figure 8 shows the deformed finite-
element mesh for a board specimen loaded in
the MD.

EXPERIMENTS

Materials

Five corrugated boards were examined. All
boards were manufactured by SCA Packaging,
Sweden, and are denoted 140B, 140C, 160C,
530C (all single wall) and 210BC (double-wall).
'B' and 'C' represent different fluting (core)

**Table 1. Composition (grammage in g/m^2, type of fibre) and characteristics of corrugated boards. WK, SC and K denote
white kraft, semi-chemical (NSSC) and kraft fibres, respectively. The $\pm$ range represents 1 standard deviation.
Wavelengths for B- and C-flutes are 6.08 and 7.26 mm, respectively**

Board	Composition (g/m²)	Total grammage (mm)	Board thickness, H (mm)	Flute height, C^1 (mm)
140B	140WK/112SC/140K	435 ± 3	2.86 ± 0.01	2.50
140C	140WK/112SC/140K	448 ± 3	3.91 ± 0.01	3.50
160C	200WK/112SC/186K	556 ± 5	4.02 ± 0.03	3.50
530C	300WK/150SC/200K	689 ± 5	4.21 ± 0.02	3.50
210BC	140WK/112SC/112SC/ 112SC/140K	701 ± 5	6.52 ± 0.03	2.50, 3.50

[1]Nominal flute height, see Fig. 1.

Table 2. Thickness, t (mm) and principal Young's moduli, E (GPa) for the board constituents

Board	Property	Ply number				
		1	2	3	4	5
140B	t	0.204	0.205	0.172	—	—
	E_{MD}	8.37	5.42	10.76	—	—
	E_{CD}	2.89	2.14	2.95	—	—
140C	t	0.211	0.185	0.169	—	—
	E_{MD}	8.01	7.10	10.4	—	—
	E_{CD}	2.78	2.39	2.63	—	—
160C	t	0.268	0.217	0.244	—	—
	E_{MD}	7.98	4.75	8.09	—	—
	E_{CD}	3.19	1.56	2.49	—	—
530C	t	0.240	0.283	0.369	—	—
	E_{MD}	8.20	4.75	6.70	—	—
	E_{CD}	2.85	1.85	2.78	—	—
210BC	t	0.203	0.206	0.210	0.212	0.173
	E_{MD}	7.86	5.31	5.12	5.25	9.28
	E_{CD}	2.18	1.94	1.69	1.69	2.47

geometry. The liners were made from chemical kraft fibres and the fluting from neutral sulphite, semi-chemical pulp (NSSC). Table 1 presents compositions (lay-ups), total grammages and thickness of the boards. Thickness, t, and Young's moduli, E_{MD} and E_{CD}, of each constituent (before corrugation) were measured using standard test methods [12,13] (Table 2). The data listed are averages from 10 specimens.

Test procedures

According to the ASTM [6], the width of the block shear specimen should exceed twice its thickness while the length should exceed 12 times the thickness. Rectangular board specimens, 12 cm long and 8 cm wide, were cut from large corrugated board panels with the edges aligned with the CD and MD. The specimens were glued to the loading blocks with a two-component epoxy glue (Loctite) that cures in a couple of minutes at room temperature conditions. To achieve good adhesion and alignment of the board specimen with respect to the loading blocks, a special specimen preparation fixture was used. After adhesive bonding, the specimens were conditioned at 23°C and 50% RH for at least 24 h before testing in this environment. The loading platens were 162 mm long, 100 mm wide and 6 mm thick and made from aluminium. Figure 9 shows the block shear test fixture mounted in a 10 kN Alwetron TCT10 test machine. The crosshead speed was 3 mm/min.

Shear loading is accomplished by application of a tensile load, P. For evaluation of shear

strain, the horizontal displacement, u, was measured with an inductive displacement transducer (Feinpruf Mahr, type 1300) applied directly to the specimen (see Fig. 9) to eliminate the influence of deformations in the load train. The effective shear modulus, $G_{c,iz}$, is calculated directly from eqn (2) with $\tau_{iz} = P/bL$, where b and L are the specimen width and length, respectively.

Figure 10 shows the three-point bend (TPB) fixture mounted in an Alwetron TCT10 universal test frame of 10 kN load capacity. The diameter of the load and support rolls was 15 mm. Beam deflection was measured by a
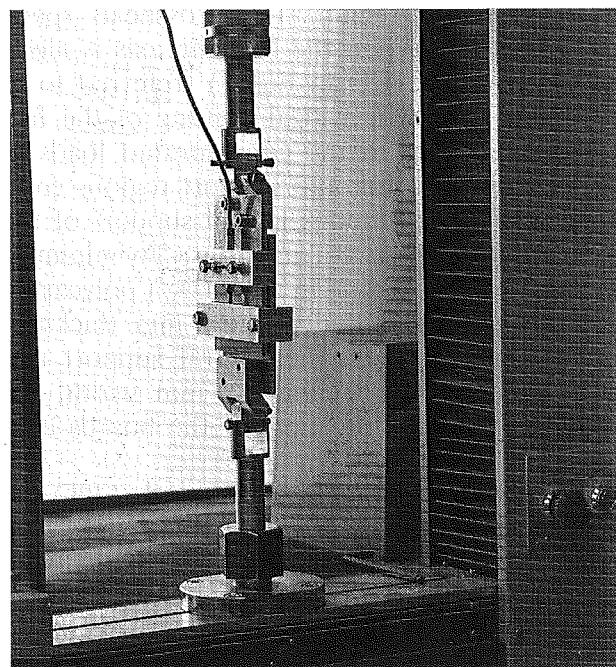
**Fig. 9.** Block shear test fixture mounted in the test frame.
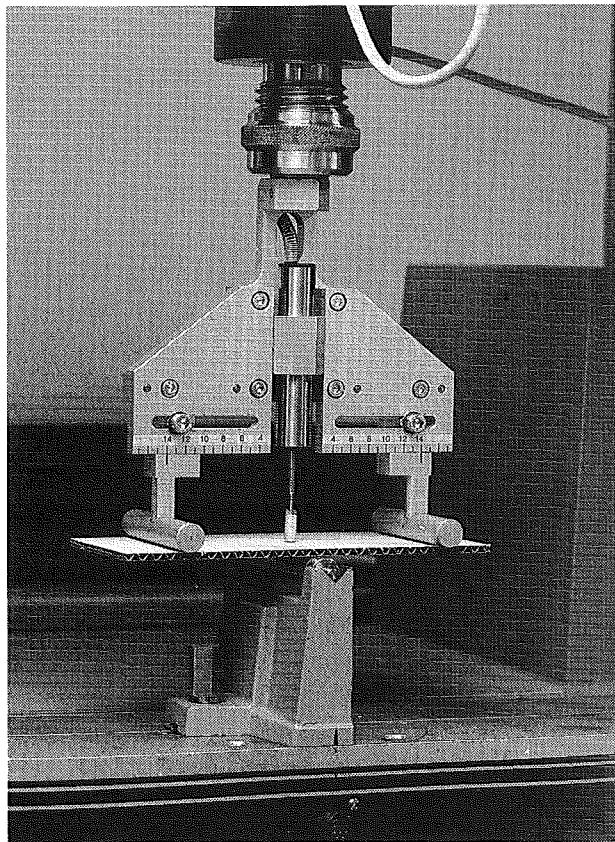
Fig. 10. Three-point bending fixture mounted in the test frame.

Fig. 11. Load–deflection curve for corrugated board 160C loaded in the CD.

linear voltage displacement transducer (LVDT) attached directly to the specimen (Fig. 10). For load measurement, a very sensitive load cell of 100 N load capacity was used. All measurements were performed within the linear (visco-) elastic response region. The crosshead speed was 3 mm/min. When the bending axis is along the corrugations (CD in Fig. 1) (referred to as 'bending in the MD') local denting of the facings is likely due to the concentrated loads in the load introduction and support regions combined with discontinuous lateral support of the facings between the corrugations. To minimize denting during bending in the MD, a polycarbonate strip of 9 mm width and 1 mm thickness was inserted between the central support and lower facing. By selecting a 9 mm width, the strip covered two flute tips for the boards considered.

Three-point bending tests of boards 140C and 160C were performed using 8 cm wide and 20 cm long specimens. Ten specimens were tested using span lengths of 10, 12, 14 and 16 cm. All tests were performed in an environmentally controlled laboratory at $23 \pm 1°C$ and $50 \pm 2\%$ RH (relative humidity).

RESULTS AND DISCUSSION

Experimental results

Figure 11 shows a typical load–displacement curve (W–Δ) for a 160C specimen with the CD along the beam axis. After the initial stiffening, the W response is highly linear. The compliance, Δ/W, was evaluated by a linear regression fit to the linear part of the W–Δ curve.

Figure 12 shows examples of plots of beam compliance from which bending and shear rigidities can be determined, see Fig. 5. Evaluation of bending and shear rigidities according to Fig. 5, using the data in Fig. 12, yields: $D_y = 4.50$ Nm, $G_{c,yz} = 13.4$ MPa (left) and $D_y = 4.49$ Nm, $G_{c,yz} = 13.4$ MPa (right). Plots similar to Fig. 12 were constructed for all board specimens, and bending stiffness and shear moduli were reduced from the slopes, see Table 3. The core material for both boards tested is the same (Table 1) which is reflected in the consistent values of effective shear moduli observed in Table 3. The bending stiffness, on the other hand, is dominated by Young's moduli and the thickness of the facings (Tables 1 and 2), which explains the larger values for board 160C.

Block shear testing was performed on boards 140B, 140C, 160C, 530C and 210BC. Inspection of the bonds between the facing and test fixture platens was performed after each test. Debonding occurred occasionally for some specimens with high shear stiffness (CD aligned with the load axis). For the more compliant MD specimens, debonding was never a problem. Only specimens with good bonding were accepted for the subsequent evaluation of shear moduli. At
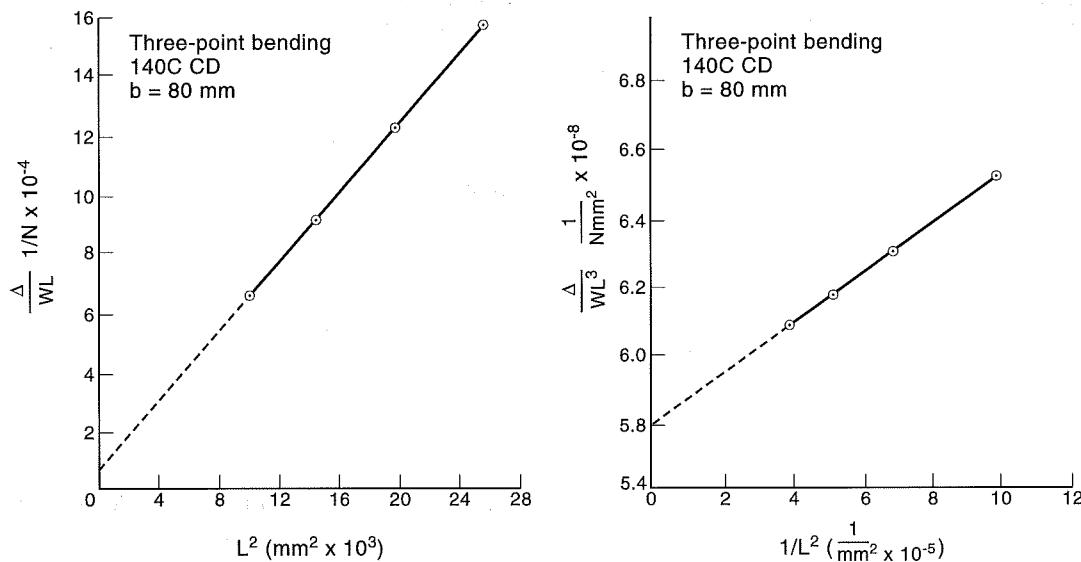
Fig. 12. Plots to determine the bending stiffness and effective transverse shear modulus for board 140C loaded in the CD.

least 10 acceptable load–displacement curves were collected for each board and loading direction. Figure 13 shows representative load–displacement curves for boards 140C and 160C. The load–displacement response is initially linear, followed by a non-linear response and a maximum in load corresponding to shear collapse of the core. The corrugated board is much stiffer in CD than in MD as evidenced from the difference in load scales for the two directions shown in Fig. 13.

An effective shear modulus was determined from a linear least-squares fit to the initial region of the load–displacement curve and eqn (2). Table 4 summarizes effective shear moduli for the boards investigated. It is observed that the shear moduli are quite consistent for the C-flute boards. The scatter in shear modulus is substantial which reflects variable material properties and processing conditions during board manufacture. The double-wall board, 210BC, has similar shear moduli as the C-flute boards, while the B-flute board has a much

larger shear modulus $G_{c,xz}$ which is evidently due to its lower flute height/corrugation pitch ratio, $C/p = 0.82$, whereas $C/p = 1.04$ for the C-flute, see Table 1. Comparison with the shear moduli for boards 140C and 160C determined from the three-point bend (TPB) test (Table 3) shows that the TPB shear moduli are about a factor of 2 less. This is evidently a result of the fact that facing deformations are unrestricted in the TPB test (see Fig. 14), while the facings are
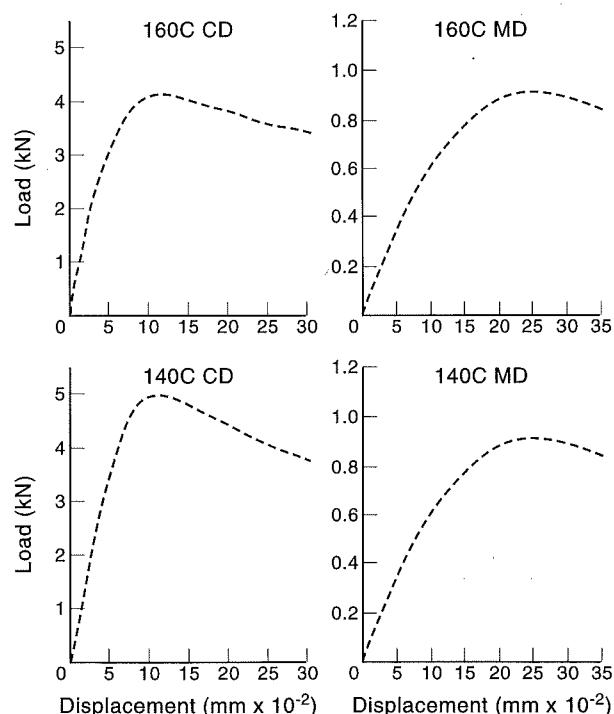
Table 3. Bending stiffnesses and effective shear moduli measured in the three-point bend test

Board	Direction[1]	D_i (Nm)	$G_{c,iz}$ (MPa)
140C	MD	11.8 ± 0.5[2]	1.80 ± 0.3
140C	CD	4.30 ± 0.2	11.6 ± 3.2
160C	MD	14.1 ± 2.5	1.60 ± 0.2
160C	CD	5.40 ± 0.1	11.2 ± 2.7

[1]MD and CD denote the machine- and cross-directions, respectively.
[2]The $\pm$ range refers to the standard deviation calculated for 10 specimens.

Fig. 13. Typical block shear load–displacement curves for boards 140C and 160C in the MD and CD, respectively.

Table 4. Transverse shear moduli for corrugated board determined from the block shear test

| Board	Direction[1]	$G_{c,iz}$ (MPa)
140B	MD	11.6 ± 3.1
140B	CD	27.0 ± 6.1
140C	MD	3.3 ± 1.2
140C	CD	31.5 ± 6.2
160C	MD	2.8 ± 0.4
160C	CD	25.5 ± 2.8
530C	MD	3.0 ± 0.6
530C	CD	17.4 ± 6.0
210BC	MD	2.8 ± 0.3
210BC	CD	20.5 ± 4.6

[1]MD and CD denote the machine- and cross-directions, respectively.

Table 6. Calculated and measured values of the transverse shear moduli obtained from the block shear test

Board	Direction[1]	$G_{iz,\text{calc}}$ (MPa)	$G_{iz,\text{exp}}$ (Mpa)
140B	MD	54.5	11.6 ± 3.1
140B	CD	54.7	27.0 ± 6.1
140C	MD	29.2	3.3 ± 1.2
140C	CD	54.7	31.5 ± 6.2
160C	MD	29.9	2.8 ± 0.4
160C	CD	42.3	25.5 ± 2.8
530C	MD	55.0	3.0 ± 0.6
530C	CD	60.8	17.4 ± 6.0
210BC	MD	40.9	2.8 ± 0.3
210BC	CD	48.8	20.5 ± 4.6

[1]MD and CD denote the machine- and cross-directions, respectively.

highly constrained by the loading platens in the block shear test.

Comparison with analytical and numerical predictions

In this section the experimental bending and shear rigidities will be compared with the corresponding analytical and numerical (FEA) values calculated based on elastic moduli, thickness of the constituents listed in Table 2 and the geometry of the cores. The bending stiffnesses were
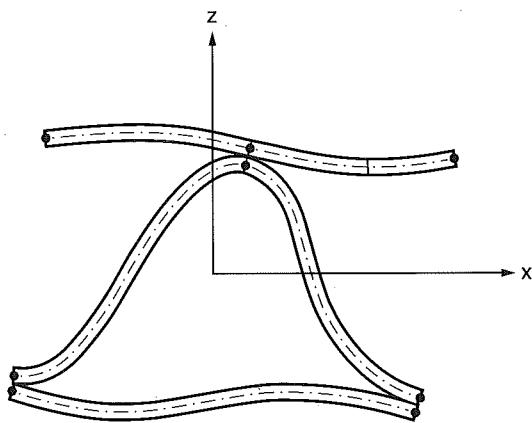
Fig. 14. Deformation of corrugated board when shear loaded in the MD.

calculated based on a procedure outlined by Carlsson et al. [1] and from compliance plots (Fig. 5) of the finite-element analysis results from the three-point bend test simulation. Experimental and calculated bending stiffnesses for boards 140C and 160C are listed in Table 5. As observed in Table 5, the measured bending stiffnesses are overall in very good agreement with the calculated ones.

For comparison between transverse shear moduli measured with the block shear test, calculations using analysis formulated and based on curved beam theory [2] was used. The calculated and block shear values of the transverse shear moduli are shown in Table 6. In all cases the calculated moduli are much larger than the measured ones. The discrepancy between calculated and measured values is much larger in MD than in CD. This is attributed to the softening influence of delaminations in regions close to the flute tips caused by large bending and shear deformations during flute formation [4]. There is also the possibility of the core buckling when the sandwich is loaded in shear which is not accounted for in the theoretical analysis [2]. This would further reduce the transverse shear stiffnesses of the board.

Table 7 lists numerically calculated and measured transverse shear moduli. Finite-element

Table 5. Calculated and measured bending stiffnesses

Board	Direction[1]	$D_{i,\text{anal}}$ (Nm)	$D_{i,\text{FE}}$ (Nm)	$D_{i,\text{exp}}$ (Nm)
140C	MD	11.9	12.1	11.8 ± 0.5
140C	CD	3.89	4.45	4.3 ± 0.2
160C	MD	14.6	15.1	14.1 ± 2.5
160C	CD	5.43	6.3	5.4 ± 0.1

[1]MD and CD denote the machine- and cross-directions, respectively.

Table 7. Finite-element calculated and measured values of (three-point bend) transverse shear moduli

Board	Direction[1]	$G_{iz,\text{FE}}$ (MPa)	$G_{iz,\text{exp}}$ (MPa)
140C	MD	6.96	1.8 ± 0.3
140C	CD	29.4	11.6 ± 3.2
160C	MD	5.43	1.6 ± 0.2
160C	CD	21.8	11.23 ± 2.7

[1]MD and CD denote the machine- and cross-directions, respectively.

simulation of the three-point bend test provides shear moduli that are much less than the corresponding analytically derived block shear moduli listed in Table 6. It was demonstrated by Nordstrand *et al.* [2] that analytical predictions of the block shear moduli were in good agreement with finite-element simulations of the block shear test. The difference between three-point bend and block shear moduli is attributed to deformable facings in the three-point bend test. Thus, deformable facings reduce the effective transverse shear modulus, but cannot explain the difference between the numerical and experimental TPB values. This discrepancy is attributed to delamination damage of the core inflicted during the corrugation process as discussed earlier.

CONCLUSIONS

Effective transverse shear moduli of corrugated board were measured using the three-point bend (TPB) and block shear tests. The transverse shear moduli obtained from TPB tests were about a factor of 2 less than those obtained by the block shear test. This discrepancy is attributed to overall deformation of the facings and local denting at the supports in the TPB. It is believed that the TPB test gives more realistic results. A similar discrepancy is obtained between the analytical solution with rigid facings and the numerical solution of the TPB test. Experimentally the block shear test and TPB test produced values of the transverse shear stiffnesses that were significantly lower than calculated values. The explanation is that the theoretical predictions are based on material properties measured before corrugation and that the flute stiffness is greatly reduced due to damage inflicted during the corrugation process.

REFERENCES

1. Carlsson, L., Fellers, C. and Jonsson, P., Bending stiffness of corrugated board with special reference to unsymmetrical and multi-wall constructions. (In German.) *Das Papier* 1985, **39**, (4), 149–156.
2. Nordstrand, T.N., Allen, H.G. and Carlsson, L.A., Transverse shear stiffnesses of structural core sandwich. *Composite Struct.* 1994, **27**, 317–329.
3. McKinlay, P. R. Machine direction shear stiffness of corrugated board a new test to determine corrugated board quality. Paper presented at the Paper Physics Seminar, 8–11 June, Dipoli Conference Center, Otaniemi, Finland, 1992.
4. Whitsitt, W.J. and Sprague, C.H., Compressive strength retention during fluting of medium. Part I: Strength losses in fluting. *TAPPI J.* 1987, **70**, (2), 91–96.
5. *ANSYS User's Manual*, Vols 1 and 2. Swanson Analysis System Inc., 1989.
6. ASTM C273-61, *Shear Test in Flatwise Plane of Flat Sandwich Constructions or Sandwich Cores*. American Society for Testing and Materials (ASTM), 1991.
7. Allen, H. G., *Analysis and Design of Structural Sandwich Panels*. Pergamon Press, Oxford, 1969.
8. Allen, H. G. and Shenoi, R. A., Flexural fatigue tests on sandwich structures. Paper presented at the 2nd International Conference on Sandwich Construction, 9–12 March, University of Florida, Gainesville, Florida, 1992.
9. Thomsen, O.T., Theoretical and experimental investigation of local bending effects in sandwich plates. *Composite Struct.* 1995, **30**, 85–101.
10. Ahmad, S., Irons, B.M. and Zienkiewicz, O.C., Analysis of thick and thin shell structures by curved finite elements. *Int. J. Numer. Meth. Engng* 1970, **2**, 419–451.
11. Baum, G.A., Brennan, D.C. and Haberger, C.C., Orthotropic elastic constants of paper. *TAPPI J.* 1981, **64**, (8), 97–101.
12. SCAN-P 7:75, *Paper and Board—Thickness and Apparent Density*. Scandinavian Pulp, Paper and Board Testing Committee, 1975.
13. SCAN-P 16:76, *Paper and Board—Tensile Strength and Stretch*. Scandinavian Pulp, Paper and Board Testing Committee, 1975.

Paper 3

———

On Buckling Loads for Edge-Loaded Orthotropic Plates including Transverse Shear

by

T. Nordstrand

To be submitted to Composite Structures.

On Buckling Loads for Edge-Loaded Orthotropic Plates including Transverse Shear

Tomas Nordstrand

SCA Research, Box 716, 851 21 Sundsvall, Sweden

ABSTRACT

Corrugated board usually exhibits low transverse shear stiffness, especially across the corrugations. In the present study the transverse shear is included in an analysis to predict the critical buckling load of an edge-loaded orthotropic linear elastic sandwich plate with all edges simply supported. In the analysis, effective (homogenised) properties of the corrugated core are used. Classical elastic buckling theory of orthotropic sandwich plates predicts that such plates have a finite buckling coefficient when the aspect ratio, i.e. the ratio between the height and width of the plate, becomes small. However, inclusion in the governing equilibrium equations of the additional moments, produced by the membrane stresses in the plate at large transverse shear deformations, gives a buckling coefficient which approaches infinity when the aspect ratio goes to zero. This improvement was first included in the buckling theory of helical springs by Harinx (1942) and later applied to orthotropic plates by Burt and Chang (1972). Some inconsistencies in the latter analysis have been considered. The critical buckling load calculated with corrected analysis is compared with a predicted load obtained using finite element analysis of a corrugated board panel, and also with the critical buckling load obtained from panel compression tests.

INTRODUCTION

Corrugated board usually exhibits low transverse shear stiffness, especially across corrugations[1, 2]. This will reduce the critical buckling load according to classical theory of orthotropic sandwich panels [3, 4]. In this small-deflection theory it is customary to assume that the membrane forces are unchanged during plate deflection and equal to their initial values. However, due to the large transverse shear strains, the change in direction of the membrane forces over a small plate element can not be disregarded. This gives additional moments that are introduced in the governing moment equilibrium equations of the panel. Such additional moments were first included in the buckling theory of helical springs by Harinx [5]. Later this was applied to shear deformable plates by Bert and Chang [6] although their work contains some inconsistencies that are corrected herein. Furthermore, in the corrected analysis the expression for the buckling coefficient is shown to reduce to the classical formulation of an orthotropic plate without shear deformation when the transverse shear stiffnesses become large. It is also shown that the buckling coefficient goes to infinity when the height-width ratio of the plate is decreased towards zero. In the following analysis the corrugated board panel is regarded as a laminated shear deformable orthotropic linear elastic plate[7]. Thus, effective (homogenised) properties of the corrugated core are used [8, 9]. The papers in the facings are also regarded as orthotropic linear elastic materials [10,11]. The analysis was used to confirm predicted critical buckling load from a finite element analysis of a corrugated board panel modelled with eight-node multi-layered isoparametric shell elements [12-14]. Predicted critical buckling load is also compared to buckling loads obtained from compression tests of corrugated board panels [15].

ANALYSIS

Figure 1 shows an element of a corrugated board panel of thickness h. Core height is h_c and wavelength of corrugations is λ_M. Facing thickness is t_f and thickness of core sheet is t_c. The principal axes of elastic symmetry of the face sheets and the core are aligned with the Cartesian coordinate system xyz. The 2-axes of the corrugated medium is parallel with the y-axes.
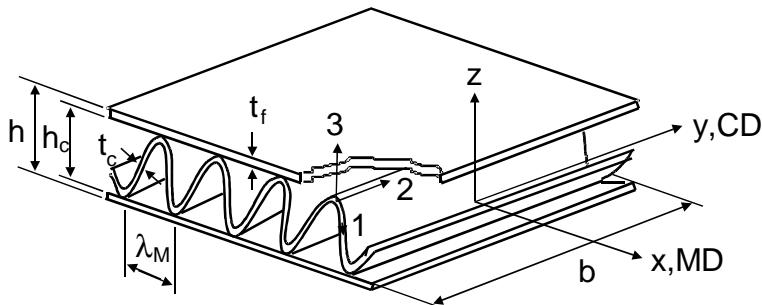
Figure 1. Schematic diagram of corrugated board.

It is assumed that the facings and core sheet are thin compared to the total thickness of the panel and that the transverse shear strains are uniform in the core layer.

Furthermore, the deflections and slopes are assumed to be small compared to the thickness of the plate. Transverse shear deformation of the plate is accommodated by assuming that cross-sections remains straight but not necessarily normal to the mid-plane of the plate during bending [6].

The membrane forces N_x, N_y, N_{xy}, transverse shear forces Q_{xz}, Q_{yz}, bending and twisting moments M_x, M_y, M_{xy} are acting on respective four sides of a plate element, see Figure 2.

The transverse shear strains, see Fig. 3, are determined by [4]

$$\gamma_{xz} = A_{55} Q_{xz}$$
$$\gamma_{yz} = A_{44} Q_{yz}$$

(1)

where A44 and A55 are the transverse shear stiffnesses [1, 2].
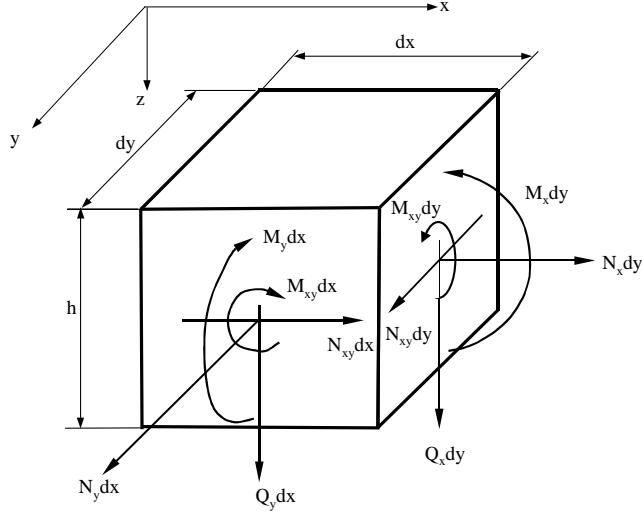
Figure 2.   Forces and moments acting on a plate element hdydx.

The plate displacement w is then related to the applied moments as follows [4]

$$M_x = -D_{11} \frac{\partial \beta_x}{\partial x} - D_{12} \frac{\partial \beta_y}{\partial y}$$

$$M_y = -D_{12} \frac{\partial \beta_x}{\partial x} - D_{22} \frac{\partial \beta_y}{\partial y}$$

(2)

where

$$M_{xy} = -\frac{1}{2} D_{66} \left(\frac{\partial \beta_x}{\partial y} + \frac{\partial \beta_y}{\partial x} \right)$$

$$\beta_x = \frac{\partial w}{\partial x} - \gamma_{xz} , \qquad \beta_y = \frac{\partial w}{\partial y} - \gamma_{yz}$$

(3)

and D_{11}, D_{22}, D_{12} and D_{66} are the bending and twisting stiffnesses defined according to ref. [7-11].

3

Figure 3 shows a cross-sectional view of the deformed plate element in the x-z-plane. Considering that the plate is loaded in compression, the normal forces N_x, N_y and the shear force N_{xy} are much larger than the transverse shear forces Q_{yz} and Q_{xz} and have to be accounted for in the lateral equilibrium of the differential plate element. Subsequently, after algebraic manipulation the equation of equilibrium in the z-direction is obtained as,

$$\frac{\partial Q_{xz}}{\partial x} + \frac{\partial Q_{yz}}{\partial y} + N_x \frac{\partial \beta_x}{\partial x} + N_y \frac{\partial \beta_y}{\partial y} + 2N_{xy}\left(\frac{\partial \beta_x}{\partial y} + \frac{\partial \beta_y}{\partial x}\right) = 0 \tag{4}$$
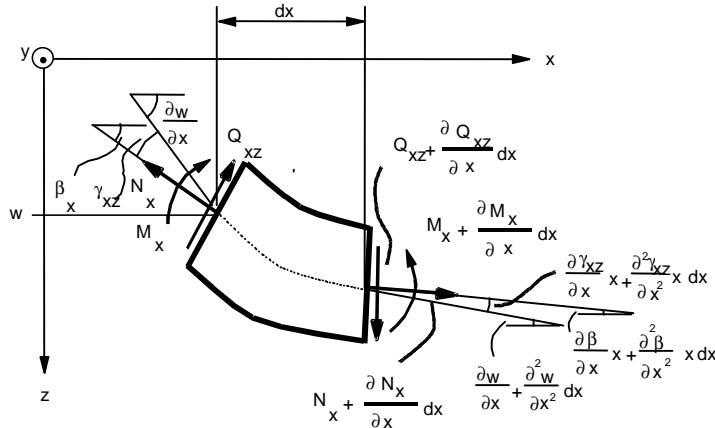
Figure 3.   Cross-section of a differential plate element.

The transverse shear strains at the left and right cross-sections in Figure 3 reduce the slope slightly more of the right cross-section than the left cross-sections. This will rotate the normal forces so that their action will not be through the centre of the differential plate element. Consequently, the normal forces will generate additional moments. These moments are taken into account in the present theory. This is the basic difference between the present theory and the classical sandwich theory [4]. The derivation of moment equilibrium around an axis through the centre of the differential element and parallel with the y-axes in Fig. 3 is then as follows.

$$\left(M_x + \frac{\partial M_x}{\partial x}dx\right)dy - M_x dy + M_{yx}dx - \left(M_{yx} + \frac{\partial M_{yx}}{\partial y}dy\right)dx$$

$$-\left(Q_{xz} + \frac{\partial Q_{xz}}{\partial x}dx\right)dydx + \left(N_x + \frac{\partial N_x}{\partial x}dx\right)dydx\left(\gamma_{xz} + \frac{\partial \gamma_{xz}}{\partial x}dx\right) = 0 \tag{5}$$

If both sides in eq. (5) are divided by dxdy and letting dx $\rightarrow$ 0 and dy $\rightarrow$ 0, eq. (5) reduces to

$$\frac{\partial M_x}{\partial x} - \frac{\partial M_{xy}}{\partial y} - Q_{xz} + N_x \gamma_{xz} = 0 \tag{6a}$$

Similarly, moment equilibrium around an axis through the centre of the differential element parallel with the x-axis yields

$$\frac{\partial M_y}{\partial y} - \frac{\partial M_{yx}}{\partial x} - Q_{yz} + N_y \gamma_{yz} = 0 \tag{6b}$$

Substitution of eqs. (1)-(3) in equilibrium eqs. (4) and (6) forms a system of three simultaneous differential equations in terms of the out-of-plane displacement w and the transverse shear strains γ_{xz} and γ_{yz}.

It is assumed that the plate is simply supported along its edges, i.e. the edges of the panel are prevented from moving out-of-plane and are not rotationally restrained. The edges are also free to move in-plane and transverse shear strains are prevented by edge stiffeners. The edges of the panel, parallel to the x-axis, are compressed uniformly by a load of intensity, p_y, per unit length, see Fig. 4.
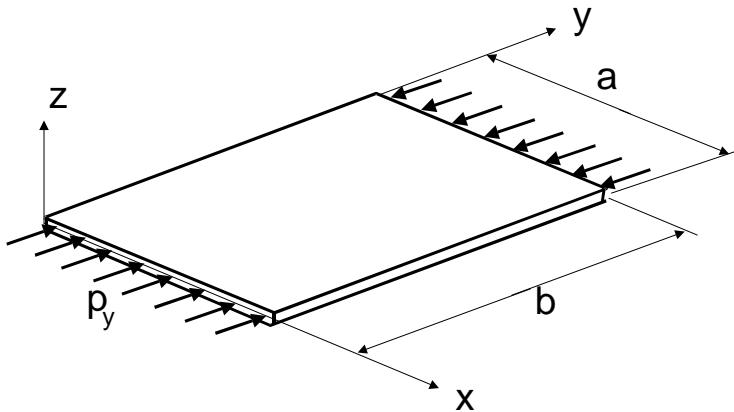
Figure 4. Schematic diagram of a simply supported panel in edgewise compression.

Thus, boundary conditions at y=0 and y=b are

$$w = 0 \qquad M_y = 0 \qquad M_{xy} = 0 \qquad \gamma_{xz} = 0$$

and boundary conditions at x = 0 and x = a are

$$w = 0 \qquad M_x = 0 \qquad M_{xy} = 0 \qquad \gamma_{yz} = 0$$

According to Navier´s procedure [7], a solution of the three simultaneous differential equations that satisfy the boundary conditions above can be obtained by assuming that the out-of-plane displacement, w, and transverse shear strains γ_{xz}, γ_{yz} can be represented by double trigonometric series. However, in the present analysis only one-term solutions are used for w, γ_{xz} and γ_{yz}, respectively.

$$w = W \sin(Ax)\sin(By) \tag{7a}$$

$$\gamma_{xz} = \Gamma_{xz} \cos(Ax)\sin(By) \tag{7b}$$

$$\gamma_{yz} = \Gamma_{yz}\sin(Ax)\cos(By) \tag{7c}$$

where W, Γ_{xz} and Γ_{yz} are corresponding amplitudes. A and B are

$$A = \frac{m\pi}{a}, \quad B = \frac{n\pi}{b} \tag{8}$$

Integers m and n are number of buckles, i.e. m and n half sine waves, in the x and y directions. In the subsequent analysis it is convenient to define a number of parameters of the homogenised sandwich plate [4]:

$$\lambda = \left(\frac{na}{mb}\right)^2, \quad \zeta = \sqrt{\frac{D_{11}}{D_{22}}}, \quad \psi = \frac{D_{66}}{\sqrt{D_{11}D_{22}}}, \quad \eta = \frac{D_{12} + 2D_{66}}{\sqrt{D_{11}D_{22}}}, \quad s_{xz} = \frac{A_{55}k}{p_y}, \quad s_{yz} = \frac{A_{44}k}{p_y}$$

where

$$k = \left(\frac{a}{n\pi}\right)^2 \frac{p_{y,crit}}{\sqrt{D_{11}D_{22}}}, \quad P_{crit,theor} = a\, p_{y,crit} \tag{9}$$

$p_{y,crit}$, is the critical load intensity (load/unit length) to cause panel buckling. The total critical buckling load is $P_{crit,theor}$.

Substitution of the trigonometric expressions eq. (7) in the differential equations (4), (6a) and (6b) leads to the following system of equations shown in matrix form

$$\begin{bmatrix} k & -\dfrac{1}{A}\left(k + s_{yz}\right) & -\dfrac{\lambda}{B}s_{xz} \\[2mm] \dfrac{1}{\zeta} + \lambda\eta & -\dfrac{1}{A}\left(\dfrac{1}{\lambda\zeta} + \psi + k + s_{yz}\right) & -\dfrac{\lambda}{B}(\eta - \psi) \\[2mm] \lambda\zeta + \eta & -\dfrac{1}{A}(\eta - \psi) & -\dfrac{\lambda}{B}\left(\zeta + \dfrac{\psi}{\lambda} + s_{xz}\right) \end{bmatrix} \begin{bmatrix} W \\[2mm] \Gamma_{xz} \\[2mm] \Gamma_{yz} \end{bmatrix} = \begin{bmatrix} 0 \\[2mm] 0 \\[2mm] 0 \end{bmatrix} \tag{10}$$

Correct expressions of the elements in the stiffness matrix of eq. (10) are given instead of those in the stiffness formulation [6]. Solution of eqs. (10) different than the trivial one, $W = \Gamma_{xz} = \Gamma_{yz} = 0$ are possible when the determinant of the matrix vanishes. This criterion leads to a second order equation of k

$$Pk^2 + Qk + R = 0 \tag{11}$$

where

$$P = \zeta + \frac{\psi}{\lambda} + s_{xz} \tag{12a}$$

$$Q = \left(s_{yz} + \psi - \lambda\zeta - 2\eta\right)P + \frac{(\lambda\zeta + \eta)^2 - (\eta - \psi)^2}{\lambda} \tag{12b}$$

$$R = \left(\zeta + \frac{\psi}{\lambda}\right)\Theta + s_{yz}\frac{(\lambda\zeta + \eta)^2}{\lambda} - P\Theta - s_{yz}P\left(\lambda\zeta + 2\eta + \frac{1}{\lambda\zeta}\right) \tag{12c}$$

and

$$\Theta = 1 + \psi\left(\lambda\zeta + 2\eta + \frac{1}{\lambda\zeta}\right) - \eta^2 \tag{12d}$$

The non-trivial solution of eq. (8) can thus be found when

$$k = -\frac{Q}{2P} \pm \sqrt{\frac{Q^2}{4P^2} - \frac{R}{P}} \tag{13}$$

where only positive values of k are valid since the buckling load must be compressive. The critical buckling load, $P_{crit,theor}$, is given by eq.(9), where n=1 and k is the smallest positive value given by eq. (11). Using eq. (12), the two ratios in eq. (13) are:

$$\frac{Q}{2P} = \frac{s_{yz}}{2}\left[1 + \frac{\psi - \lambda\zeta - 2\eta}{s_{yz}} + \frac{(\lambda\zeta + \eta)^2 - (\eta - \psi)^2}{s_{xz}s_{yz}\lambda\left(1 + \frac{\zeta + \frac{\psi}{\lambda}}{s_{xz}}\right)}\right] \tag{14a}$$

$$\frac{R}{P} = -s_{yz}\left[\left(\lambda\zeta + 2\eta + \frac{1}{\lambda\zeta}\right) + \frac{(\lambda\zeta + \eta)^2}{s_{xz}\lambda\left(1 + \frac{\zeta + \frac{\psi}{\lambda}}{s_{xz}}\right)} + \frac{1 + \psi\left(\lambda\zeta + 2\eta + \frac{1}{\lambda\zeta}\right) - \eta^2}{s_{yz}\left(1 + \frac{\zeta + \frac{\psi}{\lambda}}{s_{xz}}\right)}\right] \tag{14b}$$

Attention is now turned to analysis of the limit case of infinite large transverse shear stiffnesses in order to show that the buckling coefficient k, determined by eq. (13), for that limit is reduced to the buckling coefficient for orthotropic plates without shear deformation [7].

If the transverse shear stiffnesses A_{44} and A_{55}, corresponding to s_{yz} and s_{xz}, approach infinity then it is evident from eqs. (14) that

$$\frac{Q}{2P} \to \frac{s_{yz}}{2} \tag{15a}$$

and

$$\frac{R}{P} \to -s_{yz}\left(\lambda\zeta + 2\eta + \frac{1}{\lambda\zeta}\right) \tag{15b}$$

Substitution of eqs. (15) into eq. (13) gives

$$k = -\frac{s_{yz}}{2}\left(1 - \sqrt{1 + \frac{4\left(\lambda\zeta + 2\eta + \frac{1}{\lambda\zeta}\right)}{s_{yz}}}\right) \tag{16}$$

The square root in eq. (16) can be expanded according to the binomial series

$$\sqrt{1+\chi} = 1 + \frac{1}{2}\chi - \frac{1}{4}\chi^2 + \ldots \tag{17}$$

where

$$\chi = \frac{4\left(\lambda\zeta + 2\eta + \frac{1}{\lambda\zeta}\right)}{s_{yz}} \tag{18}$$

If eq. (17) and eq. (18) is substituted into eq. (16), the expression on the right hand side is reduced to the buckling coefficient for an orthotropic plate [4]

$$k = \lambda\zeta + 2\eta + \frac{1}{\lambda\zeta} \tag{19}$$

when s_{yz} goes to infinity.
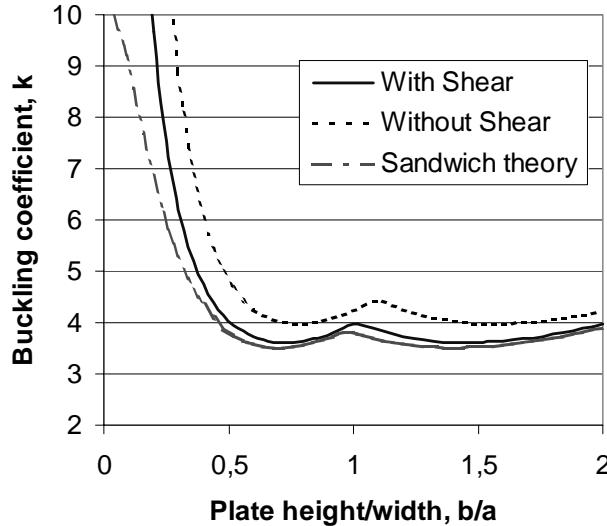
Figure 5.   Buckling coefficient k, according to present theory, eq.(13)-(14), the theory for orthotropic plate without shear [4] and the classical sandwich theory [4].

In Figure 5 the buckling coefficient for a plate with and without transverse shear is plotted versus the plate width/height ratio. The material data used is typical for a common corrugated board grade and defined in Table 2. Notice that the buckling coefficient of the plate including transverse shear has no limit when the plate height/width becomes small as classical sandwich buckling theory predicts [3,4].

COMPARISON WITH FINITE ELEMENT ANALYSIS OF A CORRUGATED BOARD PANEL

In a finite element analysis of a simply supported corrugated board panel, with side lengths a = b = 400 mm, following eigenvalue analysis was made to obtain the critical buckling load [12]. A multi-ply eight node isoparametric shell element where first order transverse shear deformation is accounted for is used in the analysis. A quarter of the panel was modelled, due to symmetry, in a 6x6 element mesh. The side length ratio between the corner element and mid element was 1:5. The finite element eigenvalue analysis is

$$([K] + \chi[S]_{ref})\{\psi\} = \{0\} \tag{20}$$

where [K] is the global stiffness matrix of the finite element model, $[S]_{ref}$ is the "stress stiffness matrix", χ is the factor used to multiply the loads which generate the stresses and $\{\psi\}$ is the generalised displacement vector of the nodes [13]. The load

$\{P\}$ is also scaled by χ and it alters the intensity of the membrane stresses but not the distribution of the stresses such that

$$\{P\} = \chi \{P\}_{ref} \Leftrightarrow [S] = \chi [S]_{ref} \tag{21}$$

As χ is increased, the overall stiffness of the plate, $([K] + [S])$, is reduced until a critical load $\{P\}_{cr}$ corresponding to the eigenvalue χ_{cr} is reached and the plate becomes unstable, i.e. $\det([K] + [S])$ goes to zero.

The corrugated board analysed has 0.23 mm thick liners and a corrugated medium with wall thickness 0.25 mm and wavelength 7.26 mm. The height of the core layer is $h_c = 3.65$ mm, see Fig. 1. Using the material data in Table 1, the buckling load of the corrugated board panel was calculated to $P_{cr,fem} = 849$ N. This value is in excellent agreement with the value obtained by the closed form solution $P_{cr,theor} = 846$ N, see eq. (9) and eq. (13). Sandwich theory gives a critical buckling $P_{cr,sand} = 815$ N and an orthotropic plate without shear $P_{cr,ortho} = 898$ N.

Table 1.   Effective material properties of the layers in the panel.

Layer	E_x (GPa)	E_y (GPa)	E_z (GPa)
1	8.25	2.9	2.9
2	0.005	0.231	3.0
3	8.18	3.12	3.12
Layer	G_{xy} (GPa)	G_{xz} (GPa)	G_{yz} (GPa)
1	1.89	0.007	0.070
2	0.005	0.0035	0.035
3	1.95	0.007	0.070
Layer	ν_{xy}	ν_{xz} +	ν_{yz} +
1	0.43	0.01	0.01
2	0.05	0.01	0.01
3	0.43	0.01	0.01

+ The Poisson's ratios are assumed small because of the plane stress condition in the board.

COMPARISON WITH EXPERIMENTS

Panels size 400x400 mm were cut from corrugated board and tested under compression in a rig that furnishes simply supported boundary conditions [15]. Panels were oriented with the cross direction (CD) in the direction of loading, see Figure 6.
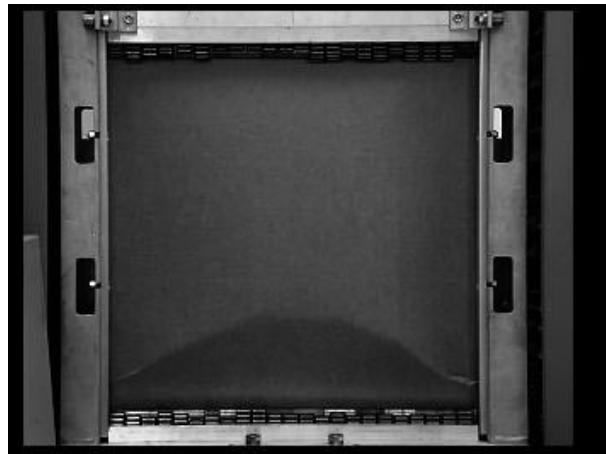
Figure 6.   Rig and corrugated board panel tested under compression.

Material data for the board is given in Table 2. The critical buckling load as estimated from the test results by means of a non-linear regression analysis method [15] was 814 N. This value is consistent with the analytically predicted critical buckling load of 870 N using the present buckling analysis, i.e. an analysis of a plate including transverse shear deformation.

Table 2.   Corrugated board data. Transverse shear stiffness is measured.

Basis weight, g/m^2		556
Thickness, mm	h	4.02
Corrugation wavelength, mm	λ_M	7.26
Bending stiffness, Nm	D_{11}	14.6
	D_{22}	5.43
	D_{12}	2.71
	D_{66}	3.34
Transverse shear stiffness, kN/m	A_{44}	39.2
	A_{55}	5.6

In comparison, a plate without shear deformation is predicted to have a critical buckling load of 924 N, which is exactly the same result as obtained from the classical theory of orthotropic plates [7].

CONCLUSIONS

An explicit equation for the buckling load of a simply supported orthotropic linear elastic plate in edgewise compression has been derived taking into account first order transverse shear deformation. There is major difference between present theory and classical sandwich theory in the additional moments that are introduced in the governing moment equilibrium equations of the panel, due to change in directions of the membrane forces over a small plate element that has large transverse shear strains.

When the transverse shear stiffness goes to infinity the critical buckling load, predicted by the present theory, is shown to be reduced to the critical buckling load of an orthotropic plate without transverse shear deformation. Furthermore, the buckling coefficient does not have a limit in the present theory when the plate height/width becomes small, as classical sandwich buckling theory predicts. The present theory is approximate due to one-term approximations of the deflection $w(x,y)$ and the transverse shear strains $\gamma_{xz}(x,y)$ and $\gamma_{yz}(x,y)$. Verification by finite element analysis suggests that the present explicit equation for the buckling load is accurate, the deviation is typically less than 0.5%. However, the discrepancy is larger between present theoretical buckling load and the experimental buckling load of corrugated board panels. This may partly be due to the difficulties involved in evaluation of the buckling load from the experimental results [15] partly due to the non-linear material behaviour of paper.

REFERENCES

1. T. M. Nordstrand, H. G. Allen and L. A. Carlsson, "Transverse Shear Stiffness of Structural Core Sandwich", Composite Structures, Vol. 27, pp. 317-329, 1994.

2. T. Nordstrand and L.A. Carlsson, "Evaluation of Transverse Shear Stiffness of Structural Core Sandwich Plates", Composite Structures, Vol. 37, pp. 145-153, 1997.

3. E. Reissner, "The Effect of Transverse Shear Deformation on Bending of Elastic Plates", Journal of Applied Mechanics, 12, A69-A77, 1945.

4. F.J. Plantema, "Sandwich Construction", John Wiley & Sons, Inc., New York, N.Y., 1966.

5. J. A. Harinx, "On Buckling and the Lateral Rigidity of Helical Compression Springs", Proceedings of the Konjlike Nederland Akademie Wettenschappen, Vol. 45, pp. 533-539, 650-654, Amsterdam, Holland,1942.

6. C.W. Bert and S. Chang, "Shear-Flexible Orthotropic Plates Loaded In-Plane", Journal of Engineering Mechanics Division, Proceedings of the American Society of Civil Engineers, Vol. 98, No. EM6, pp. 1499-1509, December, 1972.

7. Jones, R. M., Mechanics of Composite Materials, Hemisphere Publishing Corp. New York, 1975.

8. L. A. Carlsson, T. Nordstrand and B. Westerlind, "On the Elastic Stiffnesses of Corrugated Core Sandwich", Journal of Sandwich Sturctures and Materials, Vol. 3, pp. 253-267, 2001.

9. C. Libove and R. E. Hubka, "Elastic Constants for Corrugated Core Sandwich Plates", NACA, TN 2289, 1951.

10. G. A. Baum, D. C. Brennan and C. C. Habeger, "Orthotropic Elastic Constants of Paper", Tappi, Vol. 64, pp. 97-101, 1981.

11. R. Paetow and L. Göttsching, "Poisson's Ratio of Paper", Das Papier, Vol. 6, pp. 229-237, 1990.

12. T. Nordstrand, "Parametrical Study of the Post-buckling Strength of Structural Core Sandwich Panels", Composite Structures, Vol. 30, pp. 441-451, 1995.

13. ANSYS User's Manual, Swanson Analysis System Inc., Vol. 1-2, 1989.

14. S. Ahmad, B. M. Irons and O. C. Zienkiewicz, "Analysis of Thick and Thin Shell Structures by Curved Finite Elements", International Journal of Numerical Methods in Engineering, No. 2, pp 419-451, 1970.

15. T. Nordstrand, "Analysis and Testing of Corrugated Board Panels into the Post-buckling Regime", To be submitted to Composite Structures.

Paper 4

———

Parametrical Study of the Post-buckling Strength of Structural Core Sandwich Panels

by

T. Nordstrand

0263-8223(94)00066-2

Parametric study of the post-buckling strength of structural core sandwich panels

T. M. Nordstrand

SCA Research AB, Box 3054, 850 03 Sundsvall, Sweden

Post-buckling strength of simply supported orthotropic corrugated board panels subjected to edge compressive loading has been investigated using geometrically non-linear finite element analysis (FEA). Adjustments of the transverse shear stiffnesses in the FEA were necessary and performed by comparing the critical buckling load calculated by FEA with a closed form solution. The collapse load of the sandwich plate was calculated based on material failure of the facings predicted from Tsai–Wu failure theory. Parametric studies were performed to investigate the sensitivity of the collapse load to changes in the transverse shear stiffnesses of the core, initial out-of-plane imperfections, asymmetry in board construction, slenderness ratio and eccentric loading of the plate. It was found that a reduction of the transverse shear stiffnesses of the core below a certain limit produces a significant reduction in the collapse load. Panels are said to be insensitive to imperfections and this holds true when the imperfections are the same as or lesser than the thickness of the panel, but a 40% reduction of the collapse load is observed for imperfections that are ten times the panel thickness. From a design point of view it is shown that a symmetrical board is preferred because an asymmetric board as well as eccentric loading of the panel significantly reduce the collapse load. It is also shown that the critical buckling load is directly related to the slenderness ratio of the panel whereas the collapse load is not.

1 INTRODUCTION

This paper considers a sandwich construction of considerable practical use in the packaging industry. The sandwich, referred to as corrugated board, consists of a core made from a corrugated paper sheet (fluting) attached at its troughs and crests to flat facings (liners). Typically the board is converted into a box which must sustain the weight of other boxes and packages stacked on top of the box. Often the box is designed for a specific load level with an added factor of safety. The safety factor compensates, to some extent, for the lack of knowledge about the spread in material properties of the constituents of the board, but also for reductions in the load carrying capability due to unknown factors such as initial imperfections and eccentric loading induced by the creases between the vertical panels and flaps at top and bottom. Another factor that may reduce the load carrying capability of a corrugated board panel is transverse shear deformation. Previous studies[1,2] have shown that the

approximately sine wave shaped corrugated core has low shear stiffnesses, especially in directions perpendicular to the corrugations. The slenderness ratio and asymmetry due to differences in thicknesses and elastic moduli of the facings, also affect the performance of the panel.

It is the objective of this study to examine the sensitivity of the collapse load of such sandwich panels to changes in the transverse shear stiffnesses of the core, initial out-of-plane imperfections, slenderness ratio, asymmetry in board construction and eccentric loading. Since the panels are essentially flat, i.e. the magnitude of the initial imperfection is much smaller than the thickness of the panel, the panels will buckle in a stable manner. This means that the collapse load of such a panel may exceed the calculated elastic critical buckling load and that the panels may undergo large out-of-plane displacements, i.e. deflections many times the thickness of the panel.[3-7] Thus, analysis of the collapse of such a sandwich plate under in-plane compressive load requires incorporation of geometrical non-linearities due to

large deflections. Several studies have been published on the post-buckling behaviour of isotropic and orthotropic plates.[8-13] However, as has been pointed out by Folie:[14] 'The complexity of the sandwich equations has resulted in relatively few analytical solutions being obtained. The reason for this difficulty is that the partial differential equations for sandwich plates generally do not have closed form or series solutions for all possible boundary conditions'. Thus, in order to achieve the objectives of our study, finite element analysis (FEA) as reported in Refs. 15–17 was employed. The study is limited to square panels. The ANSYS finite element code[18] was used for all computations. Numerical results are compared with an analysis for a laterally loaded orthotropic plate which does not incorporate transverse shear deformation and a buckling analysis of orthotropic plates including transverse shear deformation.

2 ANALYSIS

The element formulation is based on the standard isoparametric approach to plate problems, similar

Fig. 1. The eight-node isoparametric shell element, STIF99.

to that given by Ahmad *et al.*[16] In short, the element used, denoted STIF99 in the ANSYS finite element code,[18] has four corner nodes and four middle side nodes which are connected by quadratic shape functions which describe both the original shape and the displacements of the element, see Fig. 1. Bending and shear deformations are accounted for by the degenerated solid element approach, similar to that adopted in the Mindlin plate theory, i.e. cross-sections of the plate remain straight but not necessarily normal to the mid-plane during bending, see for example, Ref. 17.

The element features a multi-layer capability which enables modelling of sandwich structures such as corrugated board. However, since each layer is assumed to be homogeneous and orthotropic, the corrugated core has to be transformed to an equivalent homogenous core layer with 'effective' material properties, see Fig. 2.

With x, y and z being the cartesian coordinate system of the corrugated board panel and 1, 2 and 3 the curvilinear coordinate system of the corrugated core, where the y- and 2-axes are coincident and parallel to the core ridges, the 1-axis follows the curvature of the corrugated sheet and the z-axis is oriented in the thickness direction, see Fig. 3, the effective core moduli, $E_{i,j}$ (i = directions x and y, j = layer No.) can be approximated as follows:

$$E_{x,2} \approx 0 \tag{1a}$$

$$E_{y,2} = \frac{\alpha S_{2,c}}{h_c} \tag{1b}$$

where α (take-up factor) is the ratio between the arc length and the wavelength of the corrugation pitch, h_c is the core thickness and $S_{2,c}$ is the

Fig. 2. Transition of the structural core (left) to a homogeneous core (right).

tensile stiffness of the corrugated core sheet in the 2-direction, see Fig. 3. This approximation provides correct in-plane extensional moduli and bending stiffness D_x, but the bending stiffness D_y, may be incorrect. However, using the approach given by Carlsson *et al.*[19] to calculate the moment of inertia of the core cross-section, $I_{y,c}$, the error in bending stiffness can be shown to be less than 5%, see Appendix.

Libove and Hubka[20] showed that if the corrugated core is symmetrical, its contribution to the in-plane shear and twisting stiffnesses of the panel can be neglected. Consequently the effective in-plane shear modulus, $G_{xy,2}$, of the core was set to a very small value. The effective transverse shear moduli of the core $G_{xz,2}$ and $G_{yz,2}$ were calculated from measured transverse shear stiffnesses of the board.[2]

Concerning the facings, the principal axes of elastic symmetry are assumed to be aligned with the cartesian coordinate system of the corrugated board panel. Consequently, the in-plane Young's moduli, $E_{x,j}$ and $E_{y,j}$, coincide with the measured principal Young's moduli, $E_{1,j}$ and $E_{2,j}$ of the facings ($j = 1, 3$). The in-plane shear moduli $G_{xy,j}$ of the facings are difficult to measure, but have been found empirically to be aproximated by:[21]

$$G_{xy,j} = G_{12,j} \approx 0.387 \sqrt{E_{1,j} E_{2,j}} \qquad (2)$$

where $j = 1, 3$.

Loading and boundary conditions for a compressively loaded simply supported plate are shown in Fig. 4 where w denotes the lateral displacement in the z-direction. The load intensity is P_x and a and b are the length and width of the panel, respectively. All edges are constrained to deform only in the x–y plane and rotate freely. The loaded edges are assumed to displace uniformly along the x-axis, i.e. the in-plane displacement v is constant along the loaded edges. Thus:

$$x = 0, b: \begin{cases} w = 0 \\ \dfrac{\partial^2 w}{\partial x^2} = 0 \end{cases} \quad y = 0, a: \begin{cases} v = \text{const.} \\ w = 0 \\ \dfrac{\partial^2 w}{\partial x^2} = 0 \end{cases} \qquad (3)$$

For the square panel considered ($a = b$), it may be shown that the panel buckles in its first mode, i.e. in half a wavelength along the x- and y-directions respectively [22]. This is illustrated in Fig. 5 where the buckling coefficient k, defined as

$$k = \frac{b^2 P_{cr,theor}}{\pi^2 \bar{D}} \qquad (4)$$

where $\bar{D} = \sqrt{D_x D_y}$ and $P_{cr,theor}$ is the critical buckling load, is plotted versus the aspect ratio, a/b.


Fig. 3. Dimensions and coordinate systems of the corrugated board.
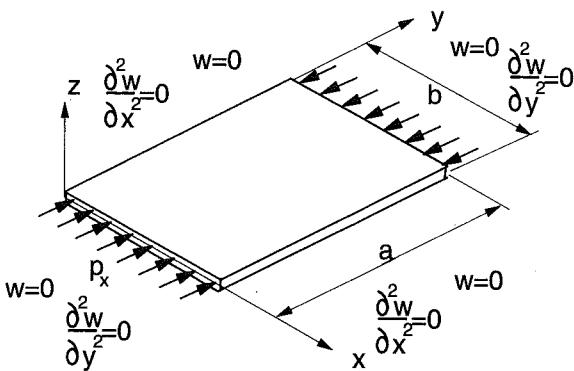
Fig. 4. Edge-wise loading of a simply supported plate where w denotes the out-of-plane deformation.
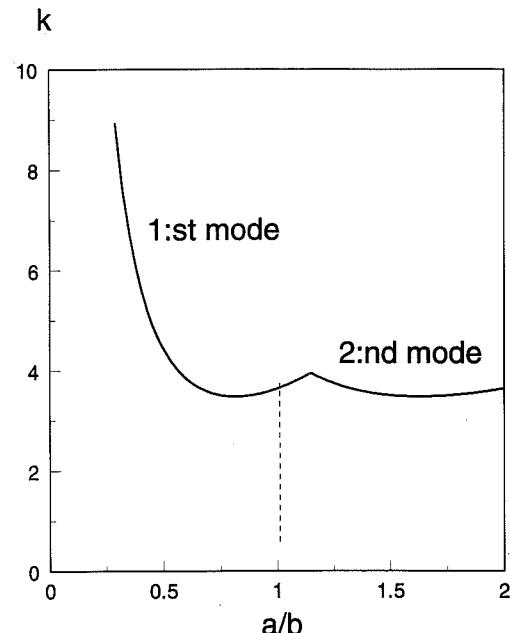

Fig. 5. The buckling coefficient of the reference panel versus the aspect ratio a/b.

The shift between the first and second mode occurs at $a/b \approx 1 \cdot 1$. Biaxial symmetry thus applies to the square panel considered which means that only a quarter of the panel needs to be modelled.

For plates where the planar dimensions are large compared to the thickness, large transverse shear stress gradients exist near the corners.[23] Consequently, accurate numerical analysis requires that the mesh be refined in that area. A 6×6 element mesh was chosen with a side ratio of $1:5$ between the corner and middle element, see Fig. 6. To check for accuracy, the model was compared with an analytical solution for a laterally pressure loaded, simply supported, homogeneous plate given by Reddy.[24] The out-of-plane displacement at the center was found to be within $0 \cdot 5\%$ of the analytical solution, which indicates that the mesh is appropriate.

In homogeneous plate analysis where the transverse shear strain and stress are assumed to be constant through the thickness it is common to reduce the transverse shear moduli by a 'shear correction factor' of $1 \cdot 2$ to compensate for the excessive amount of shear strain energy produced, as in Ref. 17. In the current finite element formulation the transverse shear moduli of each layer are reduced by a factor f given by:

$$f = 1 \cdot 2 \tag{5a}$$

or

$$f = \left\{ 1 \cdot 0 + 0 \cdot 2 \frac{A}{25 \, h^2} \right\} \tag{5b}$$

whichever is greater, where A and h are the area of the element and the thickness of the panel,

SYM
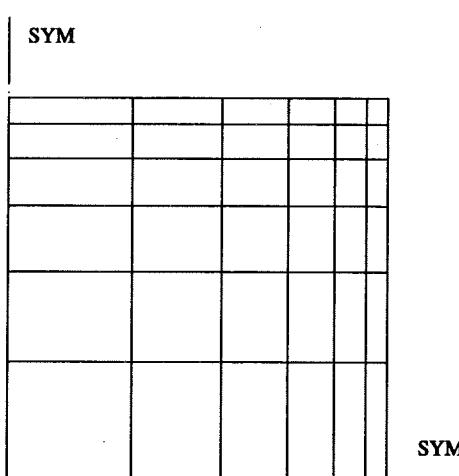
Fig. 6. Finite element mesh of the corrugated board panel. Due to loading, geometry and deflection symmetries only one quarter of the panel is considered.

respectively. Equation (5b) is included in order to prevent shear locking.[18]

Thus the transverse shear moduli of the elements are commonly modified to achieve the appropriate transverse shear stiffnesses for the panel. This is, however, only required when the bending stiffnesses of a layer are large enough to significantly contribute to the total bending stiffness of the panel. For the corrugated core sandwich panels considered, the bending stiffnesses of the core are inherently low compared with the contributions from the facings.[1,2] Thus the correction made above should not be performed for the core.[17] The transverse shear stiffnesses of the facings are considered later in this section.

The stress/strain relationship of each layer, j, can be expressed by:

$$\{\sigma\}_j = [Q]_j \{\varepsilon\}_j \tag{6}$$

where $\{\sigma\}_j$ and $\{\varepsilon\}_j$ are the stresses and strains, respectively, and the elastic stiffness matrix $[Q]_j$ is defined as:

$$[Q]_j = \frac{1}{1 - \nu_{xy,j}\nu_{yx,j}} \times$$

$$\begin{bmatrix} E_{x,j} & \nu_{xy,j}E_{y,j} & 0 & 0 & 0 \\ \nu_{yx,j}E_{y,j} & E_{y,j} & 0 & 0 & 0 \\ 0 & 0 & G_{xy,j} & 0 & 0 \\ 0 & 0 & 0 & \dfrac{G_{yz,j}}{f} & 0 \\ 0 & 0 & 0 & 0 & \dfrac{G_{xz,j}}{f} \end{bmatrix} \tag{7}$$

where $\nu_{xy,j}$ and $\nu_{yx,j}$ are the Poisson's ratios. The stiffness matrix can be integrated through the thickness h of the panel to obtain the membrane, coupling and bending stiffness matrices as follows:

$$[A] = \int_{-h/2}^{h/2} \sum_j [Q]_j \, dz \tag{8a}$$

$$[C] = \int_{-h/2}^{h/2} \sum_j z[Q]_j \, dz \tag{8b}$$

$$[D] = \int_{-h/2}^{h/2} \sum_j z^2[Q]_j \, dz \tag{8c}$$

These stiffness matrices in turn can be combined with the strain/displacement matrix [B], which connects the displacements to the strains

and curvatures of the element, to form the element stiffness matrix [k] as follows

$$[k] = \int_A ([B_0]^T[A][B_0] + [B_0]^T[C][B_1]$$

$$+ [B_1]^T[C][B_0] + [B_1]^T[D][B_1]) \, dA \qquad (9)$$

where $[B] = [B_0] + z[B_1]$, as in Ref. 17. The element stiffness matrices are subsequently assembled to a global stiffness matrix [K], which is used in an eigenvalue analysis of the finite element model to determine a suitable load step for the non-linear analysis. The following equation is solved in the eigenvalue analysis:

$$([K] + \lambda[S]_{ref})\{\psi\} = \{0\} \qquad (10)$$

where $[S]_{ref}$ is the 'stress stiffness matrix', λ is the factor used to multiply the loads which generate the stresses, and $\{\psi\}$ is the generalized displacement vector for the nodes.[18] $[S]_{ref}$ is obtained by applying consistent nodal forces $\{P\}_{ref}$, corresponding to a uniform unit pressure on the edges as indicated in Fig. 4, and performing a static linear analysis to obtain the membrane stresses which generate the matrix $[S]_{ref}$ according to Ref. 15. The load $\{P\}$ can be scaled by a factor λ which also alters the intensity of the membrane stresses but not the distribution of the stresses such that:

$$\{P\} = \lambda\{P\}_{ref} \Leftrightarrow [S] = \lambda[S]_{ref} \qquad (11)$$

As λ is increased, the overall stiffness of the plate, ([K]+[S]), is reduced until a critical load $\{P\}_{cr}$ corresponding to the eigenvalue λ_{cr} is reached and the plate becomes unstable, i.e. ([K]+[S]) goes to zero.

In the stiffness matrix [A], eq. (8a), the transverse shear stiffnesses are found by integrating the transverse shear moduli through the thickness of each layer. Since the facings are much thinner than the core, the transverse shear stiffnesses of the facings will have a minor influence on P_{cr}. This is not the case, however, when we consider the matrix elements corresponding to the transverse shear moduli in the bending stiffness matrix [D], eq. (8c), because the shear moduli of each layer are multiplied by the second moment of area of respective layer. Thus the transverse shear moduli of the facings have to be realistic in relation to the transverse shear moduli of the core to produce a correct value of P_{cr}. This was done by comparing the calculated P_{cr} with $P_{cr, theor.}$ obtained from the buckling analysis including transverse shear deformation,[22] eq. (4), and adjusting the transverse shear moduli of the facings accordingly. The

transverse shear moduli of the facings were set to twice the effective transverse shear moduli of the core by this procedure.

The panel may collapse at a load much higher than the critical buckling load P_{cr} according to Ref. 7. In this so-called post-buckled state the deflection of the panel is larger than its thickness and this introduces a geometric non-linearity between the load and displacement of the panel because approximations, like $\sin \varphi = \varphi$, made in linear analysis become inaccurate. This means that the stiffness matrix [K] of the panel becomes a function of the unknown displacements, i.e.

$$[K(\psi)]\{\psi\} = \{P\} \qquad (12)$$

where $\{\psi\}$ is a set of known and unknown nodal displacements and $\{P\}$ represents a set of external loads which act on the nodes. In order for the finite element model of the panel to exhibit out-of-plane deformation, it must contain an imperfection which in our case is introduced by a slightly curved shape of the panel. The shape of the imperfection is assumed to be described by the product of two sine functions in x- and y-directions of amplitude w_o. The non-linear problem is solved step-wise using the Newton–Raphson method.[18] The general algorithm proceeds as follows.

1. Prescribe known displacements $\{\psi^k\}_i$ of the notes on the edges parallel to the y-axis, in this case a uniform displacement. The superscript k denotes known displacements and the subscript i is the load step.

2. Compute the unknown forces $\{P\}_i$ and displacements $\{\psi^u\}_i$ using the stiffness matrix from the earlier step $[K]_{i-1}$ (for the first step, $i = 1$, the global stiffness matrix of the undeformed panel is used $[K]_0$). Then $[K]_{i-1}(\{\psi^k\}_i + \{\psi^u\}_i) = \{P\}_i$.

3. Compute the updated stiffness matrix $[K]_i$ corresponding to the configuration $\{\psi^k\}_i + \{\psi^u\}_i$.

4. Calculate restoring force $\{P^r\}_i$ and the change in displacements $\{\Delta\psi\}_i$ as $[K]_i(\{\psi^k\}_i + \{\psi^u\}_i + \{\Delta\psi\}_i) = \{P\}_i + \{P^r\}_i$.

5. Convergence is checked by Max$\{\Delta\psi\}_i \le c$, where c is an arbitrary small number for which equilibrium is approximately obtained.

6. If the solution is not converged, add $\{\Delta\psi\}_i$ to $\{\psi^u\}_i$, add $\{P^r\}_i$ to $\{P\}_i$ and repeat steps 3 to 5.

7. If the solution is converged continue with the next load step $\{\psi^k\}_{i+1} = \{\psi^k\}_i + \{\psi^u\}_i + \{\Delta\omega\}_i + \{\Delta\psi^k\}_{i+1}$.

The loading is terminated when the stress state at any point in the facings of the panel exceeds a predefined failure criterion, in this case the Tsai–Wu theory[25] which postulates that a failure surface in the stress space exists which in tensor form is written as:

$$F_i \sigma_i + F_{ij} \sigma_i \sigma_j = 1, \qquad i, j = 1, \dots, 6 \qquad (13)$$

where F_i and F_{ij} are strength tensors of the second and fourth ranks, respectively. Contracted stress notation with $\sigma_4 = \tau_{23}$, $\sigma_5 = \tau_{31}$ and $\sigma_6 = \tau_{12}$ is used. The facings are assumed orthotropic with the principal directions 1 and 2 coincident with the x- and y-axes of the corrugated board panel. It is also assumed that the facings are under plane stress, i.e. $\sigma_3 = \sigma_z = 0$, and that the transverse shear stresses are negligible, i.e. $\sigma_4 = \sigma_5 = 0$, which reduces eqn (13) to:

$$F_1 \sigma_x + F_2 \sigma_y + F_6 \tau_{xy} + F_{11} \sigma_x^2 + F_{22} \sigma_y^2 + F_{66} \tau_{xy}^2$$
$$+ 2F_{12} \sigma_x \sigma_y = 1 \qquad (14)$$

The failure criterion, eqn (14), represents a surface of an ellipsoid in the stress space spanned by σ_x, σ_y and τ_{xy}, see Fig. 7, where:

$$F_1 = \frac{1}{X_1^T} + \frac{1}{X_1^C}, \quad F_2 = \frac{1}{X_2^T} + \frac{1}{X_2^C}, \quad F_6 = 0,$$

$$F_{11} = -\frac{1}{X_1^T X_1^C}, \quad F_{22} = -\frac{1}{X_2^T X_2^C} \text{ and } F_{66} = \frac{1}{S_6^2} \qquad (15)$$

The terms X_i^T, X_i^C $(i = 1, 2,)$ and S_6 are the tensile, compressive and shear strengths respectively (notice that X_1^C and X_2^C are < 0). For paper, F_{12} and S_6 have been shown to be closely approximated by:[26]

$$F_{12} \approx -0.36 \sqrt{F_{11} F_{22}} \qquad (16)$$
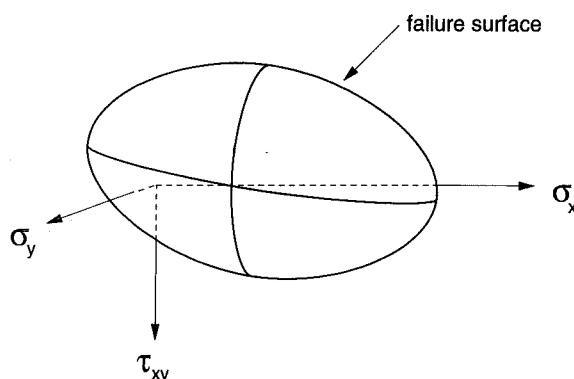
and

$$S_6 \approx \sqrt{X_1^C X_2^C} \qquad (17)$$

These approximations reduce the amount of testing of paper to only tensile and compressive strength measurements in the principal directions.

The investigation is divided into three parts. The first part deals with the sensitivity of the collapse load to initial imperfections and changes in transverse shear stiffnesses of the panel. These are accounted for by changing the imperfection amplitude w_o and the effective transverse shear moduli of the core, G_{xz} and G_{yz}. The second part focuses on how the slenderness of the panel and asymmetry of the board might influence the strength of the panel. The slenderness ratio, a/h, is changed by varying both the side length a and core thickness h_c. Asymmetry of the board is varied by changing the ratio between the tensile stiffnesses of the facings, $t_{f,1} E_{i,1} / t_{f,3} E_{i,3}$ $(i = x, y)$ where $t_{f,j}$ and $E_{i,j}$ are the thicknesses and the elastic moduli of the facings $(j = 1, 3)$. The third part deals with eccentric loading of the panel and how it reduces the collapse load. Load eccentricity is achieved by introducing nodes parallel with the x-axis at the loaded edges and at a distance e from the midplane of the panel, see Fig. 8. The loaded nodes are rigidly connected to the nodes on the edges and nodal loads are introduced corresponding to a uniform displacement.

A reference panel made from board denoted by 170C of dimensions 40×40 cm was chosen for comparison. The reason for utilizing this board is that a complete set of stiffnesses are readily available from previous measurements.[2] The board consists of 0.23 mm thick facings and a corrugated core with a wall thickness of 0.25 mm and a wavelength of 7.26 mm. The height of the core layer is $h_c = 3.65$ mm, see Fig. 3. The tensile stiffness $S_{2,c}$ of the corrugated sheet is 570 kN/m.

Fig. 7. Failure surface in the stress space spanned by the in-plane stresses, σ_x, σ_y and τ_{xy}, according to Tsai–Wu's failure criterion.
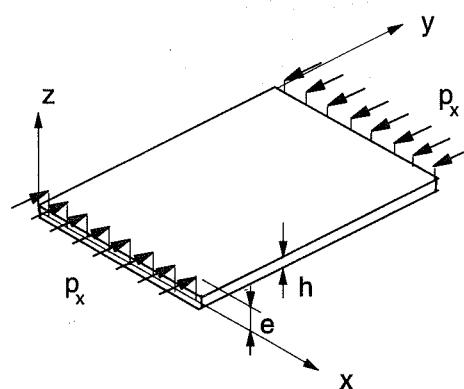

Fig. 8. Illustration of eccentric loading of the panel.

Assuming a sinusoidal core shape and a take-up factor $\alpha = 1.42$, the effective Young's modulus $E_{y,2}$ of the core was obtained according to eqn (1).

The effective Young's moduli of each layer of the panel are listed in Table 1. The Poisson's ratios in Table 1 are taken from Paetow and Gottsching[27] and the in-plane shear moduli of the facings are estimated using Baum's formula,[21] eqn (2). From Table 1 it is clear that the board chosen is not perfectly symmetrical. This means that the neutral surface in bending will not coincide with the middle plane of the board. In addition, a board with an orthotropic structural core has different neutral surfaces in x- and y-directions. However, the difference in Young's moduli of the facings are small and the coupling effects can be neglected. With the above mechanical and geometric properties the membrane, coupling and bending stiffnesses are calculated by the finite element program. Table 2 lists the stiffnesses for the element at the centre of the panel. The strength properties of the facings are listed in Table 3.

Table 1. Effective material properties of the layers in the panel

Layer No.	E_x (GPa)	E_y (GPa)	E_z (GPa)
1	8·25	2·9	2·9
2	0·005	0·231	3·0
3	8·18	3·12	3·12

Layer No.	G_{xy} (GPa)	G_{xz} (GPa)	G_{vz} (GPa)
1	1·89	0·007	0·070
2	0·005	0·0035	0·035
3	1·95	0·007	0·070

Layer No.	v_{xy}	v_{xz}^*	v_{yz}^*
1	0·34	0·01	0·01
2	0·05	0·01	0·01
3	0·34	0·01	0·01

*The Poisson's ratios are assigned small numbers because of the plane stress condition assumed for the board.

Table 2. Stiffnesses of the centre element of the reference panel

A_{ij} (kN/m)	C_{ij} (kN)	D_{ij} (Nm)
$A_{11} = 3928$	$C_{11} = 40.1$	$D_{11} = 14.780$
$A_{12} = A_{21} = 431$	$C_{12} = C_{21} = 38.4$	$D_{12} = D_{21} = 1.625$
$A_{22} = 2284$	$C_{22} = 128.8$	$D_{22} = 6.355$
$A_{44} = 97$	$C_{44} = 0.0$	$D_{44} = 0.137$
$A_{55} = 12$	$C_{55} = 0.0$	$D_{55} = 0.021$
$A_{66} = 884$	$C_{66} = 41.4$	$D_{66} = 3.350$

3 RESULTS AND DISCUSSION

Using the material data in Tables 1 and 2 the buckling load of the reference panel was calculated to $P_{cr,ref} = 849$ N according to eqn (10). This value is in excellent agreement with the value obtained by a closed form solution, eqn (4), where the coupling effects are omitted,[22] $P_{cr,theor} = 846$ N.

To evaluate the sensitivity of the buckling and collapse load to changes in the transverse shear stiffnesses of the core, the transverse shear moduli of the core were varied over wide ranges. It should be pointed out that G_{xz} is generally much less than G_{yz} according to Refs. 1 and 2. The amplitude, w_o, of the initial imperfection was set to 1 mm.

The results in Table 4 show that by excluding the adjustments of the transverse shear moduli of the core, eqn (5), and reducing the transverse shear moduli of the facings, the buckling loads obtained by finite elements are within 4% of the theoretical predictions over the range of transverse shear moduli investigated. Furthermore, the collapse load is much larger than the buckling load and is rather insensitive to changes in the transverse shear moduli of the core. Below certain values of G_{xz} and G_{yz}, however, the collapse load will decrease in proportion to the decrease in buckling load.

Based on the FEA results, the facing on the compressive side would fail in a corner region due

Table 3. Tensile and compressive strengths of the facings

Layer No./ Stress	Strength (MPa)	
	x-direction	y-direction
1/Tensile	81·4	28·4
1/Compressive	24·7	13·3
3/Tensile	82·1	31·5
3/Compressive	23·9	13·0

Table 4. Buckling and collapse load ($w_o/h = 0.25$) versus the transverse shear moduli of the core

Transverse Shear Moduli (GPa)		Buckling Load (N)		Collapse Load (N)
G_{xz}	G_{vz}	$P_{cr,theor}$	P_{cr}	P_{col}
∞	∞	898	927	1410
3·5	35	846	849	1397
0·875	8·75	727	737	1220
0·35	3·5	584	608	1020

to the high in-plane shear stress acting in the corner regions. In panel compression experiments[7] a wrinkle was observed to initate in a corner region of the panel at approximately a 45° angle to the loading direction. The wrinkle then propagated rapidly towards the center of the panel. This is experimental indication that the collapse was due to high shear stresses.

The sensitivity to initial imperfection was examined by varying the amplitude w_o of the initial imperfection of the panel from 0·1 to 10 times the panel thickness. While large imperfections are unlikely to occur during board manufacture they can be introduced by warpage of the board when the humidity changes, e.g. from 50 to 90% RH, if the facings have different hygro-expansion coefficients.

Figure 9 shows the normalised collapse load, $P_{coll}/P_{cr,ref}$ versus the amplitude, w_o, of the initial imperfection of the panel. For reasonable imperfections, the collapse load is not very much affected, but for large imperfections, the collapse load is reduced by about 40%. Similar conclusions were obtained experimentally, Ref. 7. Failure occurred in the corner regions of the panels in a manner as discussed above.

The effect of stiffness asymmetry of the facings was studied by changing the thickness of the facings while maintaining constant total thickness of the facings and the board. The amplitude of the initial imperfection was set to $w_o = 1$ mm. The normalized collapse load is plotted versus the stiffness ratio of the facings in Fig. 10. The collapse load is quite sensitive to the asymmetry, but the failure initation mechanism according to the FEA was the same as described earlier. When the thickness of the facing on the concave side of the panel is increased and the thickness of the facing

on the convex side is decreased ($S_{2,f3}/S_{2,f1}$ is decreased from unity) a rise in the collapse load is observed in Fig. 10 until a certain asymmetry ratio is reached. Then a drastic reduction of the collapse load is observed because the panel abruptly starts to buckle in the direction opposite to the initial imperfection, i.e. the 'weakest or thinnest' liner becomes loaded in compression. This in turn is caused by the fact that the load is introduced at the middle plane of the panel and that the neutral plane shifts towards the facing on the concave side, which produces an eccentricity moment at the loaded edges. If the thickness of the facing on the concave side is decreased ($S_{2,f3}/S_{2,f1}$ is increased from unity), the facing on the compressive side will become weaker which produces a steady decrease of the collapse load.

Eccentric loading, Fig. 8, was studied using a symmetrical panel with an imperfection, $w_o = 1$ mm. The results in Fig. 11 shows a 15% reduction in the load carrying capability for a

Fig. 10.   Normalised collapse load versus the stiffness ratio of the liners, i.e. the asymmetry of the board.

Fig. 9.   Normalised collapse load versus imperfection amplitude (w_o/h) of the panel.
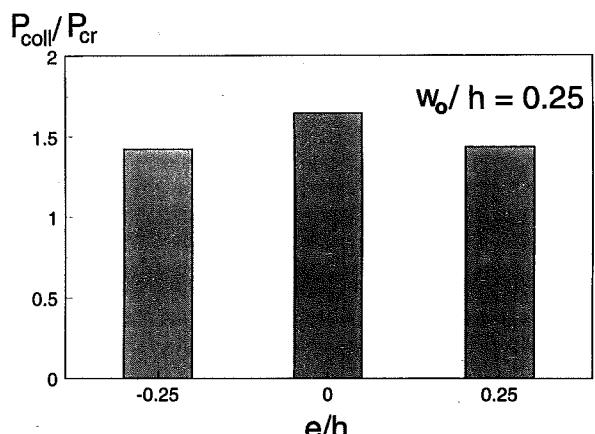
Fig. 11.   Normalised collapse load versus eccentricity e/h.

panel with an eccentricity (*e*) of one quarter of the panel thickness (*h*). The change in collapse load is almost the same regardless of the eccentricity, being towards or opposite the direction of the imperfection, see Fig. 8.

The moments at the horizontal edges, produced by eccentric load, bend the panel in a direction opposite the direction of the eccentricity. The eccentricity thus governs the direction of the buckling of the panel from the start because there is no shift in the neutral plane to balance this effect. The reduction in collapse load is partly attributed to additional compressive stress in the facing on the concave side of the panel due to the bending moments introduced by the eccentric load. The failure zone is expected to move closer to the corners because the in-plane shear stress becomes more concentrated at the corners. Thus, the introduction of load into a panel is very important for its load bearing capability.

Finally, the sensitivities of the buckling and collapse loads to the slenderness ratio, a/h, of the panel were analyzed. Both the side length a and the core thickness h_c of the panel were changed while the aspect ratio, a/b, and the thicknesses of the facings were kept constant. Figure 12 shows that the buckling load is proportional to the inverse square of the slenderness ratio which is also evident from eqn (4).

The collapse load responds quite differently to the changes in slenderness ratio, see Fig. 13. If the side length of the panel is increased at constant panel thickness, a rapid increase of the collapse load occurs for small slenderness ratios followed by a moderate increase in the collapse load for large slenderness ratios. In contrast, increasing the core thickness at constant panel side length and

thereby decreasing the slenderness ratio, will increase the collapse load. The collapse load of the panel is much more sensitive to changes in the core thickness, h_c, than to changes in the side length.

These results may give a somewhat misleading indication of how effectively the panels can carry compressive load. As illustrated in Fig. 14, by plotting the average stress on the loaded edges at collapse, $\bar{\sigma}_{coll}$, versus the slenderness ratio it is demonstrated that panels with small slenderness ratios carries load more effectively, as expected.

4 CONCLUSIONS

A parametric study of the influences of geometry, loading and material parameters on the buckling load and collapse load of a corrugated board panel has been presented. The parameters studied
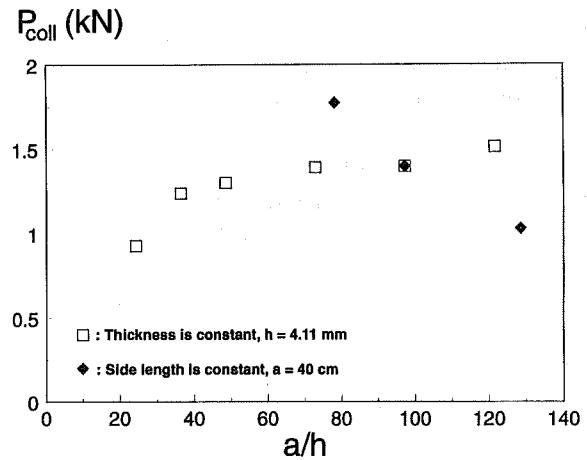
Fig. 13. Collapse load versus slenderness ratio of the panel.

Fig. 12. Buckling load versus slenderness ratio of the panel.
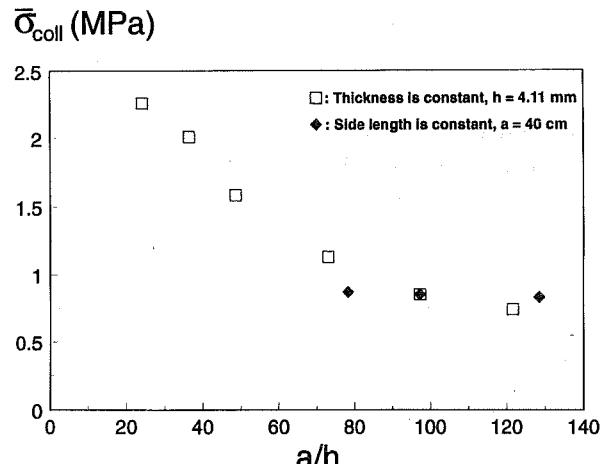
Fig. 14. Average stress on the loaded edges at collapse versus slenderness ratio of the panel.

are directly connected to the design, manufacture and use of corrugated boxes. Properties which are influenced by the manufacturing process are the transverse shear stiffness and initial imperfections. It was shown that they normally have a minor influence on the collapse load of panels. However, when the imperfection becomes large, e.g. ten times the thickness of the board, the collapse load is reduced by about 40%. Design factors such as stiffness asymmetry and slenderness ratio of the panel were shown to significantly influence the collapse load of the panel. Especially the stiffness asymmetry was shown to be important. The collapse load dropped about 20% when the buckling direction was reversed at a certain stiffness ratio. From a design point of view, the safest design should be a symmetrical board because it is difficult to predict at what level of asymmetry the change in buckling direction will occur.

The collapse load was found to be very sensitive to changes in core thickness, while it was rather insensitive to the panel size above a slenderness ratio of 40. By plotting the average stress on the loaded edges at collapse versus slenderness ratio it was shown that panels with a small slenderness ratio are most effective in carrying compressive load. The FEA indicated failure initiation at the corner regions in the facing on the compressive side of the panel due to high in-plane shear stress for all the parameters studied. The failure zone shifted towards the corner and the in-plane shear stress intensity increased when an eccentric load was introduced. Furthermore eccentic loading significantly reduced the collapse load of the panel thus stressing the importance of the load introduction to the panels.

ACKNOWLEDGMENTS

REFERENCES

1. Nordstrand, T., Allen, H. G. & Carlsson, L. A., Transverse shear stiffnesses of structural core sandwich, *Composite Structures*, 27 (1994) 317–29.
2. Nordstrand, T. & Carlsson, L. A., Experimental determination of transverse shear stiffnesses of structural core sandwich, to be published.
3. Walker, A. C., A brief review of plate buckling research, in *Behaviour of Thin-walled Structures*, Elsevier, (1984) 375–98.
4. Prabhakara, M. K. & Chia, C. Y., Post-buckling behaviour of rectangular orthotropic plates, *Journal of Mechanical Engineering Science*, 15 (1973) 25–33.
5. Harris, G. Z., The buckling and post-buckling behaviour of composite plates under biaxial loading, *International Journal of Mechanical Science*, 17 (1975) 187–202.
6. Robinson, J. R., The buckling and bending of orthotropic sandwich panels with all edges simply-supported, *Aeronautical Quarterly*, 6 (1955) 125–48.
7. Hahn, E. K., de Ruvo, A., Westerlind, B. S. & Carlsson, L. A., Compressive strength of edge-loaded Corrugated Board Panels, *Experimental Mechanics*, 32 (1992) 259–58.
8. Coan, J. M., Large-deflection theory for plates with small initial curvature loaded in edge compression, *Journal of Applied Mechanics*, 18 (1951) 143–51.
9. Yamaki, N., Post-buckling behaviour of rectangular plates with small initial curvature loaded in edge compression, *Journal of Applied Mechanics*, 26 (1959) 407–14.
10. Rhodes, J., Harvey, J. M. & Fok, W. C., The load-carrying capacity of initially imperfect eccentrically loaded plates, *International Journal of Mechanical Science*, 17 (1975) 161–75.
11. Noor, A. K., Starnes, J. H. & Waters, W. A., Numerical and experimental simulations of the postbuckling response of laminated anisotropic panels, *AIAA-90-0964-CP*, (1990), 848–61.
12. Libresen, L., Postbuckling analysis of shear deformable composite flat panels taking into account geometrical imperfections, *AIAA-90-0967-CP* (1990) 892–902.
13. Stein, M. Postbuckling of orthotropic composite plates loaded in compression, *AIAA Journal*, 21 (1983) 1729–35.
14. Folie, G. M., The behaviour and analysis of orthotropic sandwich plates, *Building Science*, 6 (1971) 57–67.
15. Zienkiewicz, O. C., *The Finite Element Method in Engineering Science*, (1971) McGraw-Hill.
16. Ahmad, S., Irons, B. M., & Zienkiewicz, O. C., Analysis of thick and thin shell structures by curved finite elements, *International Journal for Numerical Methods in Engineering*, 2 (1970) 419–51.
17. Cook, R. D., Malkus, D. S. & Plesha, M. E., *Concepts and Applications of Finite Element Analysis*, (1989), John Wiley & Sons.
18. *ANSYS User's Manual*, (1989), Swanson Analysis Systems Inc., Vol. 1–2.
19. Carlsson, L., Fellers, C. & Jonsson, P., The bending stiffness of corrugated board under special consideration of asymmetrical and multi-ply construction (in German), *Das papier*, 4 (1985) 149–56.
20. Libove, C. & Hubka, R. E., Elastic constants for corrugated core sandwich plates, (1951), *NACA TN 2289*.
21. Baum, G. A., Brennan, D. C. & Habeger, C. C., Orthotropic elastic constants of paper, *Tappi J.*, 64 (1981) 97–101.
22. Nordstrand, T. M., On buckling loads for edge loaded orthotropic plates including transverse shear, to be published.
23. Palazotto, A. N. & Dennis, S. T., Nonlinear analysis of shell structures, *AIAA Education Series*, (1992) 116–54.
24. Reddy, J. N., Energy and Variational Methods in Applied Mechanics, (1994), John Wiley.
25. Tsai, S. W. & Wu, E. M., A general theory of strength for

anisotropic materials, *Journal of Composite Materials*, (January, 1971) 58–80.

26. Fellers, C., Westerlind, B. & de Ruvo, A., An investigation of the biaxial failure of paper: experimental study and theoretical analysis, *Transaction of the Symposium*

held at Cambridge: September 1981, 1 (1983) 527–59, Mechanical Engineering Publications Ltd.

27. Paetow, R. & Göttsching, L., Poisson's ratio of paper, *Das Papier* (in German), 6 (1990) 229–37.

APPENDIX

Estimation of error in bending stiffness along the corrugations

The bending stiffness along the corrugations of the corrugated board is given by Ref. 19

$$D_y \approx S_{2,f1} \frac{(h - t_{f1})^2}{4} + S_{2,f3} \frac{(h - t_{f3})^2}{4} + S_{2,c} \frac{I_{y,c}}{t_c} \tag{A1}$$

where $S_{2,f1}$, $S_{2,f3}$ and $S_{2,c}$ are the tensile stiffnesses of the facings and the corrugated sheet respectively. The second moment of area of the core $I_{y,c}$ is given in Ref. 19. t_{f1}, t_{f3}, t_c and h are the thicknesses of the constituents and the board respectively, see Fig. 3. If the wall thickness of the corrugated sheet is small compared to the core height, the wavelength is about twice the core height and the thicknesses of the constituents are similar, the bending stiffness can be approximated as

$$D_{y,app} \approx S_{2,f1} \frac{(h - t_{f1})^2}{4} + S_{2,f3} \frac{(h - t_{f3})^2}{4} + \alpha S_{2,c} \frac{h_c}{12} \tag{A2}$$

where α is the take-up factor, i.e. the ratio between the arc-length and wavelength of the corrugated sheet. Using the data for the reference panel one obtains

$$\frac{D_{y,app}}{D_y} \approx 0.958 \tag{A3}$$

Thus the error is less than 5% which is acceptable for our purpose.

Paper 5

_____

Analysis and Testing of Corrugated Board Panels into the Post-buckling Regime

by

T. Nordstrand

To be submitted to Composite Structures.

Analysis and Testing of Corrugated Board Panels into the Post-buckling Regime

Tomas Nordstrand

SCA Research, Box 716, 851 21 Sundsvall, Sweden

ABSTRACT

Testing of the load bearing capacity of corrugated board boxes is often associated with uncertainties, e.g. the creases along the edges of the side panels introduce eccentricities. An alternative to the testing of boxes is therefore attractive. One suggestion is testing of panels. However, panels are sensitive to the boundary conditions. A panel compression test (PCT-) rig, similar to a test frame for metal plates designed by A. C. Walker, was therefore built to achieve accurately defined load and boundary conditions. The PCT-rig furnishes simply supported boundary conditions, i.e. the edges of the panel are prevented from moving out-of-plane without any rotational restraint. The edges are also free to move in-plane. In order to describe the buckling behaviour, a non-linear buckling analysis of orthotropic plates, derived by Banks and Harvey, was modified to include initial imperfections. The critical buckling load of the panels was evaluated by fitting the analytical expression by non-linear regression to experimentally measured load-displacement curves. The results show a difference in the order of 15-20 % between experimentally estimated critical buckling load and the analytically predicted critical buckling load for orthotropic plates. This is mainly attributed to transverse shear deformations. A corresponding difference was observed between analytically predicted and experimentally measured load-displacement curves at large out-of-plane deformation, i.e. twice or three times the board thickness. This is probably caused by the non-linear response of paper at high stresses and local buckling of the panel facings, i.e. the liners. A predicted failure load of the corrugated board panel was determined when stresses in the facings reached the Tsai-Wu failure criterion. The predicted failure load and measured average experimental failure load were close, indicating that collapse of the panel is triggered by material failure of one of the liners.

NOTATIONS

a, b	Plate size in *x* and *y* directions
A, A_0	Amplitudes of the total and initial plate deflection functions
A_i	Relative amplitude of the shape function
D_{ij}	Bending stiffness of the plate
E_{ij}	Modulus of elasticity of liner
$E_{ij,c}$	Modulus of elasticity of medium
G_{ij}	Shear modulus of liner
F	Airy's stress function
h	Plate thickness
h_c	Core thickness
t_f	Liner thickness
t_c	Medium thickness
α	Take-up factor
M_x, M_y, M_{xy}	Bending and twisting moments per unit distance in middle surface of the plate
N_x, N_y, N_{xy}	Membrane forces per unit distance in middle surface of the plate
P	Load
P_{crit}	Critical buckling load
u, v, w	Displacements in *x, y* and *z* directions
V	Strain energy
x, y, z	Cartesian co-ordinates
γ	Unit shear strain
$\varepsilon_x, \varepsilon_y$	Unit normal strains in *x* and *y* directions of the facings
v_{ij}	Poisson's ratio
σ_x, σ_y	Unit normal stresses in *x* and *y* directions
τ_{xy}	Unit shear stress on plane perpendicular to the *x*-axis and parallel to the *y*-axis

INTRODUCTION

Corrugated board is one of our most common transport packaging materials. Large retailers and distributors are under increasing pressure to cut the cost of corrugated packaging. With the increasing scale of business it has become unacceptable to over design boxes. Consequently, it is necessary to predict box strength in order to obtain boxes at the lowest possible cost.

However, analysis of top-to-bottom compression loading of boxes is often associated with uncertainties, e.g. the creases between flaps and side panels introduce eccentricities along the loaded edges [1]. Since the buckling behaviour is of primary interest, it was decided to test corrugated board panels with clean cut edges in a specially designed panel compression rig, similar to a test frame for metal plates [2]. The panel compression rig furnishes simply supported boundary conditions, i.e. the edges of the panel are prevented from moving out-of-plane without any rotational restraint. The edges are also free to move in-plane. It was decided to measure the out-of-plane displacement at the centre of the panel versus the compressive load. Out-of-plane measurement of the panel deformation is easier than in-plane measurement. It also simplifies (de-)mounting of the panel in the rig.

One objective of the tests is to obtain the critical buckling load. Since post-buckling of a panel is stable, an analytical expression was needed that relates the compressive load to the deformation of the panel. Banks and Harvey [3] originally derived a post-buckling analysis, which has been modified in the presented model to include initial imperfections. Panels are assumed to have orthotropic elastic constants as described by Jones [4]. The critical buckling load of the panels was evaluated by fitting an analytical expression for the load-deformation curve to the experimentally measured curves. The fitting was made by non-linear regression analysis and comprised the determination of three parameters in the analytical expression, one being the buckling load, another the post-buckling coefficient and the third the amplitude of the initial imperfection of the panel.

Results show a discrepancy of 15-20 % between experimentally estimated critical buckling load and the theoretically predicted buckling load for orthotropic plates. This difference is mainly attributed to transverse shear. A corresponding load difference was observed between analytically predicted and experimentally measured post-buckling curves at large deflections, i.e. twice or three times the board thickness. This is probably caused by the non-linear material response of paper at high stresses and by local buckling of the panel facings, i.e. the liners. A failure load of the corrugated board panel was predicted by determining when stresses in the facings reached the Tsai-Wu failure criterion [5]. The predicted failure load and measured average experimental failure load were close, indicating that collapse of the panel is triggered by material failure of one of the liners. Thus, the strength of the material is efficiently utilised.

THEORETICAL MODEL

Basic assumptions and mechanics principles of a corrugated board panel

A simply supported corrugated board panel, loaded in compression, buckles in a stable manner and carries load beyond the critical buckling load until compressive failure occurs. Since the paper sheets used in the panel are thin compared to the overall thickness of the panel, the variations of stresses in the thickness direction of each sheet are ignored.
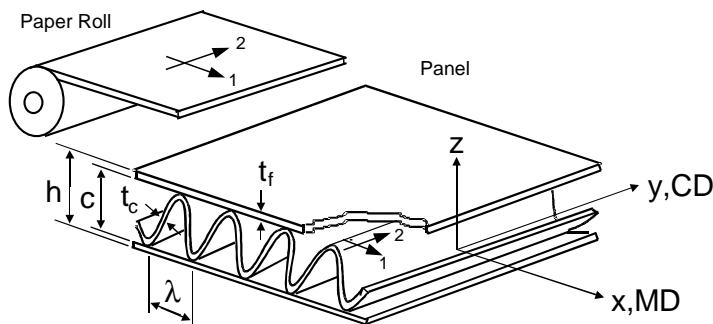
Figure 1. Geometry and orientation of a symmetrical corrugated board panel.

The paper is assumed to have orthotropic elastic properties with the elastic planes of symmetry of the facings coinciding with the Cartesian coordinate system xyz of the panel, see Figure 1. Total thickness of the panel is h, core height is c and facings and core sheet are assumed to have thickness t_f and t_c, respectively.

The membrane forces N_x, N_y and N_{xy} are shown in Figure 2. These forces are oriented according to the orientation of the panel in the loaded state. The displacements are assumed to be small in the sense that $\sin(\partial w / \partial x_i) = \partial w / \partial x_i$, $i = 1, 2$ and the projected membrane forces in the x-y plane are in equilibrium.
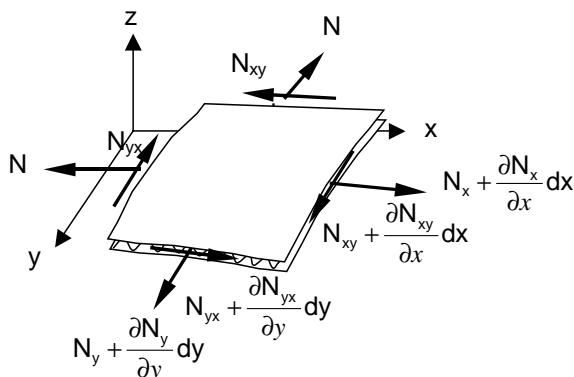
Figure 2. Membrane forces in the corrugated board panel.

It is assumed that the membrane strains are constant through the thickness of the panel and that membrane forces carried by the corrugated core in x-direction can be disregarded. The strains in panel facings due to membrane forces are

$$
\begin{bmatrix} \varepsilon_x \\ \varepsilon_y \\ \gamma_{xy} \end{bmatrix} = \begin{bmatrix} \dfrac{h}{2t_f E_{11}} & -v_{21}\dfrac{h\hbar}{2t_f E_{22}} & 0 \\ -\hbar v_{12}\dfrac{h}{2t_f E_{11}} & \dfrac{h\hbar}{2t_f E_{22}} & 0 \\ 0 & 0 & \dfrac{h}{2t_f G_{12}} \end{bmatrix} \begin{bmatrix} \dfrac{N_x}{h} \\ \dfrac{N_y}{h} \\ \dfrac{N_{xy}}{h} \end{bmatrix}
\tag{1}
$$

where $\hbar = \dfrac{1}{1 + \dfrac{\alpha\, t_c}{2t_f}\dfrac{E_{22,c}}{E_{22}}}$ and v_{ij}, E_{ij} i,j $=1,2$ and G_{12} are the Poisson´s ratio, elastic and

shear modulus of the facings, respectively. $E_{22,c}$ is the elastic modulus of the core

sheet in the cross direction CD and α is the take-up factor, i.e. the ratio between the

length of the corrugated core sheet and the length of the board.
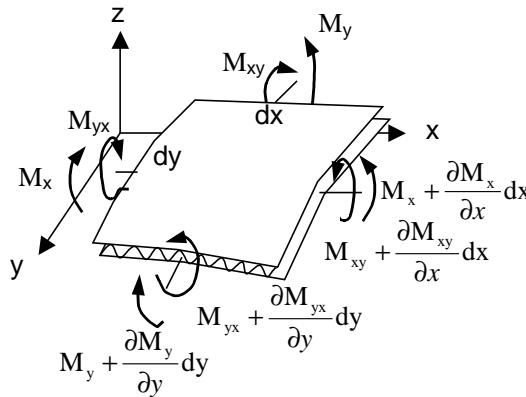
Figure 3.   Bending of the corrugated board panel.

The bending and twisting curvatures and strains in the facings $z = \pm\dfrac{(h - t_f)}{2}$

$$
\kappa_x = \frac{\varepsilon_x(z) - \varepsilon_x(0)}{z} = -\frac{\partial^2 w}{\partial x^2}, \quad \kappa_y = \frac{\varepsilon_y(z) - \varepsilon_y(0)}{z} = -\frac{\partial^2 w}{\partial y^2}, \quad \kappa_{xy} = \frac{\gamma_{xy}(z) - \gamma_{xy}(0)}{z} = -2\frac{\partial^2 w}{\partial x \partial y}
\tag{2}
$$

are connected to the bending and twisting moments acting on the panel in Figure 3 by

$$
\begin{bmatrix} M_x \\ M_y \\ M_{xy} \end{bmatrix} = \begin{bmatrix} D_{11} & D_{12} & 0 \\ D_{12} & D_{22} & 0 \\ 0 & 0 & D_{66} \end{bmatrix} \begin{bmatrix} \kappa_x \\ \kappa_y \\ \kappa_{xy} \end{bmatrix}
\tag{3}
$$

where D_{ij} are elements of the bending stiffness matrix [4,5].

3

Buckling of a corrugated board panel

When a panel with a small initial curvature is subjected to a compressive load it bends, and the deflection may become large in comparison with the thickness of the board, see Figure 4. Hence the geometrical non-linearity due to membrane stretching has to be included in the analysis [6]. It is assumed that the membrane strains are constant through the thickness of the panel, and can be expressed in terms of the displacements at z=0 as follows

$$\varepsilon_x = \frac{\partial u}{\partial x} + \frac{1}{2}\left(\frac{\partial w}{\partial x}\right)^2$$

$$\varepsilon_y = \frac{\partial v}{\partial y} + \frac{1}{2}\left(\frac{\partial w}{\partial y}\right)^2 \tag{4}$$

$$\gamma_{xy} = \frac{\partial u}{\partial y} + \frac{\partial v}{\partial x} + \frac{\partial w}{\partial x}\frac{\partial w}{\partial y}$$

By adding the second derivative of ε_x with respect of y and second derivative of ε_y with respect of x and subtracting the second derivative of γ_{xy} with respect of *x* and *y*, a compatibility relation is obtained between the membrane strains and the out-of-plane displacement [6].

$$\frac{\partial^2 \varepsilon_x}{\partial y^2} + \frac{\partial^2 \varepsilon_y}{\partial x^2} - \frac{\partial^2 \gamma_{xy}}{\partial x \partial y} = \left(\frac{\partial^2 w}{\partial x \partial y}\right)^2 - \frac{\partial^2 w}{\partial x^2}\frac{\partial^2 w}{\partial y^2} \tag{5}$$

If the expression in the stiffness matrix is substituted with the effective elastic stiffnesses of the panel as follows

$$E_{11}^* = \frac{2t_f}{h}E_{11}, \ E_{22}^* = \frac{2t_f}{h\hbar}E_{22}, G_{12}^* = \frac{2t_f}{h}G_{12}, v_{12}^* = \hbar v_{12} \tag{6}$$

and the strains are subsequently substituted in eq. (2) we obtain

$$\frac{1}{hE_{22}^*}\frac{\partial^2 N_y}{\partial x^2} - \frac{1}{h}\left(\frac{1}{G_{12}^*} + \frac{2v_{12}^*}{E_{11}^*}\right)\frac{\partial^2 N_{xy}}{\partial x \partial y} + \frac{1}{hE_{11}^*}\frac{\partial^2 N_x}{\partial y^2} = \left(\frac{\partial^2 w}{\partial x \partial y}\right)^2 - \frac{\partial^2 w}{\partial x^2}\frac{\partial^2 w}{\partial y^2} \tag{7}$$

The solution of eq. (7) can be greatly simplified by introducing Airy's stress function, *F* [6]. With this stress function the membrane forces in eq. (7) can be expressed as

$$N_x = h\frac{\partial^2 F}{\partial y^2}, N_y = h\frac{\partial^2 F}{\partial x^2}, N_{xy} = -h\frac{\partial^2 F}{\partial x \partial y} \tag{8}$$

where *F=F(x,y)*. With these expressions for the forces, eq. (7) becomes

$$\frac{1}{E_{22}^*}\frac{\partial^4 F}{\partial x^4}+\left(\frac{1}{G_{12}^*}-\frac{2\nu_{12}^*}{E_{11}^*}\right)\frac{\partial^4 F}{\partial x^2\partial y^2}+\frac{1}{E_{11}^*}\frac{\partial^4 F}{\partial y^4}=\left(\frac{\partial^2 w}{\partial x\partial y}\right)^2-\frac{\partial^2 w}{\partial x^2}\frac{\partial^2 w}{\partial y^2} \qquad (9)$$

If $w=w(x,y)$ is the total out-of-plane displacement and $w_0=w_0(x,y)$ is an initial imperfection of the plate, eq. (9) can be written as

$$\frac{1}{E_{22}^*}\frac{\partial^4 F}{\partial x^4}+\left(\frac{1}{G_{12}^*}-\frac{2\nu_{12}^*}{E_{11}^*}\right)\frac{\partial^4 F}{\partial x^2\partial y^2}+\frac{1}{E_{11}^*}\frac{\partial^4 F}{\partial y^4}=$$
$$\left(\frac{\partial^2 w}{\partial x\partial y}\right)^2-\frac{\partial^2 w}{\partial x^2}\frac{\partial^2 w}{\partial y^2}-\left[\left(\frac{\partial^2 w_0}{\partial x\partial y}\right)^2-\frac{\partial^2 w_0}{\partial x^2}\frac{\partial^2 w_0}{\partial y^2}\right] \qquad (10)$$

provided that the total displacements and the initial imperfections have the same shape, differing only in magnitude. This equation links the membrane stresses with out-of-plane displacements of orthotropic plates.
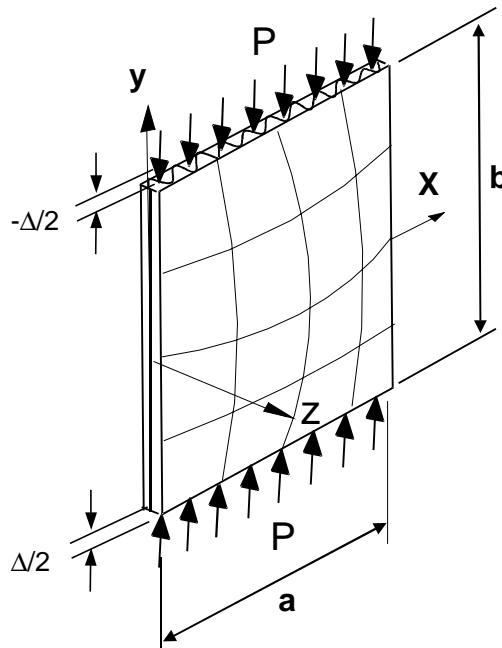
Figure 4. Simply supported corrugated board panel with compression of top and bottom edges.

Boundary conditions

It is assumed that the panel is simply supported, see Figure 4. This means that edges are rotationally unrestrained and no out-of-plane displacement is present. Neither are in-plane shear stresses allowed. Thus at the unloaded edges $x=0, a$:

$$w = 0$$

$$M_x = -D_{11}\left(\frac{\partial^2 w}{\partial x^2} + v_{21}\frac{\partial^2 w}{\partial y^2}\right) = 0 \tag{11}$$

$$\tau_{xy} = 0$$

$$\sigma_x = 0$$

The compressive displacements are constant along the loaded edges. Thus, at $y = \pm\dfrac{b}{2}$, the conditions are

$$w = 0$$

$$M_y = -D_{22}\left(\frac{\partial^2 w}{\partial y^2} + v_{12}\frac{\partial^2 w}{\partial x^2}\right) = 0$$

$$\tau_{xy} = 0$$

$$v = \mp\frac{\Delta}{2} \tag{12}$$

Solution strategy

In order to obtain a relationship between the compression v and out-of-plane displacement w the principle of minimum potential energy is used [3]. The total potential strain energy V in the buckled plate consists of two parts - the potential energy of bending and twisting, V_B, and the membrane strain energy, V_M.

$$V = V_B + V_M$$

$$V_B = \frac{1}{2}\int_0^a\int_{-\frac{b}{2}}^{\frac{b}{2}}\left[D_{11}\left(\frac{\partial^2}{\partial x^2}(w-w_0)\right)^2 + 2D_{11}v_{21}\left(\frac{\partial^2}{\partial x^2}(w-w_0)\right)\left(\frac{\partial^2}{\partial y^2}(w-w_0)\right)+\right.$$

$$\left.+D_{22}\left(\frac{\partial^2}{\partial y^2}(w-w_0)\right)^2 + 4D_{66}\left(\frac{\partial^2}{\partial x\partial y}(w-w_0)\right)^2\right]dydx \tag{13}$$

$$V_M = \frac{h}{2}\int_0^a\int_{-\frac{b}{2}}^{\frac{b}{2}}\left[\frac{1}{E_{11}}\left(\frac{\partial^2 F}{\partial y^2}\right)^2 - \frac{2v_{12}}{E_{11}}\left(\frac{\partial^2 F}{\partial y^2}\frac{\partial^2 F}{\partial x^2}\right) + \frac{1}{G_{12}}\left(\frac{\partial^2 F}{\partial x\partial y}\right)^2 + \frac{1}{E_{22}}\left(\frac{\partial^2 F}{\partial x^2}\right)^2\right]dydx$$

Before minimising the total energy V, the out-of-plane displacement w and the initial imperfection w_0 are prescribed as follows [3]

$$w = A\overline{X}(x)\cos\left(\frac{\pi y}{b}\right) \tag{14}$$

$$w_0 = A_0\overline{X}(x)\cos\left(\frac{\pi y}{b}\right) \tag{15}$$

6

where A and A_0 are the amplitude of the out-of-plane displacement and initial imperfection, respectively. The panel is accordingly assumed to have a sinusoidal shape in y-direction and $\overline{X}(x)$ is a polynomial

$$\overline{X} = 3.2\left(\frac{x}{a} - 2\left(\frac{x}{a}\right)^2 + \left(\frac{x}{a}\right)^4 \right) \tag{16}$$

that describes the deflected shape of the panel in x-direction, see Figure 5.
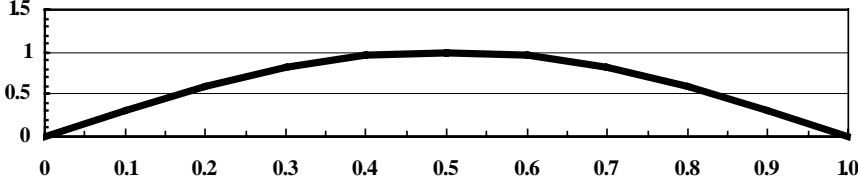
Figure 5.　　　Shape function used to model the buckled plate.

Integration of the membrane deformation $\partial v / \partial y$ in eq.(4) is equal to the uniform compression of the panel given by eq.(12)

$$v = \int_{-\frac{b}{2}}^{\frac{b}{2}} \left[\varepsilon_y - \frac{1}{2}\left(\frac{\partial w}{\partial y}\right)^2 + \frac{1}{2}\left(\frac{\partial w_0}{\partial y}\right)^2 \right] dy \tag{17}$$

Combining eq.(1), (6) and (8) gives

$$\varepsilon_y = \frac{1}{E_{22}^*}\left(\frac{\partial^2 F}{\partial x^2} - v_{21}\frac{\partial^2 F}{\partial y^2} \right) \tag{18}$$

Assuming a solution to eq.(10) [3] for a panel with uniform compression of its edges as shown in Figure 4

$$F = F_1(x) + F_2(x)\cos\left(\frac{2\pi y}{b}\right) \tag{19}$$

Substitution of eq. (14), (15), (18) and (19) into eq.(17) and integrating gives

$$\frac{\partial^2 F_1}{\partial x^2} = E_{22}^*\frac{v}{b} + \frac{E_{22}^*}{4}\left(\frac{\pi}{b}\right)^2\left(A^2 - A_0^2\right)\overline{X}^2 \tag{20}$$

Substitution of eq.(14), (15), (19) and (20) into eqs. (13) and minimising with respect to A yields the relationship between A and v

$$v = -\left(1 - \frac{A_0}{A}\right)\frac{C_1}{C_2} - \left(A^2 - A_0^2\right)\frac{C_3}{C_1} \tag{21}$$

where constants C_1, C_2 and C_3 are presented in the Appendix with a detailed solution.

Substitution of eq.(21) into (20) the relationship between the applied load P and out-of-plane displacement A is given by integrating the stress σ_y over the loaded edge $y=b/2$

$$P = -h\int_0^a \sigma_y dx = -h\int_0^a \frac{\partial^2 F}{\partial x^2} dx = -h\int_0^a \frac{\partial^2 F_1}{\partial x^2} dx \tag{22}$$

Further integration of eq.(22) gives

$$P = P_{crit}\left(1 - \frac{A_0}{A}\right) + \Psi\left(A^2 - A_0^2\right) \tag{23}$$

where the critical buckling load

$$P_{crit} = E_{22}^* \frac{ah}{b} \frac{C_2}{C_1} \tag{24}$$

and the post-buckling parameter is

$$\Psi = \left[\frac{E_{22}^* ah}{b} \frac{C_3}{C_1} - 2C_1\right] \tag{25}$$

Failure criterion

From the solution above, the total stresses in the inner facing $z = -(h - t_f)/2$ of the panel in Figure 4

$$\sigma_x = \frac{h}{2t_f} \frac{\partial^2 F}{\partial y^2} + \frac{D_{11}}{(h-t_f)t_f}\left(\frac{\partial^2}{\partial x^2}(w-w_0) + v_{21}\frac{\partial^2}{\partial y^2}(w-w_0)\right)$$

$$\sigma_y = \frac{h\hbar}{2t_f} \frac{\partial^2 F}{\partial x^2} + \frac{D_{22}}{(h-t_f)t_f}\left(\frac{\partial^2}{\partial y^2}(w-w_0) + v_{12}\frac{\partial^2}{\partial x^2}(w-w_0)\right) \tag{26}$$

$$\tau_{xy} = -\frac{h}{2t_f} \frac{\partial^2 F}{\partial x\partial y} + \frac{2D_{66}}{(h-t_f)t_f}\left(\frac{\partial^2}{\partial x\partial y}(w-w_0)\right)$$

can be obtained for a specified value of the out-of-plane deformation A. Subsequently, the stresses in eq. (26) are inserted in the Tsai-Wu failure criterion assuming plane stress [5]

$$\Gamma_1\sigma_x + \Gamma_2\sigma_y + \Gamma_{11}\sigma_x^2 + \Gamma_{22}\sigma_y^2 + \Gamma_{66}\tau_{xy}^2 + 2\Gamma_{12}\sigma_x\sigma_y = 1 \tag{27}$$

where $\Gamma_{11} = -\dfrac{1}{\sigma_{x,t}\sigma_{x,c}}$, $\Gamma_{22} = -\dfrac{1}{\sigma_{y,t}\sigma_{y,c}}$, $\Gamma_{12} = -0.36\sqrt{F_{11}F_{22}}$, $\Gamma_1 = \dfrac{1}{\sigma_{x,t}} + \dfrac{1}{\sigma_{x,c}}$,

$\Gamma_2 = \dfrac{1}{\sigma_{y,t}} + \dfrac{1}{\sigma_{y,c}}$, $\Gamma_{66} = \dfrac{1}{\sigma_{x,c}\sigma_{y,c}}$

The subscript $j=t$ or $j=c$ of strength $\sigma_{i,j}$,$i=x,y$, denote the strength in tension and compression, respectively. The expressions for Γ_{12} and Γ_{66} are approximations for paper materials [7]. A geometrical interpretation of the failure criterion, eq. (27), is depicted in Figure 6. Failure occurs when the total stress vector [σ_x, σ_y, τ_{xy}] of a facing reaches the surface of the ellipsoid in Figure 6.
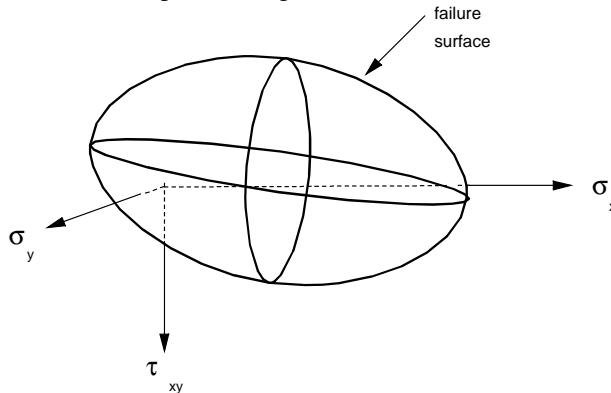
Figure 6. Geometrical interpretation of the Tsai-Wu failure criterion.

PANEL COMPRESSION TESTS

A panel compression rig was built similar to a test frame for metal plates designed by A. C. Walker [2], see Figure 7. The rig is composed of a frame that supports the bottom and side edges of the panel, and a crosshead that slides in the frame, supports the top edge and loads the panel. In this way the crosshead is guided to prevent out-of-plane movements. Furthermore, top and bottom supports consist of sectioned slotted rollers supported by needle bearings and mounted in grooves in the base plate and the crosshead. The panel is subsequently inserted into the slots.

The side edges are prevented from moving out-of-plane by knife-edge supports. Furthermore, the out-of-plane displacement at the panel centre is measured by a digital displacement gauge, see Figure 7 and Figure 8. Panels size 400x400 mm were cut from corrugated board and tested under compression with the cross-direction (CD) oriented in the direction of loading. Only flat panels with an imperfection less than half the thickness were selected for testing. Specimens were preconditioned for 24 hours at 30% RH, 23 ^{o}C, and subsequently conditioned for 24 hours at 50% RH, 23 ^{o}C, before testing. A total of 12 panels were tested and material and panel data is presented in Tables 1 and 2, respectively.
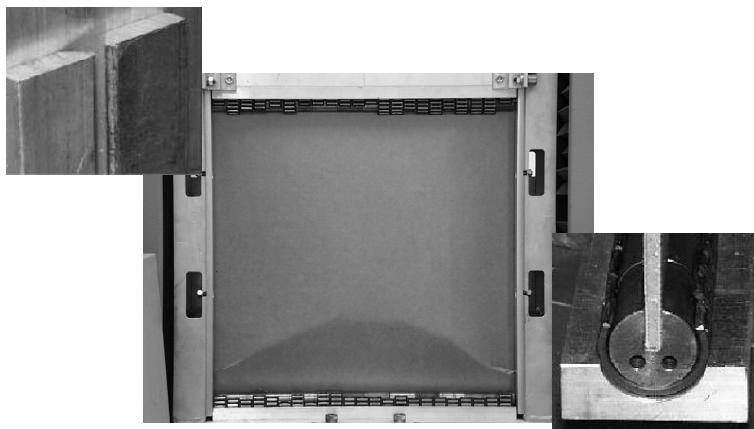
Figure 7. Panel compression rig and a corrugated board panel loaded to failure.

Figure 8. Measuring the deflection of a corrugated panel.

Table 1. Material data for liner and fluting of the corrugated board.

	Unit	Direction	Inner Facing Kraft Liner Single Facer	Core Semi-Chemical Medium	Outer. Facing Kraft Liner Double Backer
Basis weight	g/m^2		184.3	140.2	187.4
Thickness, t	mm		0.268	0.217	0.244
Elastic modulus, E_{11}	N/mm^2	MD	7980	4750	8090
Elastic modulus, E_{22}	N/mm^2	CD	3190	1560	2490
Tensile strength, $\sigma_{x,t}$	N/mm^2	MD	81.4	46.9	82.1
Tensile strength, $\sigma_{y,t}$	N/mm^2	CD	28.4	18.8	31.5
Compr. Strength, $\sigma_{x,c}$	N/mm^2	MD	30.8	23.1	29.9
Compr. Strength, $\sigma_{y,c}$	N/mm^2	CD	16.6	13.4	16.2

Table 2. Corrugated board data calculated using material data in Table 1. Transverse
shear stiffness values are measured values using three-point bending [8].

Basis weight	g/m^2	556
Thickness, h	mm	4.02
Corrugation wavelength, λ	mm	7.26
Bending stiffness, D_{11}	Nm	14.6
Bending stiffness, D_{22}	Nm	5.43
Bending stiffness, D_{12}	Nm	2.71
Bending stiffness, D_{66}	Nm	3.34
Transverse shear stiffness, A_{44}	N/mm	39.2
Transverse shear stiffness, A_{55}	N/mm	5.6

RESULTS AND DISCUSSION

The load-displacement curves of the tested corrugated board panels show consistent
buckling behaviour, see Figure 9. The dashed line is the analytical solution according
to eq. (23) using the material and panel data in Tables 1 and 2, giving the critical
buckling load P_{crit} = 958 N, which is in accordance with classical buckling theory for
orthotropic plates [4,11], and the post-buckling parameter Ψ= 8.6 N/mm^2, see Table 3.
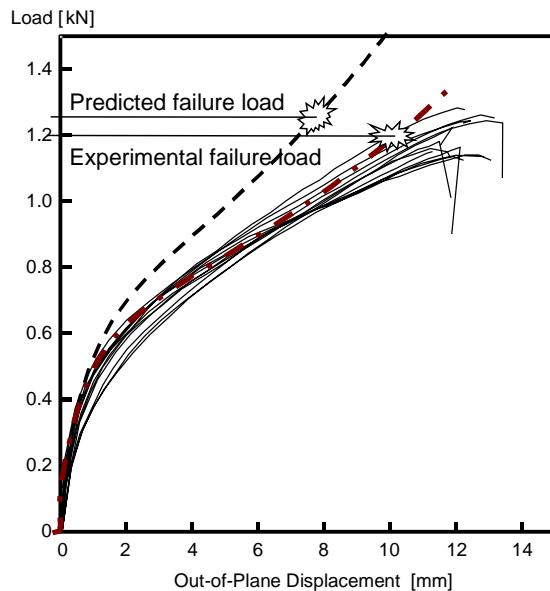
Figure 9.   Load-displacement curves of 12 corrugated board panels. The dashed
curve is the theoretical model with the analytical buckling load and post-
buckling parameter. Failure predicted using the Tsai-Wu failure criterion.
The dot-dashed curve is the theoretical model fitted to experimental
curves.

Table 3.   Analytically and experimentally determined parameters.

	$P_{crit,exp}$	P_{crit}	A_0	Ψ_{exp}	Ψ	$P_{fail, exp}$	P_{fail}
Unit	N	N	mm	N/mm^2	N/mm^2	N	N
Average	814	958	0.8	3.55	8.6	1195	1265
Std	16		0.3	0.59		60	
Max	844		1.3	4.68		1288	
Min	786		0.5	2.88		1138	

When the analytical out-of-plane deflection A has reached levels about half the plate thickness, the difference in analytical and experimental loads is about 20%. The brown dot-dashed line was determined by fitting the analytical expression in eq. (23), i.e. parameters $P_{crit,exp}$, Ψ_{exp} and A_0, to the experimental curves using non-linear regression.

The regression was made using commercially available software called SAS [9]. The experimental critical buckling load $P_{crit,exp} = 814$ N and the post-buckling coefficient $\Psi_{exp} = 3.55$ N/mm^2 for the tested panels, see Table 3. The analytically and experimentally determined critical buckling loads differ by 18 %.

The discrepancy between analytical and experimental post-buckling parameters in Table 3 is probably due to the non-linear response of the paper material at high stresses and local buckling of the facings, see Figure 10 [10]. However, the analytically calculated failure load $P_{fail} = 1265$ N differs only 6 % from the experimental failure load of $P_{fail,exp} = 1195$ N. The analytical failure load was obtained by checking when the stresses [σ_x, σ_y, τ_{xy}] in the inner facing satisfied the Tsai-Wu failure criterion in eq. (16). In Figure 11, failure of the inner facing is depicted by a range of colour fields indicating how close the material is to failure. This is expressed by the ratio between the length of the vector [σ_x, σ_y, τ_{xy}] and an aligned vector that reaches the surface of the ellipsoid in Figure 6.
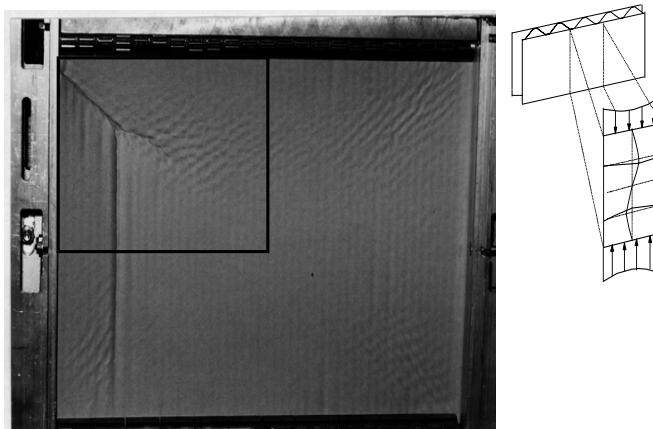
Figure 10. Local buckling of the facing on the concave side is visible just prior and after failure.
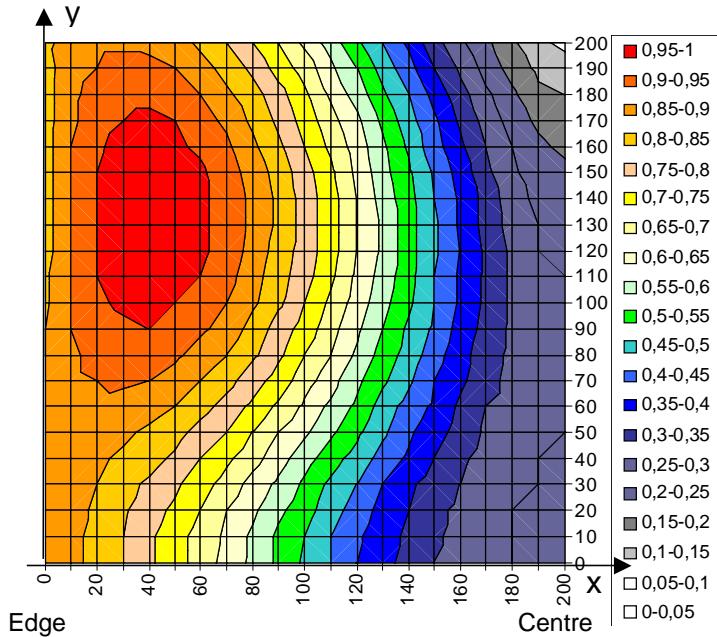
Figure 11. Colour fields indicate how close to material failure different areas of the inner facing are according to the Tsai-Wu criterion. Due to symmetry only the top-left quarter of the panel is shown.

CONCLUSIONS

A rig that furnishes simply supported boundary conditions has been designed to test corrugated board panels. Experimental results are consistent. An expression linking applied load with the out-of-plane deformation is derived. The first part of the expression is similar to ordinary Euler buckling of a column, where the maximum compressive load is limited by the critical buckling load. In the second part of the expression the membrane forces produce a parabolic relationship between the compressive load and out-of-plane displacement. The expression was fitted to experimental measured curves using non-linear regression to evaluate the critical buckling load and post-buckling coefficient for corrugated board panels. The results show an 18 % difference between experimentally estimated critical buckling load and the analytically predicted critical buckling load for orthotropic plates. This is partly attributed to excluded transverse shear deformation in the analytical solution. Compare the experimental value of 814 N with 870 N obtained from an analysis of a panel including transverse shear deformation [11,12]. A significant difference was also observed between analytically predicted and experimentally measured load-displacement curves at large out-of-plane deformation. This is probably caused by the non-linear material behaviour of paper and local buckling of the panel facings, i.e. the liners. However, the 6 % difference between the analytically calculated failure load and the experimental failure load is quite small. This suggests that collapse of the corrugated board panel is triggered by material failure of the inner facing. The strength of the material is therefore efficiently utilised.

13

REFERENCES

1. M. Renman, "A mechanical characterization of creased zones of corrugated board", Licentiate thesis, Department of Engineering Logistics, Lund University, Sweden, 1994.

2. A. C. Walker, "Thin Walled Structural Forms under Eccentric Compressive Load Actions"*,* Ph. D Thesis, University of Glasgow, June, 1964.

3. J. Rhodes and J. M. Harvey, "Examination of Plate Post-Buckling Behaviour", Journal of the Eng. Mech. Div., vol. 103, No. EM3, pp. 461-478, 1977.

4. R. M. Jones, "Mechanics of Composite Materials", Hemisphere Publishing Corp. New York, 1975.

5. C. Fellers, B. S. Westerlind and A. de Ruvo, "An Investigation of the Biaxial Failure of Paper: Experimental Study and Theoretical Analysis", Transaction of the Symposium held at Cambridge: September 1981, Vol. 1, pp. 527-559, 1983.

6. S. P. Timoshenko and J. M. Gere, "Theory of Elastic Stability"*,* McGraw-Hill, 1961.

7. L. A. Carlsson, T. Nordstrand and B. Westerlind, "On the Elastic Stiffnesses of Corrugated Core Sandwich", Journal of Sandwich Structures and Materials, Vol. 3, pp. 253-267, 2001.

8. T. Nordstrand and L.A. Carlsson, "Evaluation of Transverse Shear Stiffness of Structural Core Sandwich Plates", Composite Structures, Vol. 37, pp. 145-153, 1997.

9. SAS Institute Inc., 100 SAS Campus DriveCary, NC 27513-2414, USA.

10. P. Patel, T. Nordstrand, L. A. Carlsson, "Local buckling and collapse of corrugated board under biaxial stress", Composite Structures, Vol. 39, pp. 93-110, 1997.

11. T. Nordstrand, "On Buckling Loads for Edge Loaded Orthotropic Plates including Transverse Shear"*,* To be submitted to Composite Structures.

12. T. Nordstrand, "Parametrical Study of the Post-buckling Strength of Structural Core Sandwich Panels", Composite Structures, Vol. 30, pp. 441-451, 1995.

APPENDIX

Marquerre's differential equation linking in-plane stresses with out-of-plane displacements for orthotropic plates is as follows

$$\frac{1}{E_{22}^*}\frac{\partial^4 F}{\partial x^4} + \left(\frac{1}{G_{12}^*} - \frac{2v_{12}^*}{E_{11}^*}\right)\frac{\partial^4 F}{\partial x^2 \partial y^2} + \frac{1}{E_{11}^*}\frac{\partial^4 F}{\partial y^4} =$$

$$= \left(\frac{\partial^2 w}{\partial x \partial y}\right)^2 - \frac{\partial^2 w}{\partial x^2}\frac{\partial^2 w}{\partial y^2} - \left[\left(\frac{\partial^2 w_0}{\partial x \partial y}\right)^2 - \frac{\partial^2 w_0}{\partial x^2}\frac{\partial^2 w_0}{\partial y^2}\right] \tag{1}$$

If the deflections w and w_0 are of the same form and their magnitudes are related by the expression

$$w = A\overline{X}(x)\cos\left(\frac{\pi y}{b}\right) \tag{2}$$

and the initial imperfections as

$$w_0 = A_0 \overline{X}(x)\cos\left(\frac{\pi y}{b}\right) \tag{3}$$

then a solution of eq. (1) for a plate with uniform compressive displacements of its ends, as shown in Fig. 4, is

$$F = F_1(x) + F_2(x)\cos\left(\frac{2\pi y}{b}\right) \tag{4}$$

Substituting eqs. (2-4) into (1) gives

$$\frac{1}{E_{22}^*}F_1^{IV} = \frac{1}{2}\left(\frac{\pi}{b}\right)^2 \left(A^2 - A_0^2\right)\left[\overline{XX}^{II} + \left(\overline{X}^I\right)^2\right] \tag{5}$$

$$\frac{1}{E_{22}^*}F_2^{IV} - \left(\frac{2\pi}{b}\right)^2 HF_2^{II} + \left(\frac{2\pi}{b}\right)^4 \frac{1}{E_{11}^*}F_2 =$$

$$\frac{1}{2}\left(\frac{\pi}{b}\right)^2 \left(A^2 - A_0^2\right)\left[\overline{XX}^{II} - \left(\overline{X}^I\right)^2\right] \tag{6}$$

where $\quad H = \frac{1}{G_{12}^*} - \frac{2v_{12}^*}{E_{11}^*}$.

Thus F_1 is independent of y and hence constant along the length of the plate. While F_1 can not give a stress in the x-direction, it does give a stress in the y-direction which is found by integrating equation (5) twice.

This gives

$$F_1'' = \frac{E_{22}^*}{2}\left(\frac{\pi}{b}\right)^2\left(A^2 - A_0^2\right)\frac{\overline{X}^2}{2} + Bx + C \tag{7}$$

where B and C are constants and found from the membrane boundary conditions on the loaded ends.

To obtain an expression for F_2 we assume that the deflections across the plate are in the form of a polynomial series

$$\overline{X} = \sum_{n=1}^{N} A_n X_n \tag{8}$$

where $|A_n| \leq 1$ is the relative amplitude of the normalised shape function X_n which in turn is assumed to take the general algebraic form

$$X_n = \sum_{p=1}^{r} C_{pn}\left(\frac{x}{a}\right)^p \tag{9}$$

Substituting eq. (8) into eq. (6) gives

$$\frac{1}{E_{22}^*}F_2''' - \left(\frac{2\pi}{b}\right)^2 HF_2'' + \left(\frac{2\pi}{b}\right)^4\frac{1}{E_{11}^*}F_2 =$$

$$\frac{1}{2}\left(\frac{\pi}{b}\right)^2\left(A^2 - A_0^2\right)\sum_{n=1}^{N}\sum_{m=1}^{N}A_n A_m\left(X_n X_m'' - X_n' X_m'\right) \tag{10}$$

Inserting the expression for X_n, eq. (9), into eq. (10) and manipulating gives

$$\frac{1}{E_{22}^*}F_2''' - \left(\frac{2\pi}{b}\right)^2 HF_2'' + \left(\frac{2\pi}{b}\right)^4\frac{1}{E_{11}^*}F_2 =$$

$$\frac{1}{2}\left(\frac{\pi}{b}\right)^2\left(A^2 - A_0^2\right)\sum_{n=1}^{N}\sum_{m=1}^{N}A_n A_m \sum_{s=0}^{2(r-1)}B_{smn}\left(\frac{x}{a}\right)^s \tag{11}$$

where

$$B_{smn} = \sum_{q=1}^{r}C_{(s+2-q)n}C_{qm}\left[q(q-1) - q(s+2-q)\right] \tag{12}$$

A2

under the condition that $C_{(s+2-q<1)n} = C_{(s+2-q>r)n} = 0$. A solution for F_2 can be found by putting F_2 in the same form as the right hand side of eq. (11),

$$F_2 = \frac{1}{2a^2}\left(\frac{\pi}{b}\right)^2\left(A^2 - A_0^2\right)\sum_{n=1}^{N}\sum_{m=1}^{N} A_n A_m \phi_{mn}(x) E_{11}^* b^4 \tag{13}$$

Substituting eq. (13) into eq. (11) gives

$$\frac{1}{E_{22}^*}\phi_{mn}^{IV} - \left(\frac{2\pi}{b}\right)^2 H\phi_{mn}^{II} + \left(\frac{2\pi}{b}\right)^4 \frac{1}{E_{11}^*}\phi_{mn} = \sum_{s=0}^{2(r-1)} \frac{B_{smn}}{E_{11}^* b^4}\left(\frac{x}{a}\right)^s \tag{14}$$

If $\phi_{mn,part}$ in turn is assumed to take the same form as the right-hand side of Eq. (14),

$$\phi_{mn,part} = \sum_{s=0}^{2(r-1)} L_{smn}\left(\frac{x}{a}\right)^s \tag{15}$$

we obtain, by substituting eq. (15) into eq. (14) and equating coefficients from each term, for $s = 2(r-1)$ to $2(r-1)-1$

$$L_{smn} = \frac{B_{smn}}{(2\pi)^4} \tag{16}$$

and for $s = 2(r-2)$ to $2(r-1)-3$

$$L_{smn} = \frac{B_{smn}}{(2\pi)^4} + \frac{H(s+1)(s+2)}{\dfrac{1}{E_{11}^*}\left(\dfrac{2\pi}{b}\right)^2 a^2} L_{(s+2)mn} \tag{17}$$

and for $0 \le s \le 2(r-1)$

$$L_{smn} = \frac{B_{smn}}{(2\pi)^4} + \frac{H(s+1)(s+2)}{\dfrac{1}{E_{11}^*}\left(\dfrac{2\pi}{b}\right)^2 a^2} L_{(s+2)mn} -$$

$$-\frac{\dfrac{1}{E_{22}^*}(s+1)(s+2)(s+3)(s+4)}{\dfrac{1}{E_{11}^*}\left(\dfrac{2\pi}{b}\right)^4 a^4} L_{(s+4)mn} \tag{18}$$

Eqs. (16) - (18) thus give the particular integral solution for eq. (14) when evaluated in the right order. To obtain a complete solution for ϕ, the complementary function solution must be added to eq. (15). There are three possible solutions to the homogeneous equation,

$$\phi_{mn}^{IV} - \left(\frac{2\pi}{b}\right)^2 E_{22}^* H\phi_{mn}^{II} + \left(\frac{2\pi}{b}\right)^4 \frac{E_{22}^*}{E_{11}^*}\phi_{mn} = 0 \tag{19}$$

consistent with the values of E_{11}^*, E_{22}^* and H.

A3

1. If $E_{22}^{*}{}^{2}H^{2} > 4\dfrac{E_{22}^{*}}{E_{11}^{*}}$, then all roots are real.

2. If $E_{22}^{*}{}^{2}H^{2} = 4\dfrac{E_{22}^{*}}{E_{11}^{*}}$, then the roots are equal. This corresponds to the isotropic case.

3. If $E_{22}^{*}{}^{2}H^{2} < 4\dfrac{E_{22}^{*}}{E_{11}^{*}}$, then all roots are complex.

Only the first of these conditions is dealt with since this is consistent with the class of materials considered. Thus the solution to equation (19) is

$$\phi_{mn,\text{hom}} = C_{1mn}\cosh k_{1}x + C_{2mn}\sinh k_{1}x + C_{3mn}\cosh k_{2}x + C_{4mn}\sinh k_{2}x \qquad (20)$$

where

$$k_{1} = \left[\left(\frac{2\pi}{b}\right)^{2}\frac{1}{2}\left(E_{22}^{*}H + \sqrt{E_{22}^{*}{}^{2}H^{2} - 4\frac{E_{22}^{*}}{E_{11}^{*}}}\right)\right]^{\frac{1}{2}} \qquad (21a)$$

and

$$k_{2} = \left[\left(\frac{2\pi}{b}\right)^{2}\frac{1}{2}\left(E_{22}^{*}H - \sqrt{E_{22}^{*}{}^{2}H^{2} - 4\frac{E_{22}^{*}}{E_{11}^{*}}}\right)\right]^{\frac{1}{2}} \qquad (21b)$$

The complete solution for ϕ_{mn} is

$$\phi_{mn} = \sum_{s=0}^{2(r-1)} L_{smn}\left(\frac{x}{a}\right)^{s} + C_{1mn}\cosh k_{1}x + C_{2mn}\sinh k_{1}x + $$
$$+ C_{3mn}\cosh k_{2}x + C_{4mn}\sinh k_{2}x \qquad (22)$$

The values of the constants C_{imn} are obtained by considering the boundary conditions at $x=0$ and $x=a$. It can be shown that if the unloaded edges are free to move in the plane of the plate, the shear stress τ_{xy} and the stress normal to the edge σ_{x} must be 0.

Since $\sigma_{x} = \dfrac{\partial^{2}F}{\partial y^{2}}$ and $\tau_{xy} = -\dfrac{\partial^{2}F}{\partial x\partial y}$, it follows by substituting eq. (13) into eq. (4) and differentiate eq. (4) accordingly that

$$\phi_{mn}(0) = 0;\ \phi_{mn}(a) = 0;\ \phi_{mn}{}'(0) = 0;\ \phi_{mn}{}'(a) = 0 \qquad (23)$$

The constants are thus found to be

$$C_{1mn} = \frac{k_{1}T_{3}\left(T_{1mn} + T_{6mn}\right) - T_{4}\left(T_{2mn} + T_{7mn}\right)}{T_{4}T_{5} - k_{1}T_{3}^{2}}$$

$$C_{2mn} = -\frac{T_{5}\left(T_{1mn} + T_{6mn}\right) - T_{3}\left(T_{2mn} + T_{7mn}\right)}{T_{4}T_{5} - k_{1}T_{3}^{2}} \qquad (24)$$

$$C_{3mn} = -C_{1mn} - L_{0mn}$$

A4

$$C_{4mn} = -\frac{k_1}{k_2}C_{1mn} - \frac{L_{1mn}}{k_2 a}$$

where

$$T_{1mn} = \sum_{s=0}^{2(r-1)} L_{smn}$$

$$T_{2mn} = \sum_{s=0}^{2(r-1)-1} \frac{L_{(s+1)mn}}{a}(s+1)$$

$$T_3 = \cosh(k_1 a) - \cosh(k_2 a)$$

$$T_4 = \sinh(k_1 a) - \frac{k_1}{k_2}\sinh(k_2 a)$$

$$T_5 = k_1 \sinh(k_1 a) - k_2 \sinh(k_2 a)$$

$$T_{6mn} = -L_{0mn}\cosh(k_2 a) - \frac{L_{1mn}}{k_2 b}\sinh(k_2 a)$$

$$T_{7mn} = -L_{0mn}k_2 \sinh(k_2 a) - \frac{L_{1mn}}{b}\cosh(k_2 a)$$

The stress function F is completely determined in terms of the deflection given by eqs. (2) and (3). The constants in eq. (7) are found by compressing the plate uniformly along the loaded edges an amount $v = -\Delta$, see Fig. 4. During compression of the plate, it is assumed that no shear stresses are introduced along the loaded edges.

Thus $\tau_{xy} = 0$ when $y = -\frac{b}{2}$ and $y = \frac{b}{2}$ and the compressive displacement must be

$$v = \int_{-\frac{b}{2}}^{\frac{b}{2}}\left[\varepsilon_y - \frac{1}{2}\left(\frac{\partial w}{\partial y}\right)^2 + \frac{1}{2}\left(\frac{\partial w_0}{\partial y}\right)^2\right]dy \qquad (25)$$

From Hooke's law we obtain

$$\varepsilon_y = \frac{1}{E_{22}^*}\sigma_y - \frac{v_{21}}{E_{22}^*}\sigma_x \qquad (26)$$

and if

$$\sigma_x = \frac{\partial^2 F}{\partial y^2}; \ \sigma_y = \frac{\partial^2 F}{\partial x^2} \qquad (27)$$

a combination of equations (25) - (27) gives

$$v = \int_{-\frac{b}{2}}^{\frac{b}{2}}\left[\frac{1}{E_{22}^*}\left(\frac{\partial^2 F}{\partial x^2} - v_{21}\frac{\partial^2 F}{\partial y^2}\right) - \frac{1}{2}\left(\frac{\partial w}{\partial y}\right)^2 + \frac{1}{2}\left(\frac{\partial w_0}{\partial y}\right)^2\right]dy \qquad (28)$$

Substituting for F, w and w_0 and integrating eq. (28), F_1^{II} is found to be

$$F_1'' = E_{22}^* \frac{v}{b} + \frac{E_{22}^*}{4}\left(\frac{\pi}{b}\right)^2 \left(A^2 - A_0^{\ 2}\right)\overline{X}^2 \tag{29}$$

Substituting eq. (7) into eq. (29) gives

$$v = \frac{b}{E_{22}^*}\left(Bx + C\right) \tag{30}$$

To obtain uniform end displacement across the plate, B must be zero and the remaining coefficient will be

$$C = E_{22}^* \frac{v}{b} \tag{31}$$

which is the stress induced in an unbuckled plate by the compression v.

The strain energy in the buckled plate consists of two parts: the potential energy of bending and twisting, V_B, and the membrane stretch energy, V_M:

$$V_B = \frac{1}{2}\int_0^a \int_{-\frac{b}{2}}^{\frac{b}{2}} \left[D_{11}\left(\frac{\partial^2}{\partial x^2}(w-w_0)\right)^2 + 2D_{11}\nu_{21}\left(\frac{\partial^2}{\partial x^2}(w-w_0)\right)\left(\frac{\partial^2}{\partial y^2}(w-w_0)\right) + \right.$$

$$\left. + D_{22}\left(\frac{\partial^2}{\partial y^2}(w-w_0)\right)^2 + 4D_{66}\left(\frac{\partial^2}{\partial x\partial y}(w-w_0)\right)^2 \right] dy\,dx \tag{32}$$

$$V_M = \frac{h}{2}\int_0^a \int_{-\frac{b}{2}}^{\frac{b}{2}} \left[\frac{1}{E_{11}^*}\left(\frac{\partial^2 F}{\partial y^2}\right)^2 - \frac{2\nu_{12}^*}{E_{11}^*}\left(\frac{\partial^2 F}{\partial y^2}\frac{\partial^2 F}{\partial x^2}\right) + \right.$$

$$\left. + \frac{1}{G_{12}^*}\left(\frac{\partial^2 F}{\partial x\partial y}\right)^2 + \frac{1}{E_{22}^*}\left(\frac{\partial^2 F}{\partial x^2}\right)^2 \right] dy\,dx \tag{33}$$

Substituting the derivatives of F and w using eqs. (2) - (4), (8), (13) and (29) in eqs. (32) - (33) and integrating with respect to y gives

$$V_B = \left(A - A_0\right)^2 \frac{b}{4}\left\{ \int_0^a \left[D_{11}\sum_{n=1}^N \sum_{m=1}^N A_n A_m X_n{}'' X_m{}'' - \right. \right.$$

$$- \left(\frac{\pi}{b}\right)^2 \nu_{21}D_{11}\sum_{n=1}^N \sum_{m=1}^N A_n A_m X_n X_m{}'' +$$

$$\left. \left. + \left(\frac{\pi}{b}\right)^4 D_{22}\sum_{n=1}^N \sum_{m=1}^N A_n A_m X_n X_m + 4\left(\frac{\pi}{b}\right)^2 D_{66}\sum_{n=1}^N \sum_{m=1}^N A_n A_m X_n{}' X_m{}' \right] dx \right\} \tag{34}$$

A6

$$V_M = \frac{bh}{4}\left\{\left(A^2 - A_0^2\right)^2 \int_0^a \left[\left(\frac{\pi}{b}\right)^4 \frac{E_{22}^*}{8} \sum_{n=1}^N \sum_{m=1}^N \sum_{p=1}^N \sum_{q=1}^N A_n A_m A_p A_q X_n X_m X_p X_q + \right.\right.$$

$$+\left(\frac{\pi}{b}\right)^4 \frac{E_{11}^{*2} b^8}{4E_{22}^* a^4} \sum_{n=1}^N \sum_{m=1}^N \sum_{p=1}^N \sum_{q=1}^N A_n A_m A_p A_q \phi_{mn}^{\;II} \phi_{pq}^{\;II} +$$

$$+\left(\frac{2\pi}{b}\right)^4 \left(\frac{\pi}{b}\right)^4 \frac{E_{11}^* b^8}{4a^4} \sum_{n=1}^N \sum_{m=1}^N \sum_{p=1}^N \sum_{q=1}^N A_n A_m A_p A_q \phi_{mn} \phi_{pq} +$$

$$+\left(\frac{2\pi}{b}\right)^2 \left(\frac{\pi}{b}\right)^4 \frac{v_{12}^* E_{11}^* b^8}{2a^4} \sum_{n=1}^N \sum_{m=1}^N \sum_{p=1}^N \sum_{q=1}^N A_n A_m A_p A_q \phi_{mn} \phi_{pq}^{\;II} +$$

$$\left.\left.+\left(\frac{2\pi}{b}\right)^2 \left(\frac{\pi}{b}\right)^4 \frac{E_{11}^{*2} b^8}{4G_{12}^* a^4} \sum_{n=1}^N \sum_{m=1}^N \sum_{p=1}^N \sum_{q=1}^N A_n A_m A_p A_q \phi_{mn}^{\;I} \phi_{pq}^{\;I}\right] dx + \right.$$

$$\left.+2E_{22}^*\left(\frac{v}{b}\right)^2 \int_0^a dx \right\} + \left(A^2 - A_0^2\right)\left(\frac{\pi}{b}\right)^2 \frac{bh}{4} E_{22}^*\left(\frac{v}{b}\right) \int_0^a \sum_{n=1}^N \sum_{m=1}^N A_n A_m X_n X_m dy \qquad (35)$$

The total strain energy is obtained by adding V_B and V_M,

$$V = V_B + V_M \qquad (36)$$

In order to minimise this expression with respect to A we have to know the values of A_i, $i=1..N$, i.e. the relative amplitudes of the shape functions. Assuming that the imperfect plate will have the same deflected shape as a perfect plate, with $A_0 = 0$, we can obtain an accurate description of A_i by the first buckling mode. Initially, limited bending can be produced with negligible membrane stretching of the middle plane, and we need to consider only the bending energy and the corresponding work done by the external forces acting in the middle plane of the plate, i.e. all terms that include v in eq. (35). Subsequently, all terms in eq. (36) that contain the fourth power of A_i can be omitted. Thus equation (36) can be written as

$$V = \frac{bA^2}{4} \sum_{n=1}^N \sum_{m=1}^N A_n A_m \left\{\int_0^a \left[D_{11} X_n^{\;II} X_m^{\;II} - 2\left(\frac{\pi}{b}\right)^2 v_{21} D_{11} X_n X_m^{\;II} + \right.\right.$$

$$\left.\left.+4\left(\frac{\pi}{b}\right)^2 D_{66} X_n^{\;I} X_m^{\;I} + \left(\frac{\pi}{b}\right)^4 D_{22} X_n X_m + \left(\frac{\pi}{b}\right)^2 E_{22}^* h\left(\frac{v}{b}\right) X_n X_m\right] dy\right\} + abh \frac{E_{22}^*}{2}\left(\frac{v}{b}\right)^2 \quad (37)$$

The minimum of V is found by differentiating V with respect to A_i and using

$$dV = \frac{\partial V}{\partial A_1} dA_1 + \frac{\partial V}{\partial A_2} dA_2 + \ldots\ldots + \frac{\partial V}{\partial A_n} dA_n = 0 \qquad (38)$$

which in turn gives N linear simultaneous equations, from which the value of $v = -\Delta_{crit}$ to cause buckling can be found. The relative values of A_i can also be obtained. Thus

A7

$$S_{nm} = \int_0^a \left[D_{11} X_n{}^{II} X_m{}^{II} - \left(\frac{\pi}{b}\right)^2 v_{21} D_{11} X_n X_m{}^{II} + 4\left(\frac{\pi}{b}\right)^2 D_{66} X_n{}^I X_m{}^I + \left(\frac{\pi}{b}\right)^4 D_{22} X_n X_m \right] dx$$

(39)

$$Q_{nm} = \int_0^a \left[\left(\frac{\pi}{b}\right)^2 E_{22}^* \frac{h}{b} X_n X_m \right] dx$$

gives

$$\left[\overline{\overline{S}} + \overline{\overline{S}}^T - 2\Delta_{crit} \overline{\overline{Q}} \right] \overline{A} = \overline{0}$$

(40)

and the non-trivial solution of eq. (42) demands that

$$\left| \overline{\overline{S}} + \overline{\overline{S}}^T - 2\Delta_{crit} \overline{\overline{Q}} \right| = 0$$

(41)

Solving eq. (41) for Δ_{crit} and inserting the value of Δ_{crit} in eq. (40) enable us to obtain the normalised eigenvector $\overline{A}$. Thus all A_i:s are determined.

Inserting the values of A_i in equation (36) and minimising V with respect to A yields the relationship between A and v as follows:

$$v = -\left(1 - \frac{A_0}{A}\right)\frac{C_2}{C_1} - \left(A^2 - A_0{}^2\right)\frac{C_3}{C_1}$$

(42)

where

$$C_1 = \left(\frac{\pi}{b}\right)^2 \frac{E_{22}^* h}{8} \sum_{n=1}^{N} \sum_{m=1}^{N} A_n A_m \int_0^a X_n X_m \, dy$$

(43)

$$C_2 = \frac{b}{8} \sum_{n=1}^{N} \sum_{m=1}^{N} A_n A_m \left\{ \int_0^a \left[D_{11} X_n{}^{II} X_m{}^{II} - \left(\frac{\pi}{b}\right)^2 v_{21} D_{11} X_n X_m{}^{II} + \right. \right.$$
$$\left. \left. + 4\left(\frac{\pi}{b}\right)^2 D_{66} X_n{}^I X_m{}^I + \left(\frac{\pi}{b}\right)^4 D_{22} X_n X_m \right] dy \right\}$$

(44)

$$C_3 = \left(\frac{\pi}{b}\right)^4 \frac{bh}{4} \sum_{n=1}^{N} \sum_{m=1}^{N} \sum_{p=1}^{N} \sum_{q=1}^{N} A_n A_m A_p A_q \left\{ \int_0^a \left[\frac{E_{22}^*}{8} X_n X_m X_p X_q + \right. \right.$$
$$\left. + \frac{E_{11}^{*2} b^8}{4a^4} \left[\frac{1}{E_{22}^*} \phi_{mn}{}'' \phi_{pq}{}'' + \left(\frac{2\pi}{b}\right)^2 \left[\frac{2v_{12}^*}{E_{11}^*} \phi_{mn} \phi_{pq}{}'' + \frac{1}{G_{12}^*} \phi_{mn}{}' \phi_{pq}{}' + \right. \right.$$
$$\left. \left. \left. + \left(\frac{2\pi}{b}\right)^2 \frac{1}{E_{11}^*} \phi_{mn} \phi_{pq} \right] \right] \right] dx \right\}$$

(45)

Paper 6

———

Local Buckling and Collapse of Corrugated Board under Biaxial Stress

by

P. Patel, Nordstrand, T. and Carlsson, L.A.

Local buckling and collapse of corrugated board under biaxial stress

Poorvi Patel[a], Tomas Nordstrand[a], Leif A. Carlsson[b]

[a]*SCA Research, Box 3054, 850 03 Sundsvall, Sweden*
[b]*Department of Mechanical Engineering, Florida Atlantic University, Boca Raton, FL 33431, USA*

The collapse mechanism of biaxially loaded corrugated board cylinders with the corrugations parallel to the cylinder axis has been experimentally examined. Axial compression, torque, external pressure and combinations thereof were examined. The cylinder dimensions were sized to avoid global buckling prior to failure of the material using finite element analysis (FE). Failure analysis of the board was based on the stress state in the facings in conjunction with a combined stress failure criterion (Tsai–Wu quadratic criterion). For cylinders under compression parallel to the corrugations, local buckling was observed but did not influence the collapse load. For biaxial load cases involving substantial shear and compression perpendicular to the corrugations, the experimental collapse stresses were substantially below predictions based on stresses in the facings in conjunction with the failure criterion. Such a discrepancy is explained by the tendency of the facings to buckle locally before material failure. Consequently, local buckling appears to govern failure of corrugated board when there are large transverse normal and shear stresses acting. © 1997 Elsevier Science Ltd.
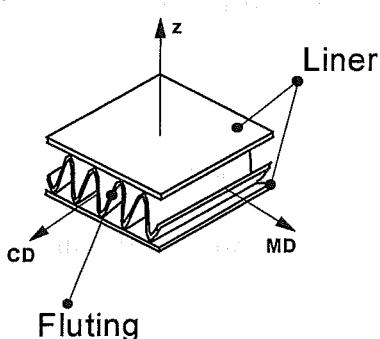
Fig. 1. Single wall corrugated board and its principal directions.

INTRODUCTION

Corrugated board (Fig. 1) is a sandwich structure used in a wide variety of packaging applications [1]. Corrugated board is an orthotropic sandwich with the surface plies (facings) providing bending stiffness, separated by a lightweight corrugated core (fluting) that provides shear stiffness. The principal directions of elastic symmetry are defined as those of the paper constituents, i.e. the machine direction (MD), cross direction (CD) and thickness direction (z) (Fig. 1). The facings of the corrugated board are commonly denoted as 'liners'. Structural design of a corrugated board package is currently based on empirical methods that require manufacture of the board and package and strength tests of the actual package. This paper aims to assist the process of bringing in appropriate engineering principles in the structural design.

It has long been recognized that corrugated board panels loaded in compression display local buckling of the facings between the corrugations [2–5] (Fig. 2). Local buckling and failure of such a panel has been found to initiate in the facing in regions where the facings are under high shear and compressive stresses [4,5]. Local buckling thus appears to be an important failure mechanism of corrugated board. To the knowledge of the authors, very few studies of local buckling instability of corrugated board have been published [2,3,6–8].
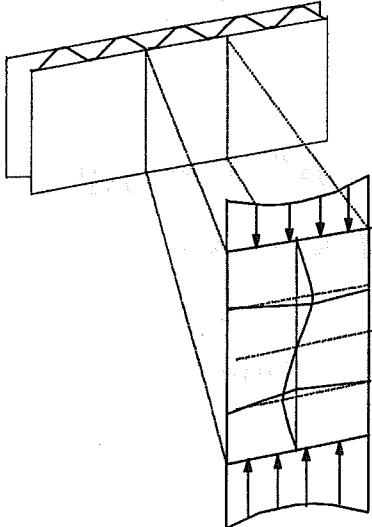
Fig. 2. Local buckling of corrugated board.

Johnson & Urbanik [2,3] analyzed local buckling instability of flat plates under axial compression. Anderson [6] and Zahn [7]investigated compressive buckling coefficients for local buckling of single- and double truss cores. Starlinger [8] developed a finite element formulation for analysis of honeycomb and foam core sandwich shells addressing global and local instabilities. Analysis of the stress conditions when local buckling is deteriorating the load-bearing capability of corrugated board panels is complicated by the many imperfections present in the material. Improved analysis methods thus require experimental back-up which is the objective of this study.

A wide range of combined uniform stress states is most conveniently achieved by subjecting cylinders to axial load, torque and external pressure. An initial experimental study of the failure mechanism of corrugated board loaded in pure axial compression along the corrugations and combined axial compression and torsion is presented by the authors in Ref. 9. The relatively low torque capacity of the test frame used in that study, however, does not allow application of large shear stress and the results are limited to compression dominated loading. In the present study, a larger variety of biaxial fields are considered. Cylinders were subjected to pure torsion using a specially developed torque fixture. A system for applying external pressure was also developed. In parallel to the experimental studies, analysis of local buckling and failure of the facings was performed using finite element analysis (FEA).

Experimental and analytical results are compared.

STRESS ANALYSIS OF CORRUGATED BOARD CYLINDERS

Local buckling and collapse of corrugated board cylinders loaded in axial compression, torsion and external pressure and combinations thereof are examined herein. To relate the axial load, external pressure and torque applied to the stresses in the facings of the board, a simplified stress analysis was performed. Through this analysis, the local buckling and collapse stresses in the facings may easily be established. The analysis is subsequently compared with stresses obtained from detailed finite element stress analysis.

Coordinate system and loading conditions

A global cylindrical coordinate system $(r-\phi-z)$ was assigned to the cylinder, and a local Cartesian system $(x-y-z)$ to the cylinder wall (Fig. 3). The radial direction of the cylinder coincides with the thickness coordinate of the board. The machine direction (MD) of the board is along the hoop direction of the cylinder and the cross direction (CD) of the board is aligned with the cylinder axis (Fig. 3). The axial force, F, corresponds to normal stress, σ_y, and the torque, T, to shear stress, τ_{xy}. Hoop stress, σ_x, is achieved by internally or externally pressurizing the cylinder.

Approximate stress analysis

Normal stresses, σ_y and σ_x, and shear stress, τ_{xy}, in the facings are calculated as functions of
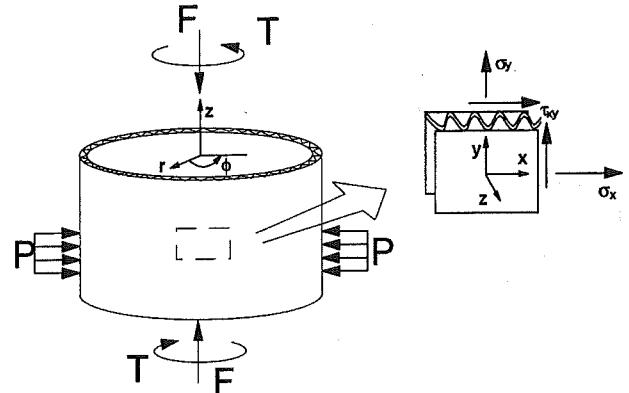
Fig. 3. Coordinate systems and loading of the cylinder.

torque, T, axial force, F, and pressure, P. The corrugated board is considered symmetric, i.e. the facings are assumed to be identical. Further, the board is assumed to be under uniform strain (equal in-plane strains in both facings and core).

The axial force per unit width of an axially compressed cylinder may be expressed as

$$f = \frac{F}{2\pi R} \tag{1}$$

where F is the load applied, and R is the mean radius. Equilibrium in the axial direction requires (Fig. 4)

$$f = 2t_L \sigma_y L + \alpha \sigma_y C t_C \tag{2}$$

where t_L and t_C are the facing (liner) and fluting thicknesses, and σ_{yL} and σ_{yC} are normal stresses in the facings (L) and core (C);

$$\sigma_y L = E_y L \varepsilon_y L \tag{3a}$$

$$\sigma_y C = E_y C \varepsilon_y C \tag{3b}$$

where E_{yL} and E_{yC} are the Young's moduli of the facing and core in the CD, and ε_{yL} and ε_{yC} are the strains in the facings and core. Assuming uniform strain, $\varepsilon_{yC} = \varepsilon_{yL}$ in Eqs. yields

$$\sigma_y C = \frac{E_y C}{E_y L} \sigma_y L \tag{4}$$

Substitution of eqns (2) and (4) in eqn (1) gives

$$\sigma_y L = \frac{F}{2\pi R \left(2t_L + \alpha \dfrac{E_y C}{E_y L} t_C \right)} \tag{5}$$
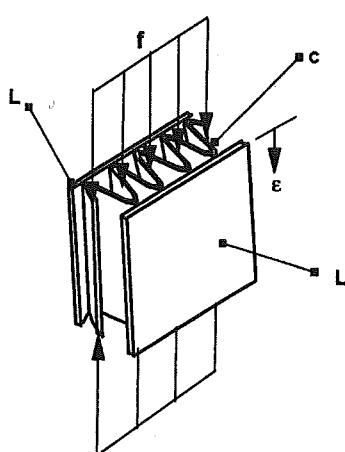
Fig. 4. Corrugated board element under axial load.

For a cylinder under external pressure, P, the stresses σ_x and σ_y in the facings are

$$\sigma_x = \frac{PR}{2t_L} \tag{6a}$$

$$\sigma_y = \frac{PA}{\pi 2R \left(2t_L + \alpha \dfrac{E_y C}{E_y L} t_C \right)} \tag{6b}$$

the subscript L on the stress is dropped from now on. A is the area of the end caps. The corrugated core is assumed not to carry hoop stress, σ_x, in Eqs. , but the core contributes to the axial force, eqn (6b).

For a torqued cylinder, the shear stress in the facings is

$$\tau_{xy} = \frac{T}{4\pi R^2 t_L} \tag{7}$$

where T is the torque applied. The contribution of the corrugated core to the torque is small compared with that from the faces [10] and is therefore neglected.

Tsai–Wu failure criterion

Failure prediction of the corrugated board under combined loading is performed based on the one hypothesis that the board fails when the stresses in the facings reach their ultimate combination. This assumption neglects possible reduction of the failure stress in the facings caused by local buckling. For anisotropic materials such as paper, the Tsai–Wu failure criterion [11] is commonly applied [12,13]. For plane stress (σ_x, σ_y and τ_{xy}) the Tsai–Wu criterion [11] is

$$F_1\sigma_x + F_2\sigma_y + F_{11}\sigma_x^2 + F_{22}\sigma_y^2 + F_{66}\tau_{xy}^2 + 2F_{12}\sigma_x\sigma_y = 1 \tag{8}$$

Equation (8) describes an ellipsoid in a space spanned by the stresses σ_x, σ_y, and τ_{xy} where all stress states on or outside the surface of the ellipsoid indicate failure. The parameters F_i and F_{ij} in eqn (8) are related to the tension and compression strengths in the x and y directions, and the shear strength in xy plane as follows

$$F_1 = \frac{1}{X_x^T} - \frac{1}{X_x^C} \quad F_{11} = \frac{1}{X_x^T X_x^C} \tag{9a}$$

$$F_1 = \frac{1}{X_y^T} - \frac{1}{X_y^C} \quad F_{22} = \frac{1}{X_y^T X_y^C} \qquad (9b)$$

$$F_{66} = \frac{1}{S_{xy}^2} \qquad (9c)$$

where X represents tension and compression strengths and superscripts T and C indicate tension and compression. Subscripts x and y denote the coordinate directions, and S_{xy} is the inplane shear strength. For paper, F_{12} and S_{xy} are approximated as [13]:

$$F_{12} \approx -0.36\sqrt{F_{11}F_{22}} \qquad (10)$$

and

$$S_{xy} \approx \sqrt{X_x^C X_y^C} \qquad (11)$$

Tsai–Wu factor

The left hand side of eqn (8) at any stress state is herein denoted the 'Tsai–Wu factor', k, thus:

$$k = F_1\sigma_x + F_2\sigma_y + F_{11}\sigma_x^2 + F_{22}\sigma_y^2 + F_{66}\tau_{xy}^2 + 2F_{12}\sigma_x\sigma_y \qquad (12)$$

If

$k < 1$ material failure has not yet initiated

$k \geq 1$ material failure has initiated.   (13)

The Tsai–Wu factor is used to localize the failure initiation region of the cylinder at different load combinations from contour plots of k over the cylinder surface as obtained from FE

analysis. Regions where k is maximum are thus expected to fail first.

Board specifics

The board considered in the previous study [9] was further examined. The board consists of a 200 g/m^2 outer facing made from kraft liner coated with a 25 g/m^2 polyethylene (PE) film barrier on the outside, an inner facing of 186 g/m^2 kraft liner, separated by a 150 g/m^2 corrugated semichemical fluting core. The wavelength of the fluting is 7·2 mm and the core height is 3·6 mm corresponding to a 'C-type' flute. The geometry and material properties of the board are listed in Tables 1 and 2. The effective core properties listed in Table 2 are homogenized properties obtained as explained in Ref. 9 for subsequent use in the FE analysis of buckling and collapse.

BUCKLING ANALYSIS OF CYLINDRICAL TEST SPECIMEN

Cylinder specimens were manufactured and subjected to combinations of compressive force, torque and external pressure as schematically

Table 1. Geometry parameters of the corrugated board examined

	mm
t_o	0·266
t_i	0·231
t_c	0·252
t_f	3·6
λ	7·2

t_o, t_i and t_c are the thicknesses of the outer, inner facings and fluting, respectively; t_f is the flute height and λ is the flute wavelength.

Table 2. Material properties of the board constituents (at 23°C and 50% RH)

	Outer liner	Fluting	Inner liner	Effect. core prop.*
E_x (MPa)	8510	5270	8220	0·5
E_y (MPa)	3810	2260	3010	227
G_{xy} (MPa)	2200	1340	1920	0·23
G_{xz} (MPa)	45	45	45	3·5
G_{yz} (MPa)	45	45	45	35
v_{xy}	0·17	0·17	0·17	0·004
SCT$_x$ (kN/m)	8·6	—	7·0	—
SCT$_y$ (kN/m)	5·4	—	3·8	—

*Effective core properties for use in FE-analysis (core is considered homogeneous).
E_x and E_y are the in-plane Young's moduli, G_{xy}, G_{xz}, G_{yz} are the shear moduli, v_{xy} is the in-plane (major) Poisson's ratio, and SCT$_x$, SCT$_y$ are the compression strengths (load per unit width) in the MD and CD. The CD compression strength of the board (ECT) is 11.3 kN/m.

Table 3. Axial load (*F*), torque (*T*) and pressure (*P*) at collapse calculated by FE and approximative stress analyses (MPa)

| Loading case	FEM			Approximate		
	F (kN)	*T* (Nm)	*P* (kPa)	*F* (kN)	*T* (Nm)	*P* (kPa)
Axial compression	−15·6	—	—	−16·1	—	—
Torsion	—	3450	—	—	3455	—
External pressure	−7·3	—	−37·4	− 7·3	—	−37·3

illustrated in Fig. 3. The cylinder manufacturing technique and details of the test frame are outlined in Ref. 9. Cylindrical shells are prone to imperfection sensitivity [14]. This implies that large factors of safety have to be implied in the design of such shells. Since the objective of this study was to examine collapse of the cylinder wall material under biaxial loading, the cylinders had to be designed to avoid global buckling. Thus, the cylinder dimensions should be sized properly. Analysis of compression and torsion loaded cylinders in Ref. 9 showed that the cylinder should have a diameter less than 1·6 m to avoid buckling failure. In this study, cylinders of 0·5 m diameter and 0·4 m length were considered. To examine the possibility of global buckling of the cylinders loaded in the various combinations of axial compression, torsion and external pressure considered in this study, further analysis was performed. FE models of the cylinder are described in detail in the previous study, Ref. 9. The FE code ANSYS [15] was used for this purpose. An eight-noded layered shell element (STIF99) was employed for modelling the board cylinder. The entire cylinder was modeled since the cylinder may not buckle symmetrically. The model consists of 1024 nodes (6 dof per node) and 320 elements. The end caps were not modeled in the buckling analysis. Boundary conditions were defined to represent the conditions of the tests, i.e. the ends were assumed to displace uniformly, and rotations of the ends were not allowed.

In order to examine the accuracy of the approximate stress analysis, the axial compression load, torque and external pressure at collapse of the cylinder were calculated from FE stress analysis and approximate stress analysis in conjunction with the Tsai–Wu failure criterion and compared. In this analysis, the FE model consists of a symmetry section of the cylinder, i.e. one end cap and half the cylinder (buckling was not considered). The calculated collapse load, torque and external pressure are listed in Table 3. Inspection of Table 3 reveals that the collapse load, torque and external pressure calculated from the approximate analysis are within 5% of those from the FE analysis, which shows that the approximate stress analysis is quite accurate.

Buckling analysis of torqued cylinder

The ends of the corrugated board cylinders are attached to end caps as shown schematically in Fig. 5. Torsion loading of the cylinder was achieved by application of a tangential force on each of the upper end nodes of the cylinder. Uniform displacement of the loaded end was guaranteed by coupling the end nodes to each other in axial and tangential translations. The lower end of the cylinder was considered clamped, i.e. all displacements and rotations were zero. An eigenvalue analysis of the torqued cylinder yields static load multipliers (SLMs) [15] corresponding to each buckling mode. The critical buckling torque, T_{cr}, is obtained by multiplying the smallest SLM with the total number of nodes on the loaded edge and the radius of the cylinder (T_{cr} = 64R SLM).
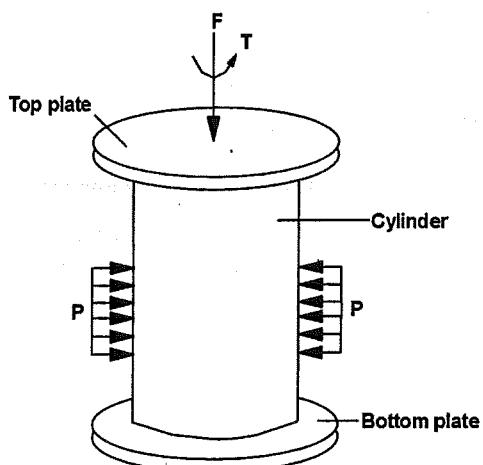
**Fig. 5.** Cylinder bonded to end caps.
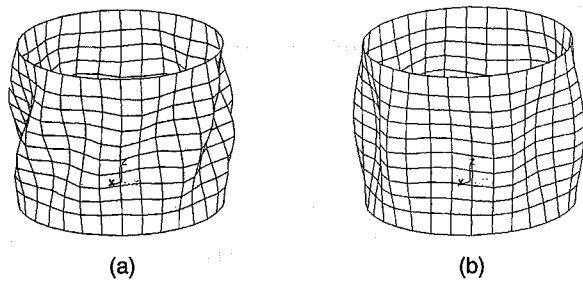
Fig. 6. (a) Buckled shape of a cylinder under torsion at $T = 9\cdot1$ kNm. (b) Buckled shape of a cylinder under external pressure at $P = -35\cdot6$ kPa.

FE analysis yielded a critical buckling torque of 9018 Nm, corresponding to a shear stress τ_{xy} of 46·2 MPa in the facings (eqn (7)). The buckling mode shape is illustrated in Fig. 6(a). The cylinder buckles in six wavelengths tangentially and in one wavelength axially. For comparison, the shear stress at failure of the facings was estimated from the approximate stress analysis in conjunction with the Tsai–Wu failure criterion (Eqs.). Table 4 lists buckling and failure stress predictions and the ratio between the buckling and failure stresses. It is observed that the critical buckling stress exceeds the failure stress by a factor of 2·4, which would indicate material failure prior to global buckling of the cylinder.

Buckling analysis of cylinder under external pressure

In the buckling analysis of an externally pressurized cylinder, surface pressure was applied on all the elements of the cylinder wall. Because the pressure also acts on the end caps of the cylinder, axial compression will develop:

$$F_{\text{plate}} = PA_{\text{plate}} \tag{14}$$

with A_{plate} being the area of the end caps (πR^2) and P the applied external pressure.

The FE analysis predicts that the cylinder will buckle in one half wavelength along its axis and six wavelengths circumferentially (Fig. 6(b)). The critical combination of buckling load and pressure is $F_{\text{plate}} = -7\cdot0$ kN and $P = -35\cdot6$ kPa (Table 4). Inspection of the stresses listed in Table 4 reveals that the ratio between the critical buckling stresses and failure stresses is 0·88, which indicates that global buckling occurs before the material of the cylinder wall fails. This analysis, however, does not include the possibility for local buckling of the board which will decrease the collapse stresses as will be discussed later.

Buckling analysis of biaxially loaded cylinders

Analysis of cylinders subjected to combined loading requires consideration of the manner in which axial compression load, torque and external pressure are applied. In this study the shear and normal stresses in the facings, τ_{xy}, σ_x and σ_y (Fig. 3), were proportionally increased. Expressions for the proportional constants are derived in Appendix A. The proportional constants that define the relation between the stresses are conveniently expressed in terms of 'phase angles', see Fig. 7. Certain phase angles were chosen for the various loading cases and used both in the experimental and analytical work. The phase angles selected and the calculated constants are listed in Table 5.

FE analysis of a cylinder subjected to combined compression and external pressure gave the following critical buckling stresses in the facings: $\sigma_y = -35\cdot8$ MPa and $\sigma_x = -12\cdot7$ MPa (Table 4). Comparison of these stresses with the calculated failure stresses in the facings, Table 4, reveals that the buckling stresses are more than twice the failure stresses which indicates that the cylinder will fail by material failure.

For a cylinder under torsion and external pressure, the calculated combination of torque,

Table 4. Buckling analysis results for cylinder with $R = 0.25$ m and $L = 0.4$ m

Loading case	Critical buckling load/torq./pressure (kN/kNm/kPa)	Buckling stresses (MPa) $\sigma_y/\tau_{xy}/\sigma_x$	Failure stresses* (MPa) $\sigma_y/\tau_{xy}/\sigma_x$	Buckling-to-failure stresses ratio
Torsion	.../9·1/...	.../46·2/...	.../19·2/...	2·4
External pressure	$-7\cdot0/.../-35\cdot6$	$-6\cdot0/.../-17\cdot9$	$-6\cdot87/.../-20\cdot4$	0·88
Comp./ext. pressure	$-41\cdot5/.../-25\cdot6$	$-35\cdot8/.../-12\cdot7$	$-14\cdot0/.../-4\cdot96$	2·6
Torsion/ext. press.	$-5\cdot9/1\cdot79/-30\cdot4$	$-5\cdot1/9\cdot2/-15\cdot3$	$-5\cdot5/9\cdot8/-16\cdot3$	0·94
Comp./tor./Ext. press.	$-18\cdot1/2\cdot04/-23\cdot0$	$-15\cdot6/10\cdot4/-11\cdot.6$	$-11\cdot4/7\cdot4/-8\cdot4$	1.4

*Estimated from approximate stress analysis and Tsai–Wu failure criterion.
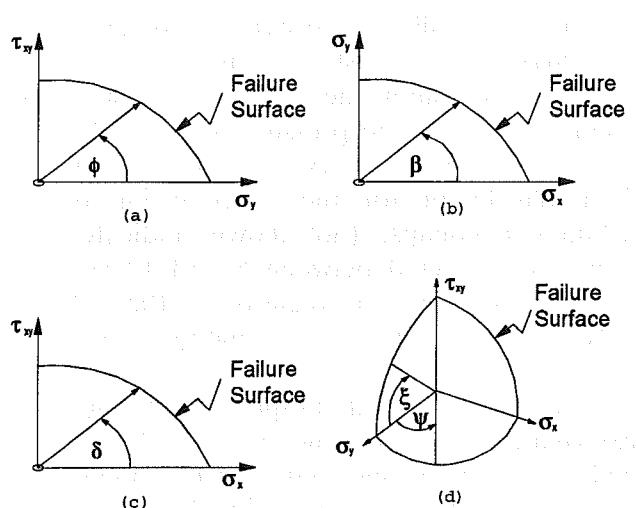
Fig. 7. Definition of phase angles ϕ, β, δ, ξ and ψ quantifying relation between stresses τ_{xy} and σ_y (a), σ_y and σ_x (b), τ_{xy} and σ_x (c), τ_{xy} and σ_y and σ_y and σ_x (d).

pressure and induced compression load at buckling was 1.79 kNm, -30.4 kPa and -5.9 kN (Table 4). This combination corresponds to stresses $\tau_{xy} = 9.2$ MPa, $\sigma_x = -15.3$ MPa and $\sigma_y = -5.1$ MPa in the facings. The buckling stresses are slightly less than the failure stresses, Table 4, which indicates that global buckling of the cylinder is a possibility for this case.

In the case of combined axial compression, torsion and external pressure, the calculated buckling stresses are (Table 4): $\sigma_y = -15.6$ MPa, $\tau_{xy} = 10.4$ MPa and $\sigma_x = -11.6$ MPa. The results in Table 4 show that the buckling stresses are 40–50% larger than the failure stresses which indicates that the cylinder should not fail by buckling.

DETAILED FINITE ELEMENT STRESS ANALYSIS AND FAILURE PREDICTION

Detailed FE stress analyses of the corrugated board cylinders under combinations of axial compression, torsion and external pressure are presented. Buckling was not considered in this section. FE models incorporating the end caps and the cylinder were developed, see Fig. 8. The end caps were reinforced with radial T-

beam reinforcements mounted at 45° increments. FE models of the cylinder and end caps and boundary conditions are described in Ref. 9. The thicknesses and material properties of the board constituents used in the analyses are listed in Tables 1 and 2. Note that the outer facing is slightly thicker than the inner facing. Hence, the board is not completely symmetric. Compressive load and torque were applied at the center of the end caps and external pressure was applied on the elements of the cylinder wall. The proportional constants between load, torque and external pressure are listed in Table 5. Initial values of the force, torque and pressure were set to 20% of the previously computed critical buckling load, torque and external pressure combinations (Table 4). The stresses are calculated in both facings to detect which facing is the first to fail. The magnitudes of axial load, torque and external pressure were increased until the Tsai–Wu failure criterion, eqn (8), was fulfilled. This analysis thus provides the loads, torques and external pressures and the stresses at failure for both the inner and outer facings. The location of failure initiation is determined from the Tsai–Wu factor.

Pure torsion was considered first. The calculated torques at collapse and the Tsai–Wu factor of the inner and outer facings are listed in Table 6. Table 6 reveals that the Tsai–Wu factor of the inner facing reaches the critical value of one prior to the outer facing. The torques at collapse calculated for the inner and outer facings were 3.45 and 3.98 kNm, respectively. The analysis thus indicates that the inner facing would fail prior to the outer facing. Fig. 9 shows a contour plot of the Tsai–Wu factor (eqn (12)) for the inner facing at a torque of 3.45 kNm. Based on Fig. 9, failure of the cylinder is expected to initiate in regions where the Tsai–Wu factor is close to one, thus between the radial reinforcements of the end caps between 0 and 5 cm from the cylinder ends. The reinforcements apparently induce stress concentrations in the cylinder wall. Failure may also be initiated at the middle

Table 5. Phase angles ans proportional constants for combined loading

Loading case	Phase angles	Proportional constants
Comp./ext. pressure	$\beta = 70°$	$k_{CP} = 6.1 \times 10^{-7}$ mm^{-2}
Torsion/ext. press.	$\delta = 30°$	$k_{TP} = 1.7 \times 10^{-8}$ mm^{-3}
Comp./tor./ext. press.	$\xi = 40°$, $\psi = 45°$	$k_{CP} = 1.3 \times 10^{-6}$ mm^{-2} and $k_{CT} = 112$ mm

region of the cylinder as indicated by the Tsai–Wu factor (Fig. 9).

For an externally pressurized cylinder, the inner facing is predicted to first collapse at a pressure of −37·4 kPa (Table 6). Figure 10 illustrates that the pressurized cylinder assumes an hour-glass shape because of the end constraints from the end caps. Failure initiation is expected 9–12 cm from the cylinder ends.

For a cylinder loaded in a combination of torsion and external pressure, the normal and shear stresses at collapse of the facings are listed in Table 6. Inspection of the Tsai–Wu factor for this load case, Table 6, reveals that the inner facing would fail prior to the outer facing. The Tsai–Wu factor plot (not shown) reveals that the collapse of the cylinder wall is expected to occur in a region between 9 and 20 cm from the cylinder ends at a torque of 1·99 kNm and an external pressure of −33·7 kPa (Table 6).


Fig. 8. Model of symmetry sections of cylinder and loading plate.

For an axially compressed and externally pressurized cylinder, stress analysis predicts collapse of the outer facing (prior to the inner facing) at a load and pressure of −13·5 kN and −9·4 kPa (Table 6). A contour plot of the Tsai–Wu factor for the outer facing of the cylinder at collapse (not shown) indicates that failure is expected between 5 and 12 cm from the cylinder ends in regions of the cylinder between the radial reinforcements of the end caps.

For combined axial compression, torsion and external pressure, the calculated combination of collapse load, torque and external pressure is −13·1 kN, 1·48 kNm and −16·7 kPa (Table 6). Failure is expected to initiate in the outer facing between 8 and 10 cm from the cylinder ends in regions between the reinforcements of the end caps.

ANALYSIS OF LOCAL BUCKLING

FE analysis of local buckling was performed on an element of the cylinder wall. The board element analysed must be representative for the sandwich and must consider enough flute wavelengths to accommodate the local buckling pattern. To reduce the influence of the edge effects, a square section of four wavelengths in side length was considered. Buckling analysis was performed using the ANSYS finite element code.[8,12,15] Three load cases were studied, viz. axial compression in the CD, axial compression in the MD and pure in-plane shear loading. The material properties of the constituents and the board geometry parameters used in the analysis are listed in Tables 1 and 2.

The constituents of the corrugated board were modeled by using the isoparametric shell element STIF93 which is particularly well suited for modeling of curved shell structures. The

Table 6. Calculated collapse load, torque, pressure, and stresses of the facings (50% RH and 23°C)

| Loading case	Inner facing							Outer facing						
	F (kN)	T (Nm)	P (kPa)	σ_y (MPa)	τ_{xy} (MPa)	σ_x (MPa)	T–W*	F (kN)	T (Nm)	P (kPa)	σ_y (MPa)	τ_{xy} (MPa)	σ_x (MPa)	T–W*
Torsion	0	3450	0	0	18·5	0	1·0	0	3980	0	0	21·3	0	0·99
External pressure	−7·3	0	−37·4	−6·2	0	−19·3	1·0	−6·20	0	−38·5	−5·2	0	−19·9	0·96
Torsion/ext. press.	−6·6	1985	−33·7	−4·9	10·7	−17·7	1·0	−5·7	2400	−34·7	−4·3	12·9	−18·2	0·95
Ax. comp./ext. press.	−10·8	0	−9·7	−10·0	0	−4·9	0·91	−13·5	0	−9·4	−12·4	0	−4·8	1·0
Comp./tor./ext. press.	−11·8	1100	−16·6	−10·7	6·5	−7·9	0·93	−13·1	1480	−16·7	−11·8	8·6	−7·9	1·0

*T–W is the Tsai–Wu factor.
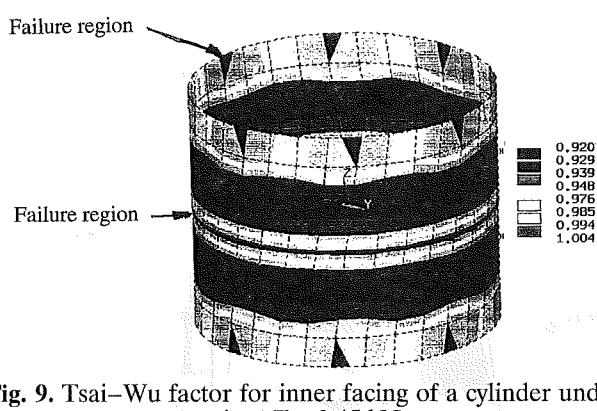
Fig. 9. Tsai–Wu factor for inner facing of a cylinder under torsion. $T = 3\cdot45$ kNm.

panel was generated by describing the geometry, Fig. 11, using keypoints and area elements. The core was assumed to have a sinusoidal shape. A total of 825 elements were used to discretize the corrugated board element. The nodes on the fluting tips were rigidly coupled to the corresponding nodes on the facings using constraint equations [15].

For an element loaded in compression, displacements of the nodes at the bottom supporting edge were set to zero. The unloaded edges were assumed to be constrained from
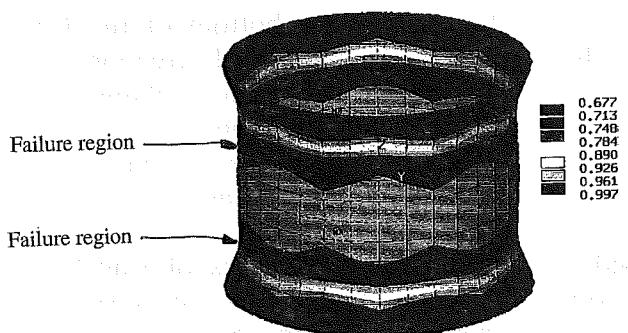

Fig. 10. Deformed shape and Tsai–Wu factor for the inner facing of an externally pressurized cylinder. $P = -37\cdot4$ kPa.
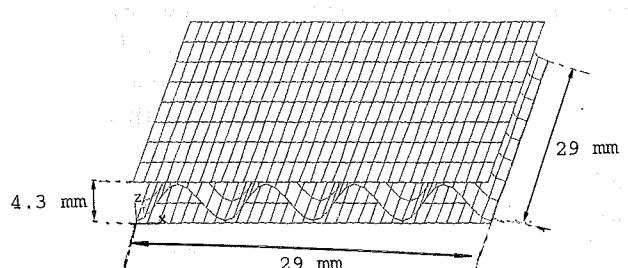
Fig. 11. Corrugated board element used in analysis of local buckling. The thickness is 4·3 mm and the planer dimensions are 29 mm × 29 mm.

Table 7. Line loads (N/mm) at local buckling of the facings

	Inner facing	Outer facing
Compression load in the CD	10·0	12·8
Compression load in the MD	3·6	4·9
Shear load	10·9	···

transverse displacements. The loaded edge was subjected to a uniform axial displacement to represent compression loading. Transverse displacements were prohibited at the loaded edge. Shear loading of the board element was simulated by application of equal magnitude shear forces (F_x and F_y) in the x and y directions on all edge nodes of the facings. One corner of the element was fixed to prevent rigid body translation of the element, and the edges were constrained from all rotations, i.e. the edges were required to remain straight after deformation, and opposite parallel edges remained so after deformation.

The calculated critical local buckling loads of the facings are listed in Table 7. For a corrugated board panel loaded in the CD, the inner facing buckles at $N_{cr} = 10$ N/mm, and the outer facing at $N_{cr} = 12\cdot8$ N/mm. Notice that the inner facing is thinner than the outer facing (Table 1) which explains its lower buckling load. Figure 12(a) displays the buckling pattern for the CD compression loaded board element. The inner facing buckles at $N_{cr} = 10$ N/mm between two fluting tips at a wavelength (λ_x) of 14·5 mm in the MD, which is approximately twice the fluting wavelength, and in approximately 2·5 wavelengths ($\lambda_y = 10\cdot9$ mm) in the CD. The outer facing is predicted to buckle at $N_{cr} = 12\cdot8$ N/mm in about three wavelengths in the CD ($\lambda_y = 9\cdot7$ mm) and two wavelengths in the MD ($\lambda_x = 14$ mm, not shown here).

For the board element loaded in compression in the MD, the inner facing buckles at 3·6 N/ mm prior to the outer facing at 4·9 N/mm (Table 7). The inner facing buckles only in the MD at a wavelength $\lambda_x = 14$ mm, which is approximately twice the fluting wavelength (Fig. 12(b)). The outer facing buckles in two wavelengths in both MD and CD ($\lambda_x = \lambda_y = 14$ mm). When the outer facing buckles, the wavelength of the inner facing in the MD decreases to $\lambda_x = 9\cdot7$ mm. At this load the inner facing also buckles in the CD in one wavelength ($\lambda_y = 14\cdot5$ mm).

For shear loading, buckling of the inner facing is predicted at a shear stress $\tau_{xy} = 10.9$ N/mm. Figure 12(c) illustrates the local buckling pattern of the inner facing at $\tau_{xy} = 10.9$ N/mm. It is noted that the inner facing buckles in a wavelength of approximately 11 mm (two and a half fluting wavelengths) in both MD and CD. We were not able to calculate the local buckling load for the outer facing. Up to 30 SLMs were examined and none of them revealed buckling of the outer facing.

EXPERIMENTAL SET-UP

The corrugated board cylinders were fabricated as detailed in Ref. 9. The cylinder were attached to end caps using Roses metal [16]. Eighteen cylinders were tested on a servohydraulic MTS test frame, and three cylinders were tested in pure torsion on a specially designed frame.
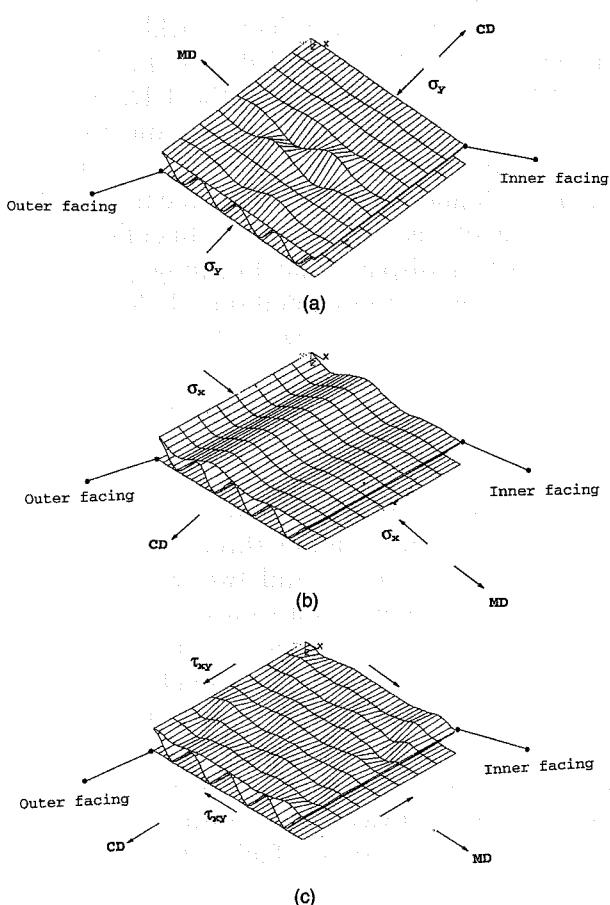
Fig. 12. (a) Local buckling pattern of the inner facing for an axially compressed board panel in CD. $N_{cr} = 10$ N/m. (b) Local buckling of the inner facing for an axially compressed board panel in MD. $N_{cr} = 3.6$ N/m. (c) Local buckling pattern of the inner facing for a shear loaded corrugated board panel. $N_{cr} = 10.9$ N/m.
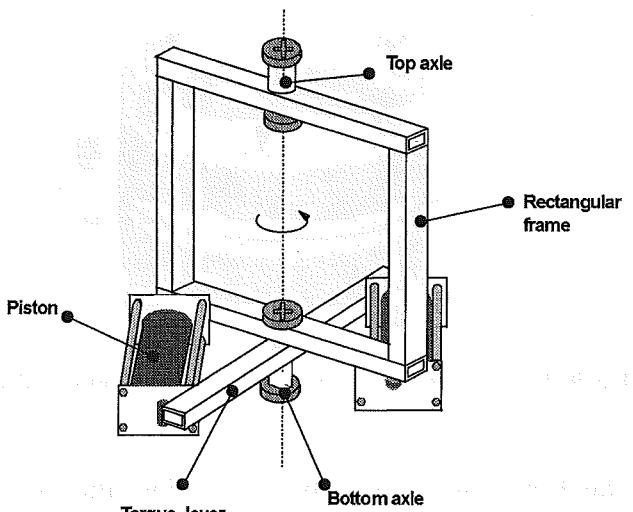
Fig. 13. Torque loading frame.

The torque limit of the MTS loading frame was 1 kNm. Larger torques are required to fail the cylinder, and therefore a special torque fixture, capable of 4 kNm, was designed. The fixture consists of a 0.6×0.85 m frame made from four quadratic (45×45 mm) steel rods of 3 mm wall thickness welded together (Fig. 13). A 0.85-m-long torque lever (Fig. 13) also made from 45×45 mm steel rod, transferred torque to the frame. The lever and the frame are fit onto a solid axle at the bottom of the frame with a rotational degree of freedom only (Fig. 13). The top of the frame contains a solid circular axle with both rotational and translational degrees of freedom. Two pistons, activated through pressurized air, were attached between the torque lever and the frame to provide the torque. For purposes of transferring torque to the cylinder and centering the cylinder, cross-shaped grooves were machined in the end caps, fitting cross-shaped heads machined at the top and bottom ends of the axles (Fig. 13). To examine and record local buckling and failure of both facings, three high shutter speed video cameras (25 pictures/sec) were placed on each side of the cylinder (front and back) and inside the cylinder, see Fig. 14.

Three cylinders were tested for each loading combination in the MTS frame and three in the torque frame. Cylinders subjected to torsion only and external pressure only were conditioned (for 48 hours) and tested at $50 \pm 2\%$ RH and $24 \pm 1°C$. Humidity was controlled by circulating humid air (of 50% RH and 24°C) between a humidity generator and the interior of the cylinder. The PE-coating on the outer
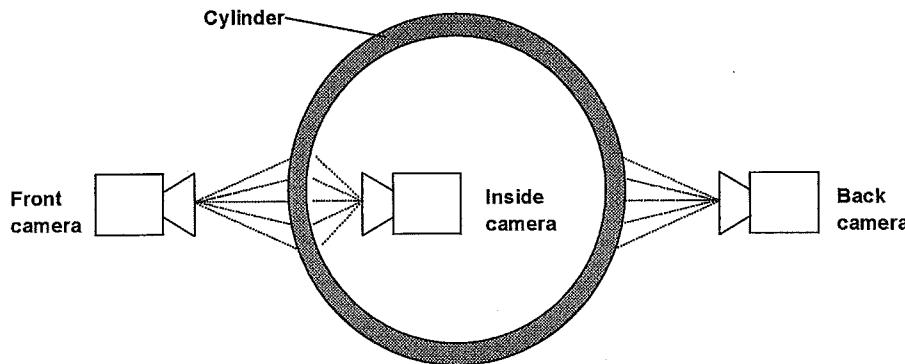
Fig. 14. Placement of the three high shutter speed video cameras.

facing sealed the board from the laboratory environment. Fifteen cylinders were conditioned and tested in the MTS frame at between 20 and 26% RH and 23±1°C. The strength of the board is not expected to be significantly altered in the relative humidity range between 20 and 50% RH,17 and therefore, we did not attempt to correct the strength for changes in RH.

External pressure loading of a cylinder is most simply obtained by applying vacuum inside the cylinder. The PE coating of the outer facing seals the board and prevents air transport through the cylinder wall. The cylinder ends are sealed by fixing the cylinder ends to the end caps using Roses metal [16]. Thus, when vacuum is applied in the cylinder, the cylinder will experience action of the external atmospheric pressure. Control of the external pressure level is achieved through a feedback vacuum control system employing a pressure gage placed inside the cylinder. To obtain a state of pure hoop stress, uniaxial compression tests of side supported laser-cut dog-bone shaped specimens shown in Fig. 15 were performed according to a procedure detailed in Ref. 18. These specimens were conditioned before and during testing at 24°C and 50% RH.

EXPERIMENTAL RESULTS

Three cylinders were tested in pure torsion. The torque was increased by 200 Nm/s. Torque versus twisting angle plots for the three cylinders are shown in Fig. 16. Very little scatter between the responses of the cylinders is observed. The torque increases linearly until about 2·5 kNm and failure occurs at approximately 2·8 kNm. Figure 17 shows the inside and outside of a

torqued cylinder. At approximately 2·3 kNm, local buckles were observed on the inner facing close to the cylinder end, Fig. 17(a). After onset of local buckling of the inner facing, failure of the cylinder initiated near one end. Figure 17(b) shows that the collapse zone propagated in a direction approximately 45° with respect of the cylinder axis, since transformation of the inplane shear stress reveals that one of the two principal stresses is compressive in the 45° direction. The measured local buckling and collapse torques for the cylinders are listed in Table 8.

Three cylinders were subjected to external pressure. The external pressure was increased by 1 kPa/s. Below pressures of −12 and −13 kPa, no indication of local buckling or failure was observed by visual inspection of the outer facing. The inner facing of the cylinder was not observed in these tests. Between pressures of −15 and −17 kPa, the outer facing buckled and collapsed between two fluting tips,
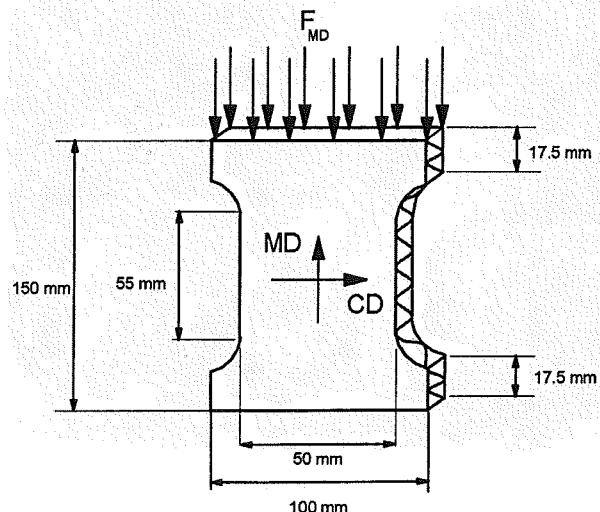
Fig. 15. MD compression test specimen.
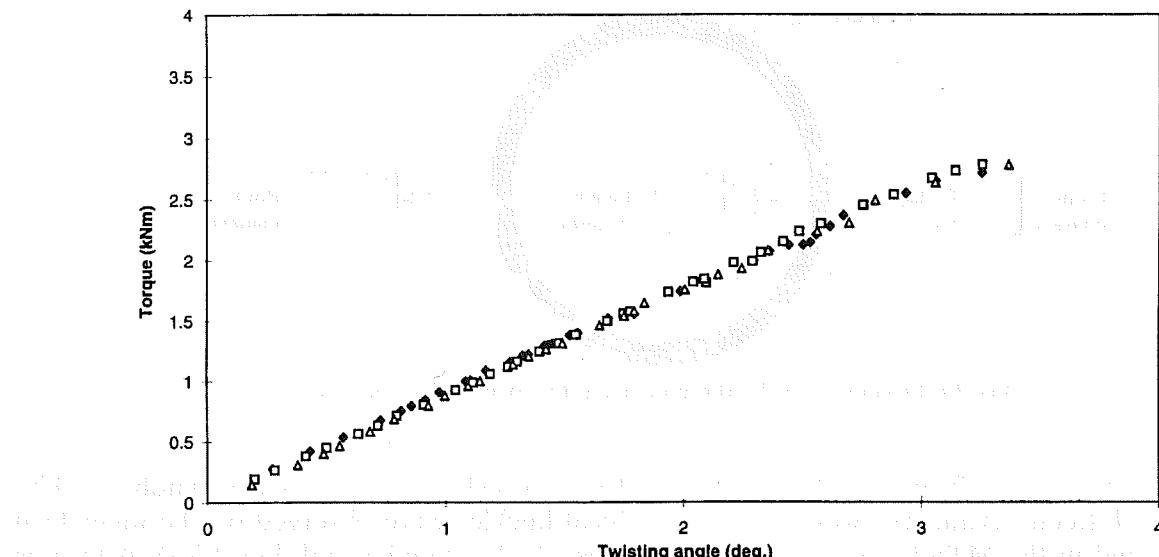
Fig. 16. Torque versus twisting angle.

and the cylinder wall buckled inwards (Fig. 18). Collapse pressures and loads (F_{plate}) measured for the three cylinders are listed in Table 9. For comparison, eight MD specimens (Fig. 15) were

tested in uniaxial compression at a crosshead speed of 10 mm/min. The facings of the specimen collapsed between two fluting tips at a stress, σ_x, between $-7 \cdot 0$ and $-7 \cdot 9$ MPa (average $-7 \cdot 6$ MPa), see Table 9 (uniaxial). Note in Table 9 that the uniaxial collapse stress closely
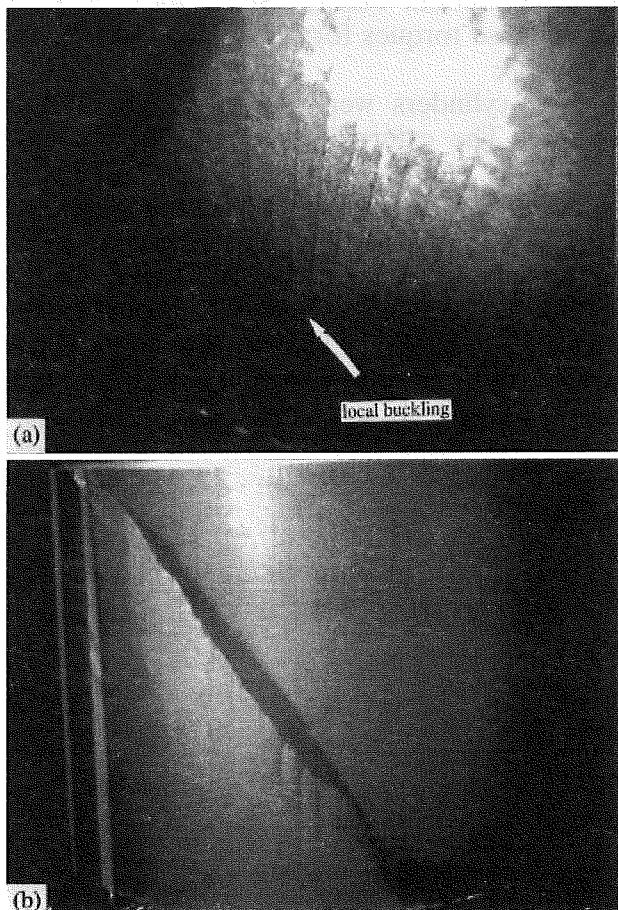
Fig. 17. (a) Local buckling of the inner facing at T = 2·4 kNm. (b) Photo of the outside of the cylinder. Failure initiates near the cylinder end at $T = 2 \cdot 78$ kNm.

Table 8. Torsion test results (50% RH and 24°C)

Test	Local buckling* torque (Nm)	Local buckling stress* τ_{xy} (MPa)	Collapse torque (Nm)	Collapse stress τ_{xy} (MPa)
1	2370	12·1	2710	13·9
2	2430	12·5	2780	14·2
3	2370	12·1	2780	14·2

*Inner facing.

Fig. 18. Photo of an externally pressurized cylinder at $P = -15 \cdot 8$ kPa.

Table 9. External pressure test results (50% RH and 24°C)

Test	External pressure at collapse (kPa)	Collapse stress σ_y (MPa)	F_{plate} at collapse (kN)	Collapse stress σ_y (MPa)
1	−15·8	−8·0	−3·1	−2·7
2	−14·8	−7·5	−2·9	−2·5
3	−15·7	−7·9	−3·1	−2·7
Uniaxial*		−7·6	···	···

*Results from uniaxial MD-tests.

Table 10. Combined axial compression and external pressure test results (25% RH and 23°C)

Test	Collapse load kN)	Collapse external pressure (kPa)	Collapse stress σ_y (MPa)	Collapse stress σ_x (MPa)
1	−11·4	−6·9	−9·8	−3·5
2	−12·8	−7·7	−11·0	−3·9
3	−11·7	−7·2	−10·1	−3·6

agrees with data from the external pressure tests.

For axially compressed and externally pressurized cylinders, the pressure was increased in proportion to the axial force. The proportional constant listed in Table 5, $k_{CP} = 6·1 \times 10^{-7}$ mm^{-2}, means that the magnitude of axial force was increased by 2 kN/min and the pressure in the cylinder was decreased by 1·2 kPa/min. Below loads of −7 kN, there was no indication of local buckling or failure. Between −11 and −13 kN, the outer facing buckled inwards between two fluting tips near the overlap region of the cylinder and the cylinder wall collapsed shortly thereafter near its mid-section (Fig. 19). The failure loads and pressures and correspond-

ing stresses for the three cylinders are listed in Table 10.

For torqued and externally pressurized cylinders, the pressure decreased in proportion to the applied torque by a factor of $k_{TP} = 1·7 \times 10^{-8} mm^{-3}$ (Table 5). The torque increased by 100 Nm/min and the external pressure was decreased by 1·7 kPa/min. At a torque of about 500 Nm and pressure of about −9 kPa, the cylinders failed in an inward buckling mode before any indication of local buckling. Fig. 20 shows a collapsed cylinder. Thus, the cylinders appeared to globally buckle. The collapse torque and pressure and corresponding stresses for the three cylinders are listed in Table 11. For the axially compressed, torqued and externally pressurized cylinders the proportional constants, k_{CT} and k_{CP}, are

Fig. 19. Collapse of an axially compressed and externally pressurized cylinder at $F = -11·4$ kN and $P = -6·9$ kPa.
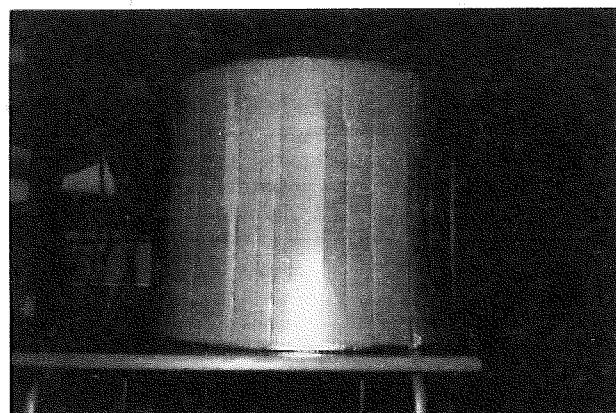
Fig. 20. Collapse of a torqued and externally pressurized cylinder at $T = 510$ Nm and $P = -8·9$ kPa.

Table 11. Combined torsion and external pressure test results at collapse (23% RH and 22°C)

Test	Torque (Nm)	External pressure (kPa)	F_{plate} (kN)	τ_{xy} (MPa)	σ_x (MPa)	σ_y (MPa)
1	440	−7·6	−1·5	2·2	−3·8	−1·3
2	530	−9·2	−1·8	2·7	−4·6	−1·5
3	510	−8·9	−1·7	2·6	−4·5	−1·4

112 mm and $1\cdot3\times10^{-6}$ mm^{-2}, respectively (Table 5). The magnitude of the compression load was increased by 2 kN/min, the torque by 112 Nm/min and the external pressure was decreased by $1\cdot3$ kPa/min. For compression loads below -4 kN, local buckling and failure was not observed. At loads between -4 and $-5\cdot5$ kN, the outer facing buckled inwards between two fluting tips. The cylinder collapsed totally at loads between $-6\cdot2$ and $-7\cdot5$ kN (Fig. 21). The collapse initiated between 10 and 20 cm from the cylinder ends and the collapse zone propagated in a direction approximately 45° with respect to the cylinder axis (Fig. 21). No indication of global buckling of the cylinder was observed prior to failure. Collapse loads,

torques, pressures and collapse stresses for the three cylinders are listed in Table 12.

COMPARISON BETWEEN ANALYSIS AND EXPERIMENTS

In this section the experimental local buckling and collapse stresses will be compared with the global buckling, local buckling and collapse stresses obtained from FE analysis.

Axial compression

Axially compressed cylinders were examined experimentally in Ref. 9. Local buckling of the outer facing was observed at $\sigma_y = -8\cdot3$ MPa (Table 13). Unfortunately, the inner facing was not observed. Local buckling was predicted to occur at $\sigma_y = -13\cdot6$ MPa and $-17\cdot3$ MPa for the inner and outer facings, respectively (Table 13). Thus, the local buckling analysis provides a highly unconservative prediction of the local buckling stress for the outer facing. The cylinders are predicted to collapse by material failure of the wall at a stress, σ_y, of $-13\cdot9$ MPa,9 which is within 3% of the experimental collapse stress ($\sigma_y = -14\cdot3$ MPa; Table 14). The local buckling observed prior to collapse therefore does not appear to influence the failure stress of the board for this loading case, Table 13Table 14.
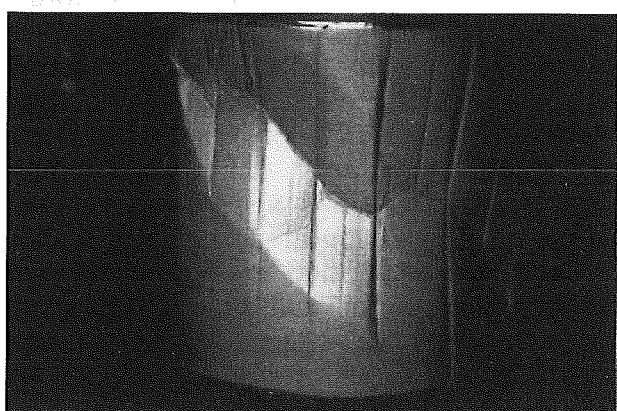
Fig. 21. Collapse of an axially compressed, torqued and externally pressurized cylinder at $F = -6\cdot7$ kN, $T = 740$ Nm and $P = -8\cdot5$ kPa.

Table 12. Combined axial compression, torsion and external pressure test results (21% RH and 23°C)

Test	Collapse load (kN)	Collapse external pressure (kPa)	Collapse torque (Nm)	Collapse stress σ_y (MPa)	Collapse stress σ_x (MPa)	Collapse stress τ_{xy} (MPa)
1	$-6\cdot7$	$-8\cdot5$	740	$-5\cdot8$	$-4\cdot3$	$3\cdot8$
2	$-6\cdot2$	$-8\cdot2$	710	$-5\cdot3$	$-4\cdot1$	$3\cdot6$
3	$-7\cdot5$	$-9\cdot5$	840	$-6\cdot4$	$-4\cdot8$	$4\cdot3$

Table 13. Comparison between experimental and analytical local buckling stresses (MPa)

| Loading case | Experimental | | | | | | FEM | | | | | |
| | Outer facing | | | Inner facing | | | Outer facing | | | Inner facing | | |
	σ_y	τ_{xy}	σ_x	σ_y	τ_{xy}	σ_x	σ_y	τ_{xy}	σ_x	σ_y	τ_{xy}	σ_x
Axial compression	$-8\cdot3$	—	—	—	—	—	$-17\cdot3$	—	—	$-13\cdot6$	—	—
Torsion	—	—	—	—	$12\cdot2$	—	—	—	—	—	$21\cdot8$	—
External pressure	—	—	—	—	—	$-7\cdot6$	—	—	$-9\cdot8$	—	—	$-7\cdot2$

Table 14. Comparison between experimental and analytical collapse stresses (MPa)

Loading case	Experimental			FEM		
	σ_y	τ_{xy}	σ_x	σ_y	τ_{xy}	σ_x
Axial compression*	−14·3	—	—	−13·9	—	—
Torsion	—	14·1	—	—	17·7	—
External pressure	−2·6	—	−7·8	−6·2	—	−18·8
Ax. comp./ext. press.	−10·3	—	−3·7	−11·8	—	−4·7
Ax. comp./torsion*	−14·5	4·6	—	−14·2	4·5	—
Torsion/ext. press.	−1·4	2·5	−4·3	−5·7	10·2	−16·9
Comp./tor./ext. press.	−5·8	3·9	−4·4	−11·3	7·6	−8·4

*Data from Ref. 9.

Torsion

Local buckling was observed on the inner facing (Fig. 17(a)), at a shear stress $\tau_{xy} = 12·2$ MPa (Table 13). FE analysis predicts a much larger local buckling stress of the inner facing ($\tau_{xy} = 21·8$ MPa, Table 13). Consequently, the linear elastic eigenvalue analysis over predicts the critical local buckling stress. The measured shear stress at collapse is 14·1 MPa (Table 14) which is close to the observed local buckling stress (Table 13). FE stress analysis in combination with the Tsai–Wu failure criterion somewhat overpredicts the collapse stress ($\tau_{xy} = 17·7$ MPa; Table 14). The collapse mechanism of the torqued cylinders thus seem to be governed by local buckling of the inner facing.

External pressure

The cylinders collapsed by local buckling at a stress $\sigma_x = -7·6$ MPa (Table 9). FE analysis predicts local buckling of the inner facing at $\sigma_x = -7·2$ MPa and at $\sigma_x = -9·8$ MPa for the outer facing (Table 13). The Tsai–Wu criterion predicts collapse of the cylinder at $\sigma_x = -18·8$ MPa, which is more than twice the magnitude of the measured collapse stress ($\sigma_x = -7·8$ MPa; Table 14). The cylinder apparently collapsed as a result of local buckling instability of the inner facing.

Combined loadings

For cylinders loaded in combined axial compression and external pressure, the FE-predicted collapse stresses σ_y and σ_x (Table 14) are in reasonable agreement with experimental data (Table 14). The global buckling stresses listed in Table 4 are approximately twice the FE-predicted collapse stresses, and there were no experimental indications that the

cylinders failed by global instability. Local buckling of the outer facing was observed just before the cylinder collapsed. It should be kept in mind that axial loading dominated ($\beta = 70°$, Table 5), which seems to diminish the influence of local buckling on the collapse mechanism.

For the torqued and externally pressurized cylinders, failure occurred at a shear stress $\tau_{xy} = 2·5$ MPa and hoop stress $\sigma_x = -4·3$ MPa (Table 14). Comparing these stresses with the predictions from the FE stress analysis (Table 14) it is noted that the experimental failure stresses are approximately one fourth of the predictions. Experimental observations, however, indicated that the cylinders buckled globally at collapse before local buckling or material failure occurred. The FE analysis of global buckling also showed that torsion and external pressure loading may lead to global buckling of the cylinder. The combined strength data for this loading case should thus be viewed with caution.

For cylinders subjected to combined axial compression, torsion and external pressure, comparison between experimental and FE predicted collapse stresses (Table 14) reveals that the experimental collapse stresses are approximately 50% less than the predicted. The experimental collapse stresses are, however, less than half the critical buckling stresses (Table 4) which would indicate that the cylinders did not fail due to global buckling instability. Inspection of the cylinders (Fig. 21) and the above discussion point to collapse induced by local buckling.

FAILURE ENVELOPES

The experimental failure envelope for the facings of corrugated board is obtained by plotting the experimental failure locus in stress space. For this purpose the approximate stress analysis

and the measured loads, torques and pressures were employed. Experimental axial compression and combined axial compression and torsion data of Ref. 9 are also included in this section.

Figure 22(a) shows failure envelopes σ_y versus τ_{xy} ($\sigma_x = 0$) generated by visually fitting a curve through the experimental collapse stresses, and the Tsai–Wu prediction. Note in
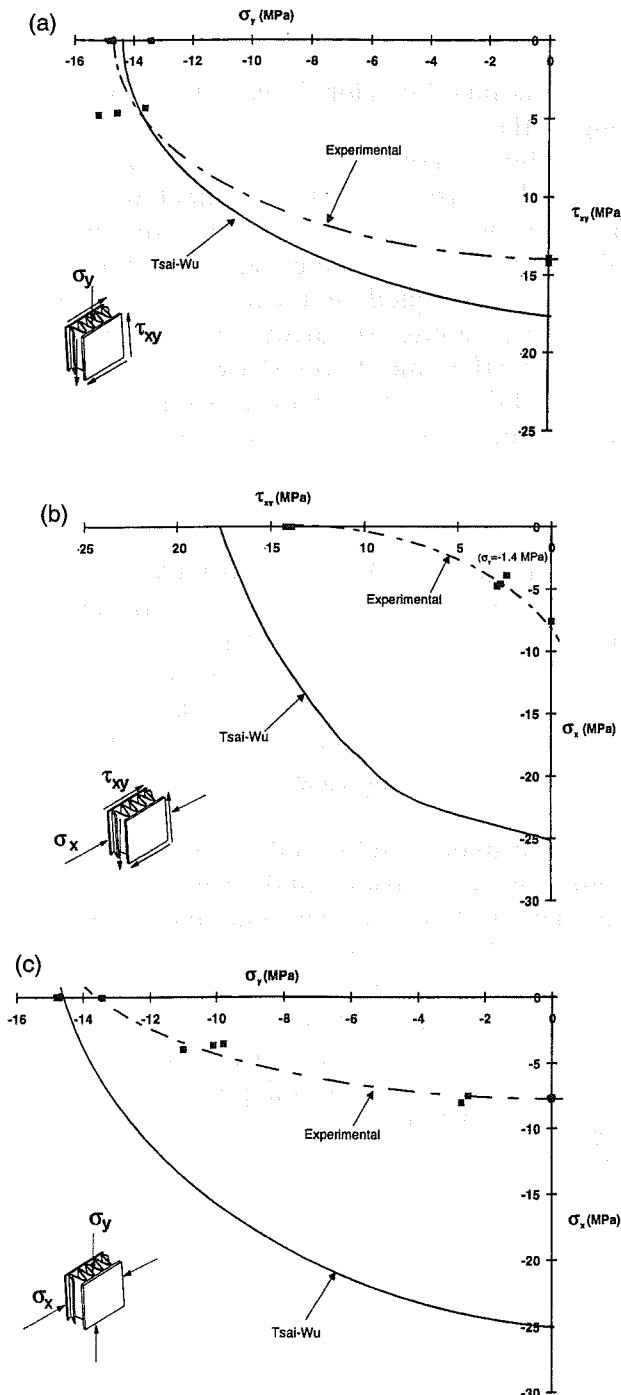
Fig. 22(a) that the experimental collapse stresses (squares) closely follow the Tsai–Wu failure criterion for pure axial compression and compression combined with a small shear stress, but falls below the Tsai–Wu envelope for shear dominated fields due to the strong influence of local instability of the facings. Figure 22(b) shows experimental and Tsai–Wu failure envelopes in the stress σ_x versus shear stress τ_{xy} quadrant. The magnitudes of the experimental failure stresses (squares) fall much below the Tsai–Wu predictions. For combined torsion and external pressure, the Tsai–Wu failure criterion overpredicts the collapse stresses by a factor of about four because the cylinders appeared to fail by global buckling. It should be noticed, however, that the pure compression and shear strengths of the board are not influenced by global buckling of the cylinder, but are governed by local buckling of the facings. The odd shape of the experimental failure envelope occurs because the torsion/external pressure strength data are too low as a result of global buckling of the cylinders, and hence should be viewed with caution. The experimental and Tsai–Wu failure envelopes for σ_y versus σ_x quadrant ($\tau_{xy} = 0$) are displayed in Fig. 22(c). As discussed in connection with Fig. 22(a), the pure axial compression failure stress is in good agreement with the Tsai–Wu failure criterion. The experimental strength data, however, fall much below the Tsai–Wu failure envelope at large magnitudes of the normal stress σ_x. In loadings dominated by σ_x the experimental strengths are about one third of the predictions from the Tsai–Wu criterion. This strength loss is attributed to the strong influence of local buckling on the collapse mechanism for this loading case.

CONCLUSIONS

An experimental study of failure of corrugated board under combined stress has been performed. Biaxial loading of the board was obtained by subjecting corrugated board cylinders with the corrugations along the cylinder axis to combinations of axial compression, torsion and external pressure. The effective collapse stresses of the board in the absence of local buckling were predicted from stress analysis of the cylinder in combination with the Tsai–Wu failure criterion. Local buckling stres-

Fig. 22. Experimental and analytical (Tsai—Wu) failure envelopes for the facings (liners) of corrugated board: (a) σ_y and τ_{xy} stress quadrant; (b) τ_{xy} and σ_x stress quadrant; (c) σ_y and σ_x stress quadrant.

ses for the facings were predicted from linear elastic FE eigenvalue analysis of a small board element.

For pure axial compression parallel to the corrugations (CD), and compression in the CD superimposed with small torsion, material failure of the facings appeared to govern the collapse mechanism of the board. Local buckling was observed near the ends of the cylinder well before collapse. Hence, the facings displayed post buckling strength in compression dominated loading along the corrugations (CD).

Cylinders subjected to pure torsion buckled locally just before collapse. The experimental collapse stresses were approximately 80% of the Tsai–Wu predicted stresses. The torqued cylinders thus seem to collapse when the inner facing locally buckled. A local buckling analysis of a shear loaded board element gave very unconservative results for the critical buckling load.

For loading combinations where compression stress acts perpendicular to the corrugations (MD), the measured collapse stresses fall much below the Tsai–Wu predictions. Local buckling analysis of an axially compressed panel in MD predicts buckling of the facings at a load close to the experimental collapse loads. For such loadings, the collapse of the board is thus governed by local buckling of the facings.

ACKNOWLEDGEMENTS

APPENDIX

PROPORTIONAL CONSTANTS FOR CYLINDERS UNDER COMBINED LOADING

For combined axial compression and torsion loading, the relation between the shear and normal stresses in the facings (Fig. 3) is

$$\tan \phi = \frac{\tau_{xy}}{\sigma_y} \tag{A1}$$

where ϕ is the 'phase angle' (Fig. 7(a)) between the magnitudes of the shear and normal stres-

ses. This means that T should increase in proportion to the magnitude of F, i.e.

$$T = -k_{FT}F \tag{A2}$$

where the proportional constant, k_{FT}, is obtained by substituting Eqs. into Eqs. , which yields

$$k_{FT} = \frac{2Rt_L}{\left(2t_L + \alpha \dfrac{E_{yC}}{E_{yL}} t_C\right)} \tan \phi \tag{A3}$$

where R is the cylinder radius, t_L and t_C are the thicknesses of the facings and core, and E_L and E_C are the Young's moduli for the facing and core.

For cylinders under axial compression and external pressure loading, the relation between the normal stresses in the facings is

$$\tan \beta = \frac{\sigma_y}{\sigma_x} \tag{A4}$$

where β is the 'phase angle' (Fig. 7(b)) between the magnitudes of the normal stresses, σ_y and σ_x. The proportional constant, k_{FP}, between the axial compression load, F, and external pressure, P, is then

$$P = k_{FP}F \tag{A5}$$

where

$$F = F_{cyl} + F_{plate} \tag{A6}$$

where F_{cyl} is the applied axial compression load on the cylinder and $F_{plate} = PA_{plate}$ with A_{plate} being the area of the end caps. k_{FP} is expressed as

$$k_{FP} = \frac{k_1}{1 + k_1 A_{plate}} \tag{A7}$$

where

$$k_1 = \frac{t_L}{\pi R^2 \tan \beta \left(2t_L + \alpha \dfrac{E_{yC}}{E_{yL}} t_C\right)} \tag{A8}$$

For cylinders subjected to torsion and external pressure, the normal stress, σ_x, in the facings is increased proportionally to the shear stress in the facings, τ_{xy}, as defined by the phase angle δ (Fig. 7(c))

$$\tan \delta = \frac{\tau_{xy}}{\sigma_x} \tag{A9}$$

The pressure and torque relation is expressed by;

$$P = -k_{TP}T \qquad (A10)$$

Substituting Eqs. into Eqs. yields

$$k_{TP} = \frac{1}{2\pi R^3 \tan \delta} \qquad (A11)$$

In this case the pressure acting on the end caps will contribute to an axial compression load:

$$F_{plate} = A_{plate}P = -A_{plate}k_{TP}T \qquad (A12)$$

For the combined axial compression, torsion and external pressure case, the torque and external pressure are increased in proportion to the axial compression load. The relations between the stresses in the facings σ_y and τ_{xy} and σ_y and σ_x are;

$$\tan \zeta = \frac{\tau_{xy}}{\sigma_y} \qquad (A13)$$

and

$$\tan \psi = \frac{\sigma_y}{\sigma_x} \qquad (A14)$$

with ζ being the 'phase angles' between the magnitude of normal stress, σ_y, and shear stress, τ_{xy} and ψ being the 'phase angle' between the magnitude of normal stresses σ_y and σ_x (Fig. 7(d) and (e)). This means that T is increased proportionally to F by a constant k_{FT};

$$k_{FT} = k_2(1 - A_{plate}k_{FP}) \qquad (A15)$$

where

$$k_2 = \frac{2Rt_L}{\left(2t_L + \alpha \dfrac{E_{yC}}{E_{yL}} t_C\right)} \tan \zeta \qquad (A16)$$

in which k_{FP} is the proportional constant between the axial compression, F, and pressure, P, expressed as

$$k_{FP} = \frac{k_3}{1 + k_3 A_{plate}} \qquad (A17)$$

where

$$k_3 = \frac{t_L}{\pi R^2 \tan \psi \left(2t_L + \alpha \dfrac{E_{yC}}{E_{yL}} t_C\right)} \qquad (A18)$$

REFERENCES

1. Jönsson, G., Corrugated Board Packaging. Pira International, 1993.
2. Johnson, M. W. and Urbanik, T. J., A non-linear theory for elastic plates with applications to characterizing paper properties. J. Appl. Mech. 1984, 51, (3), 145–152.
3. Johnson, M. W. and Urbanik, T. J., Analysis of the localized buckling in composite plate structures with application to determining the strength of corrugated board. J. Compos. Tech. Res. 1989, 11, (4), 121–127.
4. Hahn, E. K., Carlsson, L. A. and Westerlind, B. S., Edge compression fixture for buckling studies of corrugated board panels. Exp. Mech. 1992, 32, 252–258.
5. Hahn, E. K., de Ruvo, A. and Carlsson, L. A., Compressive strength of edge-loaded corrugated board panels. Exp. Mech. 1992, 32, 259–265.
6. Anderson, M. S., Local instability of the elements of truss-core sandwich plate. NASA Technical Report TR R-30, 1959.
7. Zahn, J. J., Local buckling of orthotropic truss-core sandwich. Research Paper FPL 220, USDA Forest Service, Forest Products Laboratory, 1973.
8. Starlinger, A., Ph.D. Dissertation (Inst. of Lightweight Structures and Aerospace Eng., Vienna University of Technology) Sandwich Shell Element, VDI-Velag, Düsseldorf, 1991.
9. Patel, P., Nordstrand, T. & Carlsson, L. A., Instability and failure of corrugated core sandwich cylinders under combined stresses. In Multiaxial Fatigue and Deformation Testing Techniques, ASTM STP, Vol. 1280, ed. S. Kalluri and P. J. Bonacuse, 1997, pp. 264–289.
10. Libove, C. & Hubka, R. E., Elastic Constants for Corrugated Core Sandwich Plates. NACA TN 2289, 1951.
11. Tsai, S. W. and Wu, E. M., A general theory of strength for anisotropic materials. J. Comp. Mater. 1971, 5, 58–80.
12. de Ruvo, A., Carlsson, L. and Fellers, C., The biaxial strength of paper. Tappi J. 1980, 63, (5), 133–136.
13. Fellers, C., Westerlind, B. S. & de Ruvo, A., An investigation of the biaxial failure of paper: Experimental study and theoretical analysis. In Transaction of the Symposium, Cambridge, September 1981, Vol. 1, 1983, pp. 527–559.
14. Timoshenko, S. P. & Gere, J. M., Theory of Elastic Stability, 2nd edn. McGraw-Hill, Singapore, 1963.
15. ANSYS User's Manual, Swanson Analysis System Inc., Houston, PA, 1989.
16. CRC Handbook of Chemistry and Physics, 65th edn. CRC Press, Boca Raton, 1984–1985, F19.
17. Fellers, C. and Brange, A., Impact of water sorption on compression strength of paper. Papermak. Raw Mater. 1985, 2, 529–539. (Mech. Eng. Publ. Ltd., London)
18. Westerlind, B. S. and Carlsson, L., Compressive response of corrugated board. Tappi J. 1992, 75, (7), 146–154.

Paper 7

———

A Strength Prediction Method for Corrugated Board Containers

by

T. Nordstrand, Blackenfeldt, M. and Renman, M.

Report TVSM-3065, Div. of Structural Mechanics,
Lund University, Sweden, 2003.

A Strength Prediction Method for Corrugated Board Containers

Tomas Nordstrand, Mikael Blackenfeldt and Magnus Renman

SCA Research, Box 716, 851 21 Sundsvall, Sweden

ABSTRACT

A method for prediction of the top-to-bottom compression strength of corrugated board containers using finite element analysis was developed. Up to triple-wall corrugated board is accommodated in the finite element model. In order to keep computational time down, the corrugated core layer(s) is considered to be homogeneous with effective material properties, and the complete corrugated board is represented by a multi-ply eight node isoparametric shell element. The shell elements represent the side panels of the box. Coupling elements are used to represent creases at the top and bottom edges.

Buckling and large displacements are considered in the analysis, and container collapse loads are predicted using the Tsai-Wu failure criterion. It is assumed that failure is triggered by material failure in one of the facings of the corrugated board. Local buckling of the corrugated board constituents is not considered in this study, and orthotropic linear elastic material properties are assumed for each layer.

The boxes analysed fail in a post-buckled state. A non-linear finite element method involving Newton-Raphson iterations is discussed in conjunction with the buckling analysis. Convergence of the predicted collapse load with the number of elements used in the model is studied, as well as the sensitivity of the collapse load to the imposed stiffness at the loaded boundaries. Different buckling modes of a box are simulated, giving an in-depth understanding of the relation between the strength of a box and constraints imposed on the panels by the corners of the box. Finally, the results of an extensive testing program comprising about 1,300 box strength tests are summarised and used to verify the container strength prediction method developed.

INTRODUCTION

Although corrugated board has been used for over a century, the packaging design process is still mostly empirical or semi-empirical. Research on corrugated board has been lagging behind its industrial application [1]. There are many reasons for this. One is that the mechanics of corrugated board and packaging are quite complex due to the structure of the board, difficulties in loading and control of boundary conditions.

Consideration of the corrugated board market in recent years, with fewer companies increasing their market shares, has been a driving force for improvement of design procedures. Production volumes have increased considerably. Even small savings in raw material achieved through improved design procedures imply significant cost savings [2].

In addition, with the development of powerful computing tools and structural analysis codes such as finite element software, it is now possible to obtain numerical solutions for the stresses and deformations in corrugated board structures when loaded [3]. The benefits of such an analysis are apparent since the analysis is based on the geometry of the corrugated board and the physical properties of the constituent liners and corrugated medium. In contrast, the empirical approach to design requires manufacture of the board and tedious making and testing of boxes and specimens, cut from board [4].

This work was initiated with the objective of developing a design method based on finite element analysis to predict top-to-bottom compression strength of corrugated containers. The finite element model includes multi-ply eight node isoparametric shell elements for the side panels and coupling elements representing creases at top and bottom edges [5, 6]. Creases are scored folding lines between flaps and sides. McKee and Gander [4] found that 90% of the compression deformation of a box occurs in the creases. The residual compressive and rotational stiffness of the creases, being most important [7], are accommodated using coupling elements [5]. Extensional, shear and bending stiffnesses of the corrugated board are calculated from the geometry and material properties of the constituent liners and medium [8-11]. The material properties are assumed to be orthotropic linear elastic.

In a previous study of collapse of corrugated board panels it was shown that the Tsai-Wu failure criterion [12-13] could be used to predict material failure in one of the facings of the corrugated board panels. The same failure criterion is used in the present analysis of boxes, and local buckling of the outer facings is disregarded [14]. The buckling of side panels requires a non-linear finite element analysis that is solved using the Newton-Raphson method [15, 16]. The solution is terminated when the failure criterion is satisfied.

Convergence of the predicted collapse load with the number of elements used in the model is studied, as well as the sensitivity of the collapse load to the imposed stiffness at the loaded boundaries. Different buckling modes of a box are simulated, giving an in-depth understanding of the relation between the strength of a box and constraints imposed on the panels by the corners of the box.

Finally, extensive testing of boxes made from two different corrugated board grades is used for comparison with finite element predictions.

A commercially available finite element code called ANSYS [5] was chosen to solve these tasks for two main reasons. The software is adapted to operate in Microsoft's Windows NT environment, and the ANSYS Parametric Design Language (APDL) [5] makes it easy to implement algorithms for processing the finite element models.

NUMERICAL MODEL

Material stiffness properties

Up to triple-wall corrugated board is accommodated in the finite element model. To keep computational time down the corrugated core(s) is homogenised [8-11] and the complete corrugated board is represented by a multi-ply eight node isoparametric shell element, SHELL99 [5]. Each layer, from three to seven, of the homogenised corrugated board is described by its thickness and orthotropic elastic properties, i.e. the elastic moduli (EX, EY, EZ), Poisson's ratio (NUXY, NUYZ, NUXZ) and the shear moduli (GXY, GYZ, GXZ). The elastic planes of symmetry are aligned with the machine direction(MD) and cross direction (CD) of the board, see Figure 1.
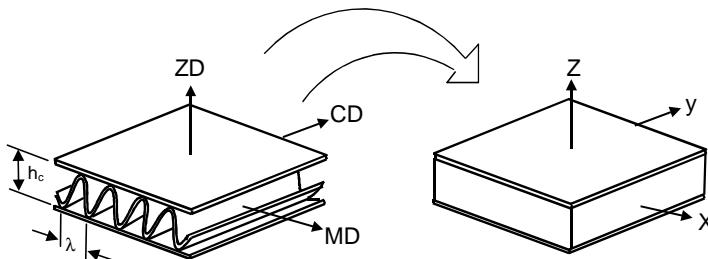
Figure 1. Homogenisation of the corrugated core of single-wall corrugated board.

Model and boundary conditions used for a regular slotted container

In a finite element analysis of a corrugated board container, a quarter of the box is represented by ixk+jxk 8-node elements, i=j and k=2i, where i represents the number of elements parallell with the x-axis, j the number of elements parallell with the y-axis and k the number of elements parallell with the z-axis, see Figure 3. Then the number of nodes is (16+5(i+j-2)+10(k-1)+3(i+j-2)(k-1)). Each node has six degrees of freedom, viz. translation and rotation along axis parallell to the nodal coordinate system. When considering a box loaded under compression, it is recognised that the creases at the top and bottom affect the loading of the box [4]. In order to predict top-to-bottom compression of boxes the properties of the creases were measured in earlier work [7]. The soft creases are accommodated in the FEM-model by edge springs attached at the loaded top and bottom edges. The springs are modelled using element COMBIN14 [5] and the stiffness of the springs is adjusted in order to introduce consistent nodal forces on the shell elements if uniformly compressed [16]. The creases also introduce an eccentricity of the applied loads [7], which is simulated by

introducing a moment that is constant at the top and bottom edges using element COMBIN37 [5], see Figure 2. The vertical edges at the four corners of the box are connected in translation only with no rotational constraint.
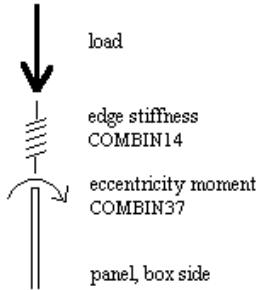
Figure 2.   Elements used to simulate the response of the creases.

A quarter of the box is analysed due to symmetry. Boundary conditions are imposed on the nodes along the edges and nodes at the planes of symmetry according to Figure 3. Only the two symmetry planes indicated in the figure are utilized since the boxes analysed in general have more complex geometry than the box shown in figure 3.
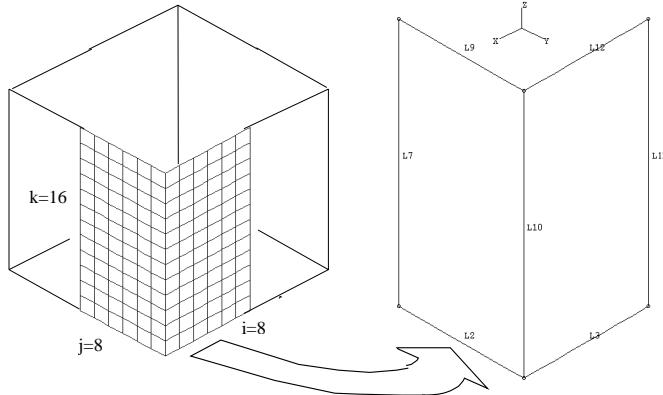
Figure 3. Quarter of a box model with boundary conditions:

L9:   DX=0, DZ=displacement step, (nodes are free to move in y-direction except where L9 intersects L7)
L12:   DY=0, DZ=displacement step
L2:   DX=0, DZ=0
L3:   DY=0, DZ=0
L10:   Translation coupling of the nodes at the corner .
L7:   DY=0, RotX=0, RotZ=0 (symmetry)
L13:   DX=0, RotY=0, RotZ=0 (symmetry)
L9, L12, L2, L3: Connected to elements shown in Figure 2.

Analysis

The stress-strain relationship of each layer, j, can be expressed by [8]

$$\{\sigma\}_j = [Q]_j \{\varepsilon\}_j \tag{1}$$

where $\{\sigma\}_j$ and $\{\varepsilon\}_j$ are the vector stress and strain, respectively, in a plate. Plane stress is assumed and the elastic stiffness matrix $[Q]_j$ is defined as

$$[Q]_j = \frac{1}{1 - \nu_{xy,j}\nu_{yx,j}}
\begin{bmatrix}
E_{x,j} & \nu_{xy,j}E_{y,j} & 0 & 0 & 0 \\
\nu_{yx,j}E_{x,j} & E_{y,j} & 0 & 0 & 0 \\
0 & 0 & G_{xy,j} & 0 & 0 \\
0 & 0 & 0 & \dfrac{G_{yz,j}}{f} & 0 \\
0 & 0 & 0 & 0 & \dfrac{G_{xz,j}}{f}
\end{bmatrix} \tag{2}$$

where $\nu_{xy,j}$ and $\nu_{yx,j}$ are the Poisson's ratios, $E_{x,j}$ and $E_{y,j}$ are the elastic moduli and $G_{xy,j}$, $G_{yz,j}$ and $G_{xz,j}$ are the in-plane and transverse shear moduli, respectively. In a finite element analysis where the transverse shear strain is assumed to be constant through the thickness of each layer, it is common to reduce the transverse shear moduli by a "shear correction factor" of 1.2 to compensate for the excessive amount of shear strain energy produced [5]. In the current finite element formulation the transverse shear moduli of each layer are reduced by a factor f given by

$f = 1.2$ or $f = 1.0 + 0.2\dfrac{A}{25h^2}$ whichever is greater, where A is the area of the element and h the thickness of the panel. The latter expression is included in order to prevent shear locking [5]. The homogeneous properties of the corrugated core layers are obtained according to ref. [8].

The stiffness matrix can be integrated through the thickness h of the panel to obtain the extensional, coupling and bending stiffness matrices as follows

$$[A] = \sum_{j=1}^{N} [Q]_j \left(z_j - z_{j-1} \right) \tag{3a}$$

$$[C] = \frac{1}{2} \sum_{j=1}^{N} [Q]_j \left(z_j^2 - z_{j-1}^2 \right) \tag{3b}$$

$$[D] = \frac{1}{3} \sum_{j=1}^{N} [Q]_j \left(z_j^3 - z_{j-1}^3 \right) \tag{3c}$$

where z_j are the ply coordinates [8] and N= 3, 5, 7. These stiffness matrices in turn can be combined with the strain-displacement matrix [B], which connects the displacements to the strains and curvatures of the element, to form the element stiffness matrix [k] as follows

$$[k] = \int_A \left([B_0]^T [A][B_0] + [B_0]^T [C][B_1] + [B_1]^T [C][B_0] + [B_1]^T [D][B_1] \right) dA \qquad (4)$$

where $[B_0]+z[B_1] = [B]$, see e.g. [16]. The element stiffness matrices are subsequently assembled to a global stiffness matrix $[K]$, which is used in an eigenvalue analysis of the finite element model to determine a suitable load step for the non-linear analysis. The following equation is solved in the eigenvalue analysis

$$\left([K] + \chi [S]_{ref} \right) \{ \psi \} = \{ 0 \} \qquad (5)$$

where $[S]_{ref}$ is obtained by applying consistent nodal forces $\{P\}_{ref}$ on the top and bottom edges corresponding to a uniform unit pressure, and performing a static linear analysis to obtain the membrane stresses that generate the "stress stiffness matrix" $[S]_{ref}$ [16]. χ is the factor used to multiply the loads that generate the stresses, and $\{\psi\}$ is the generalised displacement vector for the nodes [16]. The load $\{P\}$ is scaled by the factor χ which also alters the intensity of the membrane stresses but not the distribution of the stresses such that

$$\{P\} = \chi \{P\}_{ref} \iff [S] = \chi [S]_{ref} \qquad (6)$$

As χ is increased, the overall stiffness of the box, $([K] + [S])$, is reduced until a critical load $\{P\}_{cr}$ corresponding to the eigenvalue χ_{cr} is reached and the box becomes unstable, i.e. $\det([K] + [S])$ goes to zero.

The panels collapse at a load much higher than the critical buckling load P_{cr}. In this so-called postbuckled state, the deflection of a panel is large enough to introduce geometric non-linearities between the load and displacement of the panel. This means that the stiffness matrix $[K]$ of the box becomes a function of the unknown displacements, i.e.

$$[K(\psi)]\{\psi\} = \{P\} \qquad (7)$$

where $\{\psi\}$ is a set of known and unknown nodal displacements and $\{P\}$ represents a set of external loads that act on the nodes. In order for the finite element model of the box to exhibit out-of-plane deformation, it must contain an imperfection, which in our case is introduced as an eccentricity of the applied loads [7] simulated by introducing a moment that is proportional to the load at the top and bottom edges using element COMBIN37. The nonlinear problem is solved step-wise using the Newton-Raphson method [15, 16]. The general algorithm proceeds as follows [5].

1. Prescribe known displacements $\{\psi^k\}_i$ of the nodes on the edges parallel to the y-axis, in this case a uniform displacement. The superscript k denotes known displacements and the subscript i is the load step.
2. Compute the unknown forces $\{P\}_i$ and displacements $\{\psi^u\}_i$ using the stiffness matrix from the earlier step $[K]_{i-1}$ (For the first step, $i = 1$, the global stiffness matrix of the un-deformed panel is used $[K]_0$).

$$[K]_{i-1}(\{\psi^k\}_i + \{\psi^u\}_i) = \{P\}_i$$

3. Compute the updated stiffness matrix $[K]_i$ corresponding to the configuration $\{\psi^k\}_i + \{\psi^u\}_i$.

4. Calculate restoring force $\{P^r\}_i$ and the change in displacements $\{\Delta\psi\}_i$ as follows
$$[K]_i(\{\psi^k\}_i + \{\psi^u\}_i + \{\Delta\psi\}_i) = \{P\}_i + \{P^r\}_i.$$

5. Convergence is checked by $\text{Max}\{\Delta\psi\}_i \leq c$ where c is an arbitrary small number for which equilibrium is approximately obtained.

6. If the solution is not converged, add $\{\Delta\psi\}_i$ to $\{\psi^u\}_i$, add $\{P^r\}_i$ to $\{P\}_i$ and repeat steps 3 - 5.

7. If the solution is converged continue with the next load step
$$\{\psi^k\}_{i+1} = \{\psi^k\}_i + \{\psi^u\}_i + \{\Delta\psi\}_i + \{\Delta\psi^k\}_{i+1}.$$

The loading is terminated when the stress-state at any point in the facings of the panels exceeds a predefined failure criterion.

Failure criterion

In this study the Tsai-Wu tensor failure theory [13] is used to obtain the ultimate load-carrying capacity of a box. According to this theory, in the plane stress condition, material failure develops when $f=1$, where

$$f = \Gamma_1\sigma_x + \Gamma_2\sigma_y + \Gamma_{11}\sigma_x^2 + \Gamma_{22}\sigma_y^2 + \Gamma_{66}\tau_{xy}^2 + 2\Gamma_{12}\sigma_x\sigma_y \tag{8}$$

where $\Gamma_{11} = -\dfrac{1}{\sigma_{x,t}\sigma_{x,c}}, \Gamma_{22} = -\dfrac{1}{\sigma_{y,t}\sigma_{y,c}}, \Gamma_{12} = -0.36\sqrt{F_{11}F_{22}}, \Gamma_1 = \dfrac{1}{\sigma_{x,t}} + \dfrac{1}{\sigma_{x,c}}$,

$\Gamma_2 = \dfrac{1}{\sigma_{y,t}} + \dfrac{1}{\sigma_{y,c}}, \Gamma_{66} = \dfrac{1}{\sigma_{x,c}\sigma_{y,c}}$

The subscript j=t or j=c of strength $\sigma_{i,j}$, i=x,y, denotes the strength in tension and compression, respectively. The expressions for Γ_{12} and Γ_{66} are approximations for paper materials [13]. It is assumed that the box fails as soon as this failure criterion is fulfilled in any point of the outer facings of the corrugated board.

EVALUATION OF MODEL

Boxes of different sizes and board grades, B-140T/112R/140T, C-140T/112R/140T, C-140K/112R/140K and C-180L/112R/180L were studied. The corrugated board is coded, the first letter indicates the geometry of the core, see Table 2. The three following sets of a number and a letter indicate the liner and fluting composition of the board, see Table 1. Material data for the liners and fluting, measured according to the Scandinavian pulp, paper and board standard SCAN-P 67:93 and SCAN-P 46:83, is shown in Table 1 and geometry of the corrugated cores in Table 2. Observe that the compression strength is assumed to be 0.78*SCT (Short-span Compression Test) due to the small specimen size used in the SCT [17]. The finite element models do not

include any imperfections. Instead, eccentricity moments are introduced at the top and bottom edges.

Evaluation of the element density requirements

When performing a finite element analysis the chosen number of elements is a balance between accuracy and calculation time. A larger number of elements could give a more precise solution, but the calculation time increases dramatically with the number of elements. In order to check the influence of element size on the calculated failure load, finite element solutions were generated for boxes with a size of 300x300x300 mm (LengthxWidthxHeight). Eccentricity moments bending the panels outward, obtained in Ref. [7] as the residual after folding the flaps, are introduced at the top and bottom edges with 0.6 Nmm/mm for B-140T/112R/140T and C-180L/112R/180L. Stiffness of the creases is 20.0 (N/mm)/mm for both boards. As can be seen in Table 3, the number of elements has little influence on the box strength estimates. The largest difference is for the 16 element B-140T/112R/140T box, suggesting that the element size is more important for light and thin board grades than for heavy and thick board grades. Figure 4 shows the effect of element size on the Tsai-Wu failure criterion f, eq.(16), where 16 elements give too low precision. So generally, 16 elements seem to be too few but 64 elements and upwards give good accuracy for both B- and C-flute.

Table 1. Material data for liners and flutings (Compression strength is 0.78*SCT and stiffness in compression is set equal to stiffness in tension)

140 T Testliner 3	Avg	Sd	n
Grammage (g/m^2)	136	0.9	30
Thickness (µm)	225	8.1	30
Tensile stiff MD (kN/m)	830	18	10
Tensile stiff CD (kN/m)	460	10	10
Tensile str MD (kN/m)	6.4	0.71	10
Tensile str CD (kN/m)	3.8	0.43	10
SCT MD (kN/m)	3.3	0.22	10
SCT CD (kN/m)	2.4	0.18	10

180 L Testliner 2	Avg	Sd	n
Grammage (g/m^2)	178	1.3	30
Thickness (µm)	283	9.5	30
Tensile stiff MD (kN/m)	1190	18	10
Tensile stiff CD (kN/m)	550	15	10
Tensile str MD (kN/m)	9.97	0.98	10
Tensile str CD (kN/m)	4.63	0.54	10
SCT MD (kN/m)	4.98	0.21	10
SCT CD (kN/m)	3.29	0.16	10

140 K Kraftliner	Avg	Sd	n
Grammage (g/m^2)	139	1.2	30
Thickness (µm)	195	5.8	30
Tensile stiff MD (kN/m)	1390	23	10
Tensile stiff CD (kN/m)	490	21	10
Tensile str MD (kN/m)	14.0	0.31	10
Tensile str CD (kN/m)	5.3	0.24	10
SCT MD (kN/m)	5.1	0.12	10
SCT CD (kN/m)	2.7	0.08	10

112 R Recycled fluting	Avg	Sd	n
Grammage (g/m^2)	114	0.87	30
Thickness (µm)	199	8.2	30
Tensile stiff MD (kN/m)	911	19	10
Tensile stiff CD (kN/m)	354	13	10
Tensile str MD (kN/m)	7.32	0.26	10
Tensile str CD (kN/m)	2.9	0.16	10
SCT MD (kN/m)	3.8	0.16	10
SCT CD (kN/m)	2.12	0.12	10

Table 2. Flute profiles. α is the ratio of flute to liner length.

Profile	B	C
Wavelength, λ (mm)	6.3	7.8
Flute height, h_c (mm)	2.46	3.61
Take-up factor, α	1.32	1.43

Table 3. Failure load (N) of the whole box versus number of elements.

300x300x300 mm, C-180L/112R/180L		
No. of elements	FEM (N)	Index
16	4768	1.04
36	4631	1.01
64	4630	1.01
144	4605	1.00
256	4590	1.00
300x300x300 mm, B-140T/112R/140T		
No. of elements	FEM (N)	Index
16	2516	1.15
36	2275	1.04
64	2188	1.00
144	2181	1.00
256	2165	0.99
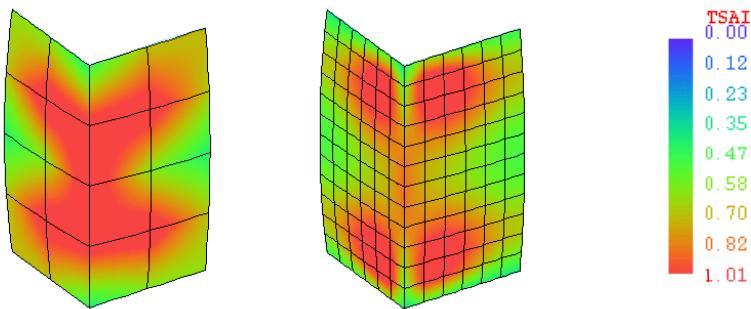
Figure 4.   Tsai-Wu value f of the inner facings, eq.(16), for the 300x300x300 mm box, B-140T/112R/140T with 16 and 144 elements respectively.

Evaluation of Tsai-Wu failure criterion vs. compression load

The collapse load of boxes size 300x300x100 mm and 300x300x300 mm is predicted using the Tsai-Wu failure criterion, eq. (8). Eccentricity moments bending the panels outward are introduced at the top and bottom edges with 0.6 Nmm/mm for C-

140T/112R/140T. Crease stiffness is 20 (N/mm)/mm. In order to make the analyses converge within reasonable time, a Tsai-Wu value between $f = 0.95$ and $f = 1.05$ is used. Typically, the maximum difference in strength predictions between $f = 0.95$ and $f = 1.05$ is within 4%. However, when small differences between subsequent predictions need to be studied a more accurate prediction is necessary. Figures 5 and 6 show typical load vs. Tsai-Wu curves and the load vs. out-of-plane displacements. Since there is almost a linear relationship between the Tsai-Wu value and the load in Figures 5 and 6, the result from the FEM-calculation, P_i, can be adjusted using the present and previous Tsai-Wu value, f_i and f_{i-1} and load step ΔP to obtain the failure load.

$$P_f = \frac{\Delta P}{f_i - f_{i-1}}\left(1 - f_i\right) + P_i \tag{9}$$

The box strength estimated using eq. (9) is $P_f = 3052$ N for C-140T/112R/140T, 300x300x300mm and $P_f = 4873$ N for C-140T/112R/140T, 300x300x100mm. For the boxes in chapter 4 (Appendix Table A1 and A2) the maximum correction with eq. (9) is 2.9% and the average correction is 1.2%.
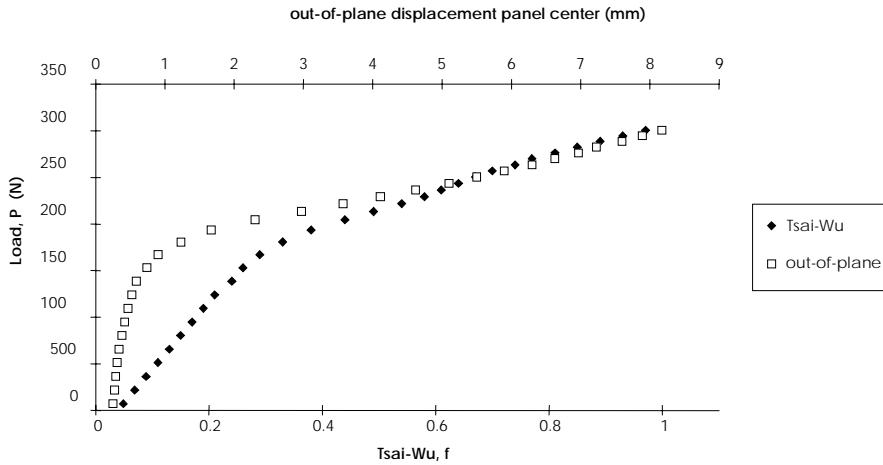
Figure 5. Load vs. Tsai-Wu value f and out-of-plane displacement for C-140T/112R/140T, 300x300x300mm. $P_f = 3052$ N. Since eccentricity moments bending the panels outward are introduced at the top and bottom edges, the Tsai-Wu value and out-of-plane displacement are not zero at zero load.
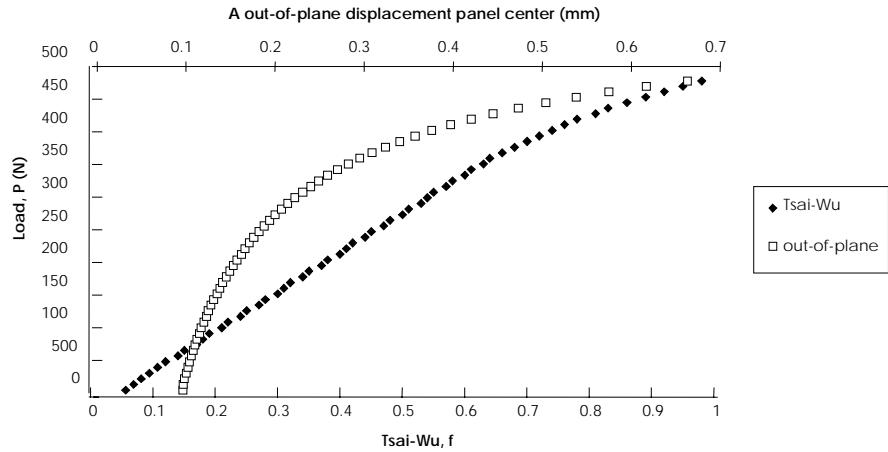
Figure 6. Load vs. Tsai-Wu value *f* and out-of-plane displacement for C-140T/112R/140T, 300x300x100mm. $P_f = 4930$ N.

Additional failure criterion

If boxes do not buckle, failure load is limited by the crushing strength of the corrugated board, see Figure 7. The crushing strength of the creased corrugated board is about 50% of the edge crush test strength (ECT) [7], and the ECT can be predicted from the short-span compression test (SCT) of the board constituents [17]. Thus the crushing strength per unit length of the creased corrugated board, *CBS*, in the CD, see Figure 7, is

$$\text{CBS} = \frac{0.85}{2}\left(0.78\text{SCT}_1 + \sum_{k=1}^{M} 0.78\left(\alpha_{2k}\text{SCT}_{2k} + \text{SCT}_{2k+1}\right)\right) \tag{10}$$

where α_{2k} is the take-up factor of the corrugated core layer 2k and when M = 1, 2, 3 it corresponds to single, double or triple-wall board, see Figure 1. For board C-140T/112R/140T CBS = 2.59 N/mm. In chapter 3.2 the crushing strength of box no.1 C-140T/112R/140T, 300x300x100mm, see Appendix Table A2, is $P_{crush} = 3108$ N and corresponding experimental value is $P_{f,exp} = 2932$ N. $P_{crush} = 3823$ N and $P_{f,exp} = 3290$ N for box no.13 C-180L/112R/180L, 300x300x100mm, see Appendix Table A2.
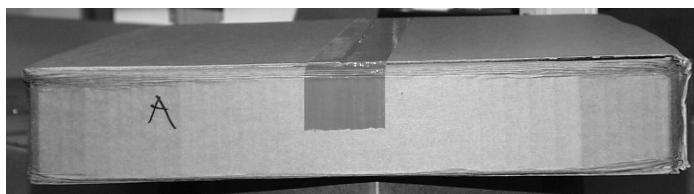
Figure 7. A crushed shallow box.

Influence of the edge stiffness

The edge/crease stiffness is an important property for box compression strength because it affects the load distribution on the top and bottom edges when the side panels buckle. Thus, a soft edge prevents a redistribution of the load towards the corners of a box during buckling. This increases the bending of the panels and reduces box strength. Edge/crease stiffness can be measured by using a special rig [7]. Figures 8a and 8b show the predicted failure load as a function of the edge stiffness for a box with B- and C-board, respectively. The predicted failure load increases rapidly with stiffness until stiffness gets close to the stiffness of a cut-edge. For the B-flute box the strength increases by about 16% between stiffness 2 and 100, whereas for C-flute the increase is about 8%.
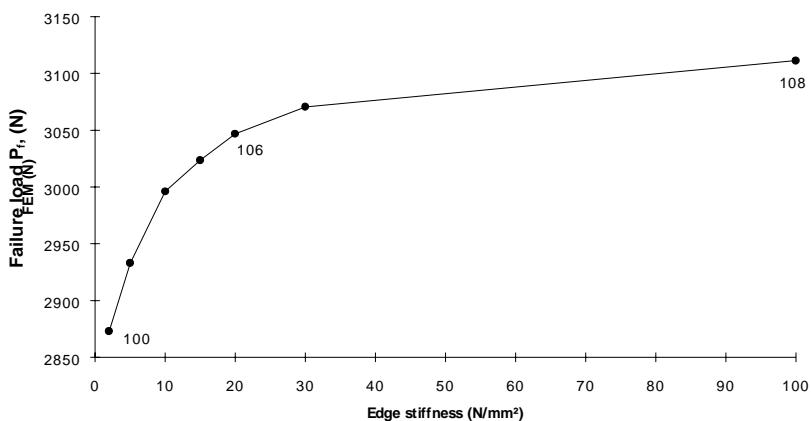
Figure 8a.   Predicted failure load for B-140T/112R/140T, 300x300x300 mm. An index is included for stiffness 2.0, 20.0 and 100 (N/mm)/mm.
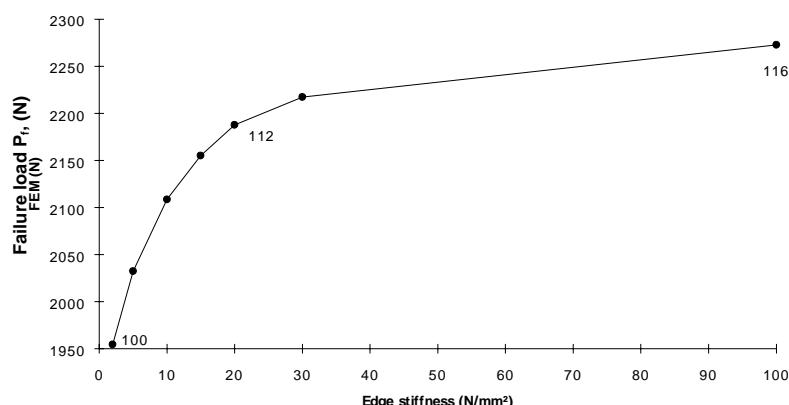
Figure 8b.   Predicted failure load for C-140T/112R/140T, 300x300x300 mm. An failure index is included for stiffness 2, 20 and 100 (N/mm)/mm.

Influence of eccentricity moments orientation on buckling modes

Applying different eccentricity moments at the loaded edges triggers different buckling modes. Two alternative moment directions are used corresponding to a panel buckling direction inwards or outwards, see Figure 9. Results in Table 4 show that outward moment for all panels clearly gives the strongest box and inward moment gives the weakest box. Since the panels are completely identical and the value of the moment is 0.6 Nmm/mm in all cases, the difference in strength is only caused by geometrical differences in the buckling patterns. Displacements of the box corners in particular will be different, see Figure 10.
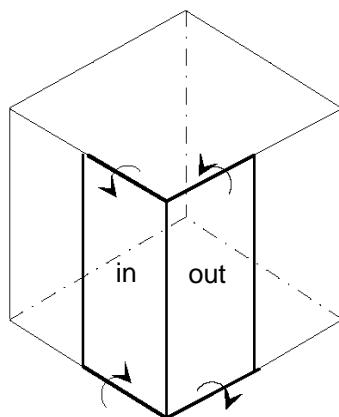
Figure 9. Applied eccentricity moments.

Table 4. Boxes size 300x300x300 mm and symmetrical board C-140K/112R/140K

Driving moment	Failure load, N	Index	Buckling
all out	3942.9	100	all out
all in	3565.8	90	all in
2 out/2 in	3673.5	93	2 out/2 in
3 out/1 in	3671.8	93	3 out/1 in
3 in/1 out	3566.3	90	3 in/1 out

Displacement of the corners (mm)

**Out-of-plane displacement
at panel centre (mm)**
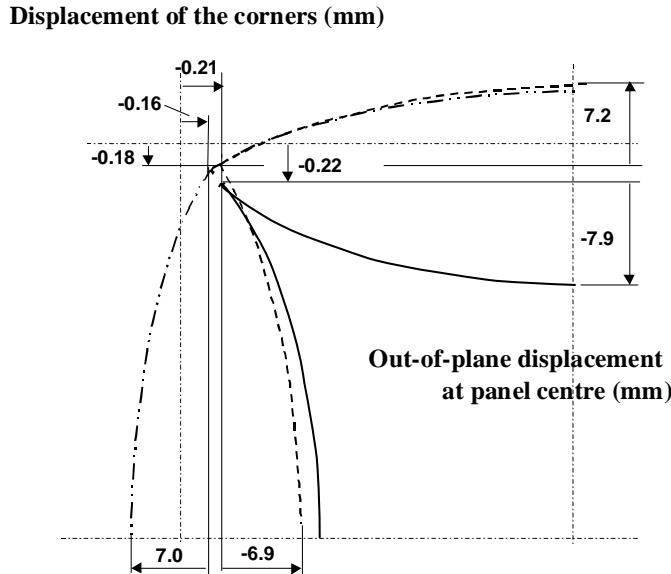
Figure 10. Schematics of deformed corner cross-sections at the centre of the box. The dot-dashed lines indicate original position of the corners. The schematics are not drawn to scale. The three first buckling modes in Table 4 are shown at index load 90.

If the ratio between height and width of the panels is different panels can buckle in completely different ways, see Figure 11.

**1/4 model
300x300x300**

**1/4 model
400x200x300**
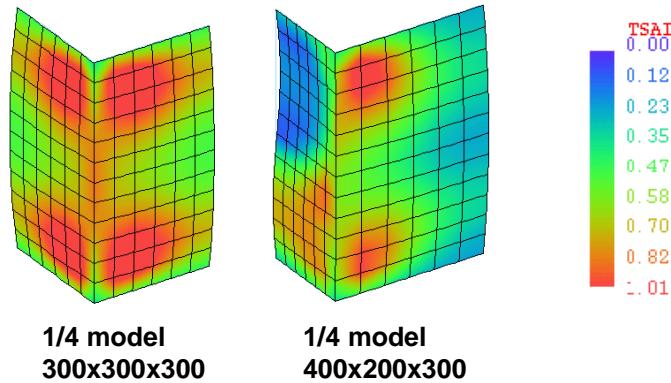
Figure 11. Tsai-Wu value *f* of the inner facings, eq.(16). Different buckling modes of boxes with the same perimeter.

EXPERIMENTS AND VERIFICATION OF FINITE ELEMENT MODEL

Boxes made from board with either a B-flute or a C-flute profile, see Table 2, have been tested to verify the finite element model. About fifty different box geometries for each flute profile and a total of 1,316 boxes were tested. All boxes were unprinted and manually creased, slotted, glued and erected. All boxes were conditioned at 23°C and at 50% RH for at least 24 hours. Some of the tests were performed at SCA Packaging Munksund with a rigid platen box compression tester, and some at SCA Packaging Research, Aylesford, with a floating platen (rotational unrestrained) box compression tester. Compression speed was 10 mm per minute and time to failure was about one minute.

Specifications, box compression test (BCT) results and FEM estimates of the tested boxes are listed in Table A1 and Table A2 in the Appendix together with material data for the liners and mediums in Table A3. All predicted strengths are based on an edge stiffness of 2 N/mm^2 and an element density of 144 elements. Moment applied at the loaded edges is 0.6 Nmm/mm [7] in the conservative configuration in/out, see Table 4.

Figures 12 and 13 show comparisons between box strength estimated with FEM and the strength of tested handmade boxes according to Table A1 and A2, respectively. On average, the finite element simulation predicted strength 3 % above the tested average of boxes in Figure 12 and 5 % below average of boxes in Figure 13. However, two of the tested boxes in Figure 13 (box no.1 and 13) have a strength that is significantly less than predicted. These boxes are shallow, which makes them less inclined to buckle and they fail due to crushing instead, see chapter 3.3. No explanation has yet been found for the over-conservative predictions for box geometries Nos. 29, 30 and 49.
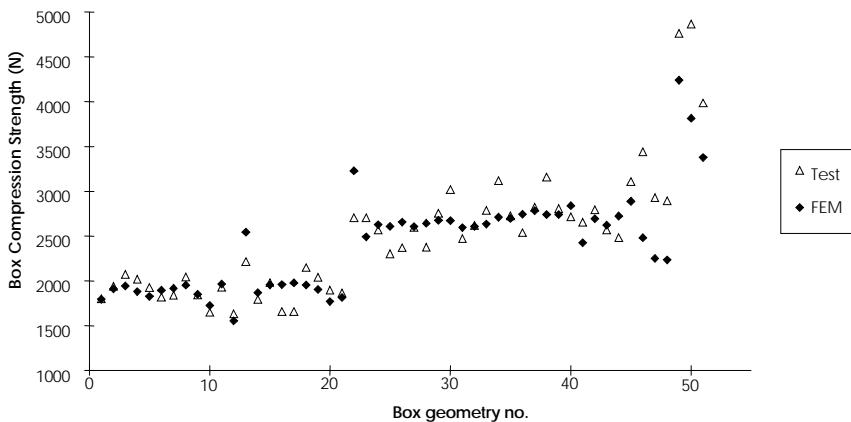
Figure 12. FEM-estimate box strength compared to test results for a range of handmade boxes according to Table A1. Flute profile B, see Table 2.
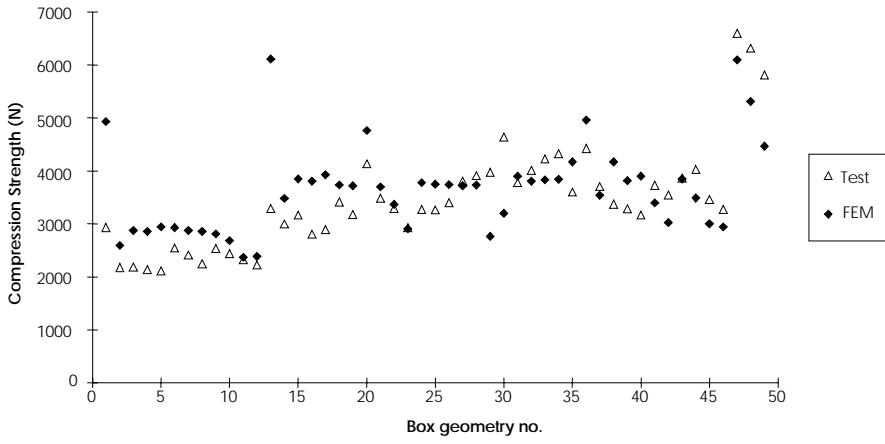
Figure 13. FEM-estimate box strength compared to test results for a range of handmade boxes according to Table A2. Flute profile C, see Table 2.

CONCLUSIONS AND REMARKS

A finite element model of corrugated board containers is shown to predict the failure load of boxes, made from B- and C-board, within an average error margin of 5%. Effective material properties of the homogenised corrugated cores have been used, and each layer of the corrugated board is assumed to be orthotropic linear elastic. It is shown that convergence is obtained with relatively few elements, e.g. 64 elements are quite sufficient for a regular size box, i.e. 300x300x300 mm. The edge stiffness has a significant influence on the predicted failure loads because it affects the load distribution on the top and bottom edges when the side panels buckle. There is also a variation of about 10% in the failure load due to different buckling modes, see Table 3. This is attributed to different constraints imposed on the side panels by the corners of a box. Boxes of different sizes and board grades were tested and compared to predicted strengths. On average, the difference between experimental and predicted values was small. However, for some boxes the difference was significant because the boxes did not buckle but were crushed instead.

The described FE-method for predicting the top-to-bottom compressive strength of corrugated containers has been used as the basic component in the subsequent development of a user-friendly computer-based tool for strength design of containers. The graphical interface of this design tool is shown in Figure 14. The example shows menus that relate to input data definition.
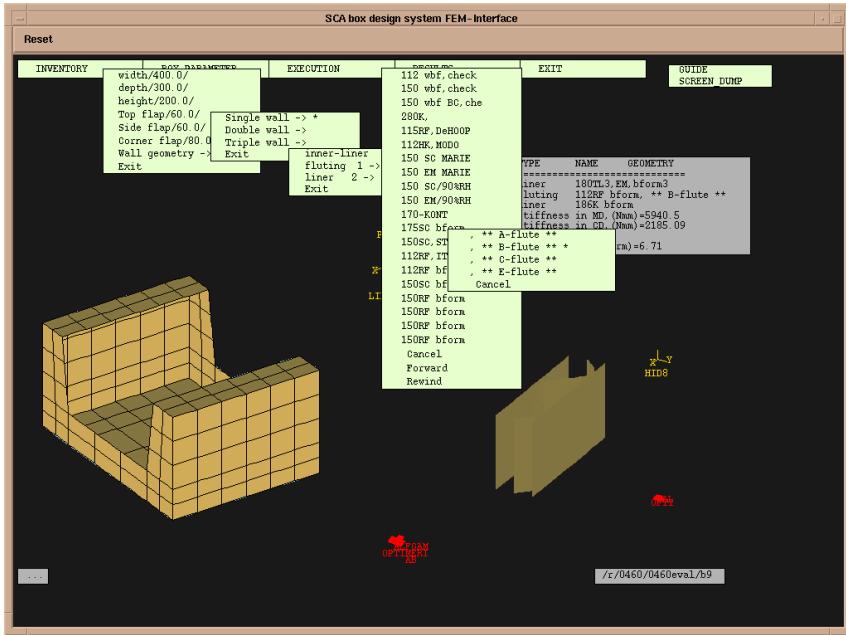
Figure 14. The graphical interface of a design tool for corrugated boxes.

REFERENCES

1. R. Steadman, "Corrugated Board", Ch. 11, in Handbook of Physical Testing of Paper, (R.E. Mark et al. eds.), pp. 563-660, Marcel Dekker, New York, 2002.

2. B. Steenberg, J. Kubat, S. Martin-Löf and L. Rudström, "Competition in Rigid Packaging materials", Svensk Papperstidning., Vol. 73, No. 4, pp. 77-92, 1970.

3. T. Nordstrand, "Parametrical Study of the Post-buckling Strength of Structural Core Sandwich Panels", Composite Structures, No. 30, pp. 441-451, 1995.

4. R. C. McKee and J. W. Gander, "Top-Load Compression", TAPPI, Vol. 40, No. 1, pp. 57-64, 1957.

5. ANSYS User's Manual, Swanson Analysis Systems Inc., Vol.1-2, 1989.

6. O. C. Zienkiewicz, " The Finite Element Method in Engineering Science", McGraw-Hill, 1971.

7. M. Renman, "A mechanical characterization of creased zones of corrugated board", Licentiate thesis, Department of Engineering Logistics, Lund University, Sweden, 1994.

8. L. A. Carlsson, T. Nordstrand and B. Westerlind, "On the Elastic Stiffnesses of Corrugated Core Sandwich", Journal of Sandwich Structures and Materials, Vol. 3, pp. 253-267, Oct., 2001.

9. C. Libove and R. E. Hubka, "Elastic Constants for Corrugated Core Sandwich Plates", NACA TN 2289, 1951.

10. R. Paetow and L. Göttsching , " Poisson's Ratio of Paper", Das Papier a. (in German), Vol. 6, pp. 229-237, 1990.

11. T. Nordstrand and L.A. Carlsson, "Evaluation of Transverse Shear Stiffness of Structural Core Sandwich Plates", Composite Structures, Vol. 37, pp. 145-153, 1997.

12. T. Nordstrand, "Analysis and Testing of Corrugated Board Panels into the Post-buckling Regime", To be submitted to Composite Structures.

13. C. Fellers, B.S. Westerlind and A. de Ruvo, "An Investigation of the Biaxial Failure of Paper: Experimental Study and Theoretical Analysis", Transaction of the Symposium held at Cambridge: September 1981, Vol. 1, pp 527-559, 1983.

14. P. Patel, T. Nordstrand and L.A. Carlsson, "A Study on the Influence of Local Buckling on the Strength of Structural Core Sandwich Structures", Multiaxial Fatigue and Deformation Testing Techniques, ASTM STP, Vol. 1280, ed. S. Kalluri and P. J. Bonacuse, pp. 264-289, 1997.

15. A. N. Palazotto and S. T. Dennis, "Nonlinear Analysis of Shell Structures", AIAA Education Series, pp. 116 - 154, 1992.

16. R. D. Cock, D. S. Malkus and M. E. Plesha, "Concepts and Applications of Finite Element Analysis", John Wiley & Sons, 1989.

17. B. S. Westerlind and L. A. Carlsson, "Compressive Response of Corrugated Board", TAPPI, 75 (7), pp. 145-154, 1992.

Table A1. Specifications, test results and FEM-estimates for handmade B-flute boxes,
COV was about 5 % for all tested boxes.

Box no.	Length	Width	Height	Flute	Board grade	no. of samples	Mean BCT	FEM	BCT/FEM
	(mm)	(mm)	(mm)				(N)	(N)	
1	200	150	300	B	125MK/150RF/125T	6	1801	1794	1.004
2	300	225	300	B	125MK/150RF/125T	6	1939	1908	1.015
3	350	350	300	B	125MK/150RF/125T	6	2072	1942	1.066
4	400	300	300	B	125MK/150RF/125T	6	2020	1881	1.074
5	400	300	200	B	125MK/150RF/125T	6	1924	1824	1.054
6	400	300	400	B	125MK/150RF/125T	6	1820	1892	0.962
7	400	300	600	B	125MK/150RF/125T	6	1839	1915	0.960
8	400	300	800	B	125MK/150RF/125T	6	2042	1950.	1.047
9	450	250	300	B	125MK/150RF/125T	6	1842	1850.	0.996
10	500	200	300	B	125MK/150RF/125T	6	1646	1723	0.955
11	535	400	300	B	125MK/150RF/125T	6	1931	1964	0.983
12	550	150	300	B	125MK/150RF/125T	6	1631	1554	1.049
13	300	300	100	B	140T/112RF/140T	10	2216	2543	0.871
14	300	300	200	B	140T/112RF/140T	10	1794	1866	0.962
15	300	300	300	B	140T/112RF/140T	10	1981	1954	1.013
16	300	300	450	B	140T/112RF/140T	10	1657	1959	0.846
17	300	300	600	B	140T/112RF/140T	10	1657	1975	0.839
18	400	400	400	B	140T/112RF/140T	10	2148	1953	1.099
19	500	300	400	B	140T/112RF/140T	10	2040	1903	1.072
20	600	200	400	B	140T/112RF/140T	10	1893	1771	1.069
21	600	200	300	B	140T/112RF/140T	10	1863	1815	1.026
22	300	300	100	B	180L/112RF/180L	20	2703	3229	0.837
23	300	300	200	B	180L/112RF/180L	20	2702	2493	1.084
24	300	300	300	B	180L/112RF/180L	20	2567	2629	0.976
25	300	300	450	B	180L/112RF/180L	20	2301	2608	0.882
26	300	300	600	B	180L/112RF/180L	19	2370	2656	0.892
27	400	400	400	B	180L/112RF/180L	20	2597	2606	0.997
28	400	400	600	B	180L/112RF/180L	17	2377	2642	0.899
29	400	400	133	B	180L/112RF/180L	20	2754	2675	1.029
30	375	250	400	B	186K/112RF/200T	10	3020	2670	1.131
31	420	280	400	B	186K/112RF/200T	10	2471	2595	0.952
32	450	300	400	B	186K/112RF/200T	10	2618	2608	1.003
33	480	320	400	B	186K/112RF/200T	10	2785	2635	1.057
34	510	340	400	B	186K/112RF/200T	10	3118	2710	1.151
35	540	360	200	B	186K/112RF/200T	9	2726	2697	1.011
36	540	360	400	B	186K/112RF/200T	10	2540	2743	0.926
37	540	360	600	B	186K/112RF/200T	10	2824	2782	1.015
38	570	380	400	B	186K/112RF/200T	10	3158	2740	1.152
39	590	390	400	B	186K/112RF/200T	10	2805	2740	1.024
40	300	300	100	B	186K/150RF/180T	10	2716	2839	0.956
41	300	300	200	B	186K/150RF/180T	10	2657	2425	1.096
42	300	300	300	B	186K/150RF/180T	10	2795	2694	1.037
43	300	300	450	B	186K/150RF/180T	10	2569	2625	0.979
44	300	300	600	B	186K/150RF/180T	10	2481	2722	0.911
45	400	400	400	B	186K/150RF/180T	10	3109	2887	1.077
46	500	300	400	B	186K/150RF/180T	10	3442	2479	1.388
47	600	200	400	B	186K/150RF/180T	10	2932	2251	1.302
48	600	200	300	B	186K/150RF/180T	10	2893	2234	1.295
49	400	400	400	B	280K/150RF/280K	19	4762	4240	1.123
50	500	300	400	B	280K/150RF/280K	20	4866	3814	1.276
51	600	200	400	B	280K/150RF/280K	20	3987	3378	1.180
					Total	566		Mean	1.0314
								CV %	11.4

Table A2. Specifications, test results and FEM-estimates for handmade C-flute boxes,
COV was about 5 % for all tested boxes.

Box no.	Length (mm)	Width (mm)	Height (mm)	Flute	Board grade	no. of samples	Mean BCT (N)	FEM (N)	BCT/FEM
1	300	300	100	C	140T/112RF/140T	10	2932	4931	0.595
2	300	300	200	C	140T/112RF/140T	10	2177	2597	0.838
3	300	300	300	C	140T/112RF/140T	10	2187	2873	0.761
4	300	300	450	C	140T/112RF/140T	10	2138	2857	0.748
5	300	300	600	C	140T/112RF/140T	10	2118	2947	0.719
6	300	300	150	C	140T/112RF/140T	30	2546	2932	0.868
7	300	300	300	C	140T/112RF/140T	30	2411	2873	0.839
8	300	300	450	C	140T/112RF/140T	30	2246	2857	0.786
9	400	400	400	C	140T/112RF/140T	10	2540	2812	0.903
10	500	300	400	C	140T/112RF/140T	10	2442	2685	0.909
11	600	200	400	C	140T/112RF/140T	10	2324	2368	0.981
12	600	200	300	C	140T/112RF/140T	10	2226	2385	0.933
13	300	300	100	C	180L/112RF/180L	20	3290	6113	0.538
14	300	300	200	C	180L/112RF/180L	19	2996	3481	0.861
15	300	300	300	C	180L/112RF/180L	20	3168	3844	0.824
16	300	300	450	C	180L/112RF/180L	20	2806	3807	0.737
17	300	300	600	C	180L/112RF/180L	20	2889	3928	0.735
18	400	400	400	C	180L/112RF/180L	20	3417	3738	0.914
19	400	400	600	C	180L/112RF/180L	19	3178	3720	0.854
20	400	400	133	C	180L/112RF/180L	20	4134	4762	0.868
21	400	400	400	C	186K/112RF/180T	19	3488	3701	0.942
22	500	300	400	C	186K/112RF/180T	20	3289	3369	0.976
23	600	200	400	C	186K/112RF/180T	19	2929	2906	1.008
24	375	250	400	C	186K/112RF/200T	10	3275	3775	0.867
25	395	260	400	C	186K/112RF/200T	10	3265	3750	0.871
26	420	280	400	C	186K/112RF/200T	10	3403	3746	0.908
27	450	300	400	C	186K/112RF/200T	9	3805	3720	1.023
28	480	320	400	C	186K/112RF/200T	10	3913	3735	1.048
29	510	340	400	C	186K/112RF/200T	10	3971	2764	1.437
30	540	360	200	C	186K/112RF/200T	10	4638	3197	1.451
31	540	360	600	C	186K/112RF/200T	10	3775	3904	0.967
32	540	360	400	C	186K/112RF/200T	20	4011	3807	1.053
33	570	380	400	C	186K/112RF/200T	10	4226	3835	1.102
34	590	390	400	C	186K/112RF/200T	10	4324	3841	1.126
35	300	300	300	C	186K/150RF/180T	29	3606	4170	0.865
36	300	300	100	C	186K/150RF/180T	10	4423	4959	0.892
37	300	300	200	C	186K/150RF/180T	10	3707	3542	1.046
38	300	300	300	C	186K/150RF/180T	10	3373	4170	0.809
39	300	300	450	C	186K/150RF/180T	10	3285	3818	0.860
40	300	300	600	C	186K/150RF/180T	10	3167	3904	0.811
41	360	240	300	C	186K/150RF/180T	30	3730	3393	1.099
42	400	200	300	C	186K/150RF/180T	29	3545	3026	1.172
43	400	400	400	C	186K/150RF/180T	10	3864	3846	1.005
44	500	300	400	C	186K/150RF/180T	10	4030	3491	1.155
45	600	200	400	C	186K/150RF/180T	10	3462	3002	1.153
46	600	200	300	C	186K/150RF/180T	10	3275	2945	1.112
47	400	400	400	C	280K/150RF/280K	19	6596	6097	1.082
48	500	300	400	C	280K/150RF/280K	20	6315	5306	1.190
49	600	200	400	C	280K/150RF/280K	18	5811	4465	1.301
					Total	750		Mean	0.950
								CV %	19.6

Table A3. Material data for liners and flutings.

125 Testliner

Grammage (g/m^2)	121
Thickness (μm)	200
Tensile stiffness MD (MN/m)	0.968
Tensile stiffness CD (MN/m)	0.363
Tensile strength MD (kN/m)	7.744
Tensile strength CD (kN/m)	2.783
SCT MD (kN/m)	3.509
SCT CD (kN/m)	1.815

186 Kraftliner

Grammage (g/m^2)	182
Thickness (μm)	223
Tensile stiffness MD (MN/m)	1.681
Tensile stiffness CD (MN/m)	0.614
Tensile strength MD (kN/m)	16.59
Tensile strength CD (kN/m)	7.05
SCT MD (kN/m)	6.07
SCT CD (kN/m)	3.51

125 Kraftliner

Grammage (g/m^2)	125
Thickness (μm)	164
Tensile stiffness MD (MN/m)	1.374
Tensile stiffness CD (MN/m)	0.503
Tensile strength MD (kN/m)	12.8
Tensile strength CD (kN/m)	4.15
SCT MD (kN/m)	4.74
SCT CD (kN/m)	2.53

200 Testliner

Grammage (g/m^2)	200
Thickness (μm)	315
Tensile stiffness MD (MN/m)	1.537
Tensile stiffness CD (MN/m)	0.501
Tensile strength MD (kN/m)	12.34
Tensile strength CD (kN/m)	4.24
SCT MD (kN/m)	5.68
SCT CD (kN/m)	3.16

140 Testliner

Grammage (g/m^2)	136
Thickness (μm)	225
Tensile stiffness MD (MN/m)	0.83
Tensile stiffness CD (MN/m)	0.46
Tensile strength MD (kN/m)	6.4
Tensile strength CD (kN/m)	3.8
SCT MD (kN/m)	3.33
SCT CD (kN/m)	2.38

280 Kraftliner

Grammage (g/m^2)	280
Thickness (μm)	338
Tensile stiffness MD (MN/m)	2.376
Tensile stiffness CD (MN/m)	0.875
Tensile strength MD (kN/m)	23.8
Tensile strength CD (kN/m)	9.76
SCT MD (kN/m)	8.65
SCT CD (kN/m)	5.06

140 Kraftliner

Grammage (g/m^2)	139
Thickness (μm)	195
Tensile stiffness MD (MN/m)	1.39
Tensile stiffness CD (MN/m)	0.49
Tensile strength MD (kN/m)	14.0
Tensile strength CD (kN/m)	5.3
SCT MD (kN/m)	5.1
SCT CD (kN/m)	2.7

112 Recycled fibre fluting

Grammage (g/m^2)	114
Thickness (μm)	199
Tensile stiffness MD (MN/m)	0.911
Tensile stiffness CD (MN/m)	0.354
Tensile strength MD (kN/m)	7.32
Tensile strength CD (kN/m)	2.9
SCT MD (kN/m)	3.8
SCT CD (kN/m)	2.12

180 Testliner (L)

Grammage (g/m^2)	178
Thickness (μm)	283
Tensile stiffness MD (MN/m)	1.19
Tensile stiffness CD (MN/m)	0.55
Tensile strength MD (kN/m)	9.97
Tensile strength CD (kN/m)	4.63
SCT MD (kN/m)	4.98
SCT CD (kN/m)	3.29

150 Recycled fibre fluting

Grammage (g/m^2)	151
Thickness (μm)	231
Tensile stiffness MD (MN/m)	1.142
Tensile stiffness CD (MN/m)	0.449
Tensile strength MD (kN/m)	8.95
Tensile strength CD (kN/m)	3.45
SCT MD (kN/m)	4.82
SCT CD (kN/m)	2.76